NASA TECHNICAL NOTE

NASA TN D-8322

c.1

NASA TN D-8322

POST SUNSET BEHAVIOR OF THE 6300 Å ATOMIC OXYGEN AIRGLOW EMISSION

Robert E. Smith

George C. Marshall Space Flight Center
Marshall Space Flight Center, Ala. 35812

NATIONAL AERONAUTICS AND SPACE ADMINISTRATION • WASHINGTON, D. C. • OCTOBER 1976

TECHNICAL

1. REPORT NO. NASA TN D-8322	2. GOVERNMENT ACCESSION NO.	3. RECIPIENT'S CATALOG NO.

4. TITLE AND SUBTITLE

Post Sunset Behavior of the 6300 Å Atomic Oxygen Airglow Emission

5. REPORT DATE
October 1976

6. PERFORMING ORGANIZATION CODE

7. AUTHOR(S)
Robert E. Smith

8. PERFORMING ORGANIZATION REPORT #
M-178

9. PERFORMING ORGANIZATION NAME AND ADDRESS

George C. Marshall Space Flight Center
Marshall Space Flight Center, Alabama 35812

10. WORK UNIT NO.

11. CONTRACT OR GRANT NO.

13. TYPE OF REPORT & PERIOD COVERED

Technical Note

12. SPONSORING AGENCY NAME AND ADDRESS

National Aeronautics and Space Administration
Washington, D. C. 20546

14. SPONSORING AGENCY CODE

15. SUPPLEMENTARY NOTES

Prepared by Space Sciences Laboratory, Science and Engineering Directorate

16. ABSTRACT

A theoretical model of the 6300 Å OI airglow emission has been developed based on the assumptions that both the charged and neutral portions of the Earth's upper atmosphere are in steady state conditions of diffusive equilibrium. Intensities of the 6300 Å OI emission line have been calculated using electron density-true height profiles from a standard C-4 ionosonde and exospheric temperatures derived from Fabry-Perot interferometer measurements of the Doppler-broadened 6300 Å emission line shape as inputs to the model. Reaction rate coefficient values, production mechanism efficiencies, solar radiation fluxes, absorption cross sections, and models of the neutral atmosphere have been varied parametrically to establish a set of acceptable inputs which will consistently predict 6300 Å emission intensities that closely agree with intensities observed during the post-sunset twilight period by an airglow observatory consisting of a Fabry-Perot interferometer and a turret photometer.

Emission intensities that can only result from the dissociative recombination of molecular oxygen ions were observed during the latter portion of the observational period. They were used with limiting values, taken from the literature, of the quenching coefficients and the production mechanism efficiencies to establish a representative model of the atmosphere. Based on current knowledge of the nearby hydroxyl bands and the configuration of the equipment used to obtain the observational data, theoretical calculations indicate that contamination of the 6300 Å OI emission should be on the order of or less than 3 percent; however, these results are very sensitive to the wavelengths of the individual lines and their intensities relative to the 6300 Å OI intensity.

This combination of a model atmosphere, production mechanism efficiencies, and quenching coefficient values was used during the earlier portion of the period when the dissociative photoexcitation and direct impact excitation processes were contributing to the intensity to establish best estimates of solar radiation fluxes in the Schumann-Runge continuum and associated absorption cross sections.

Results of this analysis show that the Jacchia 1971 model of the upper atmosphere combined with the Ackerman (1970) recommended solar radiation fluxes and associated absorption cross sections produces theoretically calculated intensities that more closely agree with the observed intensities than all the other combinations when the following set of reaction rate coefficients and efficiencies is used:

$O^+ + O_2 \rightarrow O_2^+ + O$	2×10^{-11} cm^3 s^{-1}
$O_2^+ + e \rightarrow O^* + O$	1.95×10^{-7} $(300/T)^{0.7}$ cm^3 s^{-1} with an efficiency of producing an $O(^1D)$ atom of $0.50\binom{+0.32}{-0.12}$
$O^+ + N_2 \rightarrow NO^+ + N$	1×10^{-12} cm^3 s^{-1}
$NO^+ + e \rightarrow N + O$	4.5×10^{-7} $(300/T)$ cm^3 s^{-1} with no $O(^1D)$ atoms being produced
$O(^1D) + O_2 \rightarrow O(3P) + O_2^*$	5×10^{-11} cm^3 s^{-1}
$O(^1D) + N_2 \rightarrow O(3P) + N_2^*$	$(1^{+0.00}_{-0.11}) \times 10^{-10}$ cm^3 s^{-1}

However, the analysis showed that the third source of $O(^1D)$ atoms, by conjugate point photoelectrons, contributed significantly to the overall observed intensity during the early portion of the post-sunset twilight period with the contribution decreasing with increasing conjugate point solar zenith angle. No $O(^1D)$ atoms were produced by this mechanism after conjugate point sundown, assuming a screening height of 180 km, when the conjugate point solar zenith angle was approximately 103°.

17. KEY WORDS	18. DISTRIBUTION STATEMENT Category 46

19. SECURITY CLASSIF. (of this report) Unclassified	20. SECURITY CLASSIF. (of this page) Unclassified	21. NO. OF PAGES 161	22. PRICE $6.25

For sale by the National Technical Information Service, Springfield, Virginia 22161

ACKNOWLEDGMENTS

I wish to thank Dr. Ernest G. Fontheim, Dr. Raymond G. Roble, and Professor Frederick L. Bartman for their guidance and assistance. I appreciate the stimulative discussions with and assistance of Drs. Paul B. Hays and Andrew F. Nagy.

I am also grateful to Dr. Gary R. Swenson for his assistance in setting up and operating the airglow observatory and for the many stimulating discussions and helpful suggestions, and to Mrs. Jeanette A. Scissum for her assistance in programming the model.

I also appreciate the many discussions with Dr. Eric C. Butcher, Dr. Shi T. Wu, Dr. Ru J. Hung, Dr. Ganti L. Rao, Mr. James O. Ballance, and Mr. Richard H. Comfort and their suggestions and assistance in completing this study.

TABLE OF CONTENTS

		Page
I.	INTRODUCTION	1
II.	THEORY OF THE 6300 Å TWILIGHT GLOW	3
	A. Source of the Emission	3
	B. Dissociative Photoexcitation	4
	C. Dissociative Recombination	6
	D. Photoelectron Impact Excitation	11
	E. Quenching	20
III.	INSTRUMENTATION AND OBSERVATIONS	20
	A. Instrumentation	20
	B. Observational Measurements	30
IV.	NEUTRAL ATMOSPHERE	46
	A. Models	46
	B. Columnar Number Densities	46
	C. Exospheric Temperatures	49
V.	THEORETICAL APPROACH	49
	A. Photodissociation	49
	B. Dissociative Recombination	50
	C. Volume Emission Rate	52
	D. Integrated Emission Intensity	52
VI.	SOLAR FLUXES AND ABSORPTION CROSS SECTIONS	52
VII.	DISCUSSION	52
	A. Reaction and Quenching Rate Coefficients	55
	B. Solar Radiation Fluxes and Associated Absorption Cross Section Effects	64
	C. Neutral Gas Temperature Effects	73
	D. Electron Density-True Height Profile Effects	82
	E. General	83
VIII.	CONCLUSIONS	86
	A. Atmospheric Model	86
	B. Photochemical Rate Coefficients	89
	C. Solar Flux and Absorption Cross Sections	90

TABLE OF CONTENTS (Concluded)

Page

D. Conjugate Point Photoelectrons 91
E. Atmospheric Motions 91
F. General 92

IX. RECOMMENDATIONS FOR FUTURE RESEARCH 92

APPENDIX A — HISTORICAL BACKGROUND 95

APPENDIX B — LISTING OF COMPUTER PROGRAM OF THEORETICAL MODEL 99

APPENDIX C — OBSERVATIONAL DATA 109

APPENDIX D — CONTAMINATION OF THE 6300 Å OI EMISSION BY HYDROXYL EMISSIONS 117

REFERENCES 132

BIBLIOGRAPHY 146

LIST OF ILLUSTRATIONS

Figure	Title	Page
1.	Low energy portion of the atomic oxygen energy level diagram	5
2.	Conjugate point solar zenith angle as a function of Central Standard Time on January 6-7, 1972	19
3.	Schematic drawing of the Fabry-Perot interferometer and associated system components	25
4.	Low brightness source intensity distribution	32
5.	6300 Å intensity as a function of solar zenith angle on January 6, 1972	35
6.	Fabry-Perot interferometer observations of the 6300 Å emission line shapes at 1728 and 1732 CST on January 6, 1972	37
7.	Fabry-Perot interferometer observations of the 6300 Å emission line shapes at 1740 and 1742 CST on January 6, 1972	37
8.	Fabry-Perot interferometer observations of the 6300 Å emission line shapes at 1751 and 1756 CST on Jaunary 6, 1972	38
9.	Fabry-Perot interferometer observations of the 6300 Å emission line shapes at 1805 and 1811 CST on January 6, 1972	38
10.	Fabry-Perot interferometer observations of the 6300 Å emission line shapes at 1822 and 1832 CST on January 6, 1972	39
11.	Fabry-Perot interferometer observations of the 6300 Å emission line shapes at 1845 and 1855 CST on January 6, 1972	39
12.	Fabry-Perot interferometer observations of the 6300 Å emission line shapes at 1903 and 1910 CST on January 6, 1972	40

LIST OF ILLUSTRATIONS (Continued)

Figure	Title	Page
13.	Fabry-Perot interferometer observations of the 6300 Å emission line shapes at 1926 and 1940 CST on January 6, 1972	40
14.	6300 Å emission line shapes at 1728 and 1732 CST on January 6, 1972, after correcting for and removal of the variable intensity of the background	41
15.	6300 Å emission line shapes at 1740 and 1742 CST on January 6, 1972, after correcting for and removal of the variable intensity of the background	41
16.	6300 Å emission line shapes at 1751 and 1756 CST on January 6, 1972, after correcting for and removal of the variable intensity of the background	42
17.	6300 Å emission line shapes at 1805 and 1811 CST on January 6, 1972, after correcting for and removal of the variable intensity of the background	42
18.	Thermospheric temperatures derived from the Fabry-Perot interferometer observed 6300 Å emission line shapes as a function of solar zenith angle on January 6, 1972	43
19.	Contours of constant electron number density	45
20.	6300 Å emission line intensities derived from Fabry-Perot interferometer observations and theoretically calculated intensities as a function of time after sunset on January 6, 1972	57
21.	6300 Å emission line intensities derived from Fabry-Perot interferometer observations and theoretically calculated intensities as a function of time after sunset on January 6, 1972	58
22.	6300 Å emission line intensities derived from Fabry-Perot interferometer observations and theoretically calculated intensities as a function of time after sunset on January 6, 1972	59

LIST OF ILLUSTRATIONS (Continued)

Figure	Title	Page
23.	6300 Å emission line intensities derived from Fabry-Perot interferometer observations and theoretically calculated intensities as a function of time after sunset on January 6, 1972	61
24.	6300 Å emission line intensities derived from Fabry-Perot interferometer observations and theoretically calculated intensities as a function of time after sunset on January 6, 1972	62
25.	6300 Å emission line intensities derived from Fabry-Perot interferometer observations and theoretically calculated intensities as a function of time after sunset on January 6, 1972	63
26.	6300 Å emission line intensities derived from Fabry-Perot interferometer observations and theoretically calculated intensities as a function of time after sunset on January 6, 1972	64
27.	6300 Å emission line intensities derived from Fabry-Perot interferometer observations and theoretically calculated intensities as a function of time after sunset on January 6, 1972	65
28.	6300 Å emission line intensities derived from Fabry-Perot interferometer observations and theoretically calculated intensities as a function of time after sunset on January 6, 1972	66
29.	6300 Å emission line intensities derived from Fabry-Perot interferometer observations and theoretically calculated intensities as a function of time after sunset on January 6, 1972	67
30.	Difference between observed and calculated 6300 Å emission line intensities as a function of time after sunset, attributed to direct impact excitation of atomic oxygen by conjugate point photoelectrons	69

LIST OF ILLUSTRATIONS (Continued)

Figure | Title | Page

31. 6300 Å emission line intensities derived from Fabry-Perot interferometer observations and theoretically calculated intensities as a function of time after sunset on January 6, 1972 70

32. 6300 Å emission line intensities derived from Fabry-Perot interferometer observations and theoretically calculated intensities as a function of time after sunset on January 6, 1972 71

33. Difference between observed and calculated 6300 Å emission line intensities as a function of time after sunset, attributed to direct impact excitation of atomic oxygen by conjugate point photoelectrons 72

34. 6300 Å emission line intensities derived from Fabry-Perot interferometer observations and theoretically calculated intensities as a function of time after sunset on January 6, 1972 73

35. 6300 Å emission line intensities derived from Fabry-Perot interferometer observations and theoretically calculated intensities as a function of time after sunset on January 6, 1972 74

36. Difference between observed and calculated 6300 Å emission line intensities as a function of time after sunset, attributed to direct impact excitation of atomic oxygen by conjugate point photoelectrons 75

37. Contours of constant N_2 number density 76

38. Contours of constant volume emission rate 77

39. 6300 Å emission line intensities derived from Fabry-Perot interferometer observations and theoretically calculated intensities as a function of time after sunset on January 6, 1972 78

LIST OF ILLUSTRATIONS (Continued)

Figure	Title	Page
40.	Difference between observed and calculated 6300 Å emission line intensities as a function of time after sunset, attributed to direct impact excitation of atomic oxygen by conjugate point photoelectrons	79
41.	6300 Å emission line intensities derived from Fabry-Perot interferometer observations and theoretically calculated intensities as a function of time after sunset on January 6, 1972	80
42.	Difference between observed and calculated 6300 Å emission line intensities as a function of time after sunset, attributed to direct impact excitation of atomic oxygen by conjugate point photoelectrons	81
43.	Composite of observational and theoretical data as a function of local solar zenith angle on January 6, 1972	84
44.	Observed and calculated 6300 Å intensities versus the electron number density at the F_2 peak	85
45.	Comparison of 6300 Å emission intensities over Huntsville, Ala., and Blue Hill Observatory, Mass., as a function of solar zenith angle	87
46.	Comparison of F_2 peak electron number densities over Huntsville, Ala., and Blue Hill Observatory, Mass.	88
C-1.	Observational data for November 17, 1971	110
C-2.	Observational data for January 7, 1972	111
C-3.	Observational data for February 4, 1972	112
C-4.	Observational data for February 7, 1972	113
C-5.	Composite of sunset exospheric temperature data	114

LIST OF ILLUSTRATIONS (Concluded)

Figure	Title	Page
C-6.	Composite of sunset intensity data	115
C-7.	Composite of sunset F_2 maximum electron density data	116
D-1.	Chemical kinetics of OH principal reactions	120
D-2.	Chemical kinetics of H principal reactions	122
D-3.	Chemical kinetics of O_3 principal reactions	124
D-4.	6300 Å filter transmission function	128
D-5.	Convolution of 18 emission line profiles from January 6, 1972, with expected positions of OH lines	129
D-6.	Comparison of values of Fourier transform coefficients from theoretical line profiles with those from observational data	130

LIST OF TABLES

Table Title Page

1. Values of Rate Coefficient, α_2, for Dissociative Recombination of O_2^+ Production Mechanism 9

2. Values of Rate Coefficient, α_1, for Dissociative Recombination of NO^+ Production Mechanism 10

3. Values of Rate Coefficient, γ_2, for $O_2 + O^+$ Charge Exchange Reaction 12

4. Values of Rate Coefficient, γ_1, for $N_2 + O^+$ Ion-Atom Interchange Reaction 13

5. Other Sources and Sinks and Associated Values of Their Reaction Rate Coefficients 14

6. Values of Rate Coefficient, q_1, for $O(^1D) + N_2$ Quenching Reaction 21

7. Values of Rate Coefficient, q_2, for $O(^1D) + O_2$ Quenching Reaction 22

8. Values of Rate Coefficient, q_3, for $O(^1D) + O$ Quenching Reaction 23

9. Operating Parameters of the Fabry-Perot Interferometer 26

10. Low Brightness Source Intensity Distribution 31

11. Operation Log 33

12. Neutral Constituent Number Densities at 120 km 46

13. Schumann-Runge Continuum Solar Fluxes of Friedman and Tousey with Associated O_2 Absorption Cross Sections from Metzger and Cook 53

14. Schumann-Runge Continuum Solar Fluxes and Associated O_2 Absorption Cross Sections Recommended by Ackerman 54

LIST OF TABLES (Concluded)

Table	Title	Page
D-1.	Chemical Kinetics of OH	119
D-2.	Chemical Kinetics of H	121
D-3.	Chemical Kinetics of O_3	123

POST SUNSET BEHAVIOR OF THE 6300 Å ATOMIC OXYGEN AIRGLOW EMISSION

I. INTRODUCTION

Knowledge of the physical, chemical, and dynamical processes of the Earth's upper atmosphere has progressed at a rapid pace during this century. The advent of the rocket provided not only the impetus but also, at the same time, a means for obtaining some of the observational data required to support and verify the theoretical analyses. Knowledge of the "glow" emanating from the Earth's upper atmosphere has shared in this remarkable advancement.

From the earliest studies it was quite apparent that analyses of the twilight glow would provide an opportunity to obtain a wealth of data from ground-based observations, because the Sun itself could be used as a differential analyzer to establish altitude profiles of the various processes responsible for creating the glow. Up to the present, most of the detailed analyses of the 6300 Å emission in the twilight glow have been concentrated on the pre-dawn twilight with little emphasis on the post-sunset phase. This study concentrates on the latter situation.

In this analysis available observational data were combined with appropriate models and theories in a parametric type of analysis for the purpose of establishing a consistent theoretical model that could predict the behavior of the intensity of the 6300 Å emission during the post-sunset twilight period.

Analyses of either the pre-dawn or the post-sunset 6300 Å twilight glows require a well coordinated observational-theoretical approach. Theoretical considerations should include:

1. Chemical reactions, their rate coefficients with their temperature dependence, and their efficiencies.

2. Diffusion and mass transport of the various constituents of the atmosphere.

3. Vertical distributions of both the neutral and charged components of the atmosphere and their temporal and spatial variability.

4. The thermal structure of both the neutral and charged components.

5. Solar terrestrial interrelationships, e.g., sunlight conditions at the conjugate point compared with the sunlight conditions at the observational point and level of solar and geomagnetic activity at the time of the observation.

6. Photochemical reactions, their rate coefficients with their temperature dependence, and their efficiencies.

Observational data required either as inputs to the theoretical models of the 6300 Å emission or for comparison with the calculated results should contain:

1. Number density-height profiles of both the neutral and charged components.

2. Temperature-height profiles of both the neutral and charged components.

3. Total integrated emission intensities of the 6300 Å emission and the nearby background, independently obtained.

4. Mass motions, vertically and horizontally, of the neutral and charged components.

5. Photoelectron fluxes and energy spectra entering the atmosphere at the observation point.

Previous theoretical studies and analyses have indicated that dissociative photoexcitation of molecular oxygen by solar ultraviolet radiation in the Schumann-Runge continuum, dissociative recombination of molecular oxygen and nitric oxide ions with thermal electrons, and photoelectron impact excitation of atomic oxygen may all produce ^1D oxygen atoms that contribute to the 6300 Å emission in the twilight glow. These chemical and photochemical processes are discussed in detail in Section II.

The 6300 Å intensity measurements and the equipment used to obtain the observational data are discussed in Section III.

Constituent number densities at 120 km altitude from Jacchia [1] and Reber [2] are combined with analytical temperature profiles after Bates [3] to define two of the models of the neutral atmosphere used parametrically in the analysis. The third model used is the current Jacchia 1971 model [4]. The models and their influence on the computed results are discussed in Sections IV and VII.

The theoretical model of the 6300 Å emission intensity is discussed in Section V where the O(^{1}D) atoms are assumed to be produced only from dissociative photoexcitation and dissociative recombination. Consequences of this assumption are discussed in Section VIII.

Solar radiation fluxes in the Schumann-Runge continuum and molecular oxygen absorption cross sections from Ackerman [5], Table 14, and solar flux values of Friedman and Tousey, as reported by Hinteregger, Hall, and Schmidtke [6] with cross sections from Metzger and Cook [7], Table 13, are used parametrically in this analysis.

Computational results and comparisons with observational data are discussed in detail in Section VII.

Conclusions are presented in Section VIII with recommendations for future research activities outlined in Section IX.

II. THEORY OF THE 6300 Å TWILIGHT GLOW

A. Source of the Emission

When the lowest energy level excited state of neutral atomic oxygen undergoes a radiative transition to the ground state, a quantum of light is produced whose wavelength is proportional to the difference in energy of the levels between which the transition takes place. There are three possible radiative transitions for the O(^{1}D) state:

$$^1D \xrightarrow{6392Å} {}^3P_0$$

$$^1D \xrightarrow{6364Å} {}^3P_1$$

$$^1D \xrightarrow{6300Å} {}^3P_2$$

with respective Einstein coefficients of 1.1×10^{-6} s^{-1}, 2.2×10^{-3} s^{-1}, and 6.9×10^{-3} s^{-1}, where the Einstein coefficient is a measure of the probability that a radiative transition will take place between the two levels in 1 s. From the foregoing it is apparent that a 6300 Å photon is emitted about three times as frequently as a 6364 Å photon, while the probability of the emission of a 6392 Å photon is almost negligible.

Figure 1 shows the low energy portion of the atomic oxygen energy level diagram with associated Einstein coefficients, A, and lifetimes, 1/A. Because of its relatively long lifetime, the $O(^1D)$ state is said to be metastable and, consequently, it should reach thermal equilibrium with the surrounding neutral constituents before it undergoes a radiative transition. For this reason the Doppler broadening of the integrated 6300 Å emission line should provide reliable information about the temperature of the neutral atmosphere in the layer from which the greater portion of the radiation is emanating.

Previous investigators have shown that three mechanisms are capable of producing atomic oxygen in the ^1D excited state. Dissociative photoexcitation of molecular oxygen by solar radiation, primarily the Schumann-Runge continuum, can produce both the ^1D state and the next higher excited state, ^1S, which in turn can produce a ^1D by a radiative transition in which a 5577 Å photon is emitted. Dissociative recombinations of molecular oxygen and nitric oxide ions with thermal electrons are both postulated to be sources of ^1D's with the former also capable of producing the ^1S state; however, the latter reaction, theoretically at least, is believed to be incapable of producing the ^1D state because it violates selection rule criteria. Impact excitation of oxygen atoms by photoelectrons is also postulated to be a source of the ^1D and ^1S states. These three production mechanisms are discussed in detail in the remainder of this section.

B. Dissociative Photoexcitation

Photodissociation of molecular oxygen by ultraviolet solar photons is the primary source of atomic oxygen in the upper atmosphere. The average lifetime of the ground state atoms so created is on the order of days. The average lifetime of the metastable ^1D oxygen atoms so produced is about 110 s. The Schumann-Runge continuum is the primary energy source for the formation of oxygen atoms about 80 km above the Earth's surface.

When an ultraviolet photon in the principal Schumann-Runge continuum wavelength interval is absorbed by an oxygen molecule, one ground state (^3P) and one metastable (^1D) oxygen atom are produced. The ^1D then undergoes a radiative transition to the ground state with most of the emitted photons having a wavelength of 6300 Å .

TERM	J	ENERGY (eV)	LIFETIME (s)	A (s^{-1})
^1S	0	4.19	0.74	1.36
^1D	2	1.97	110	0.0091
	0	0.028		
^3P	1	0.020		
	2	0		

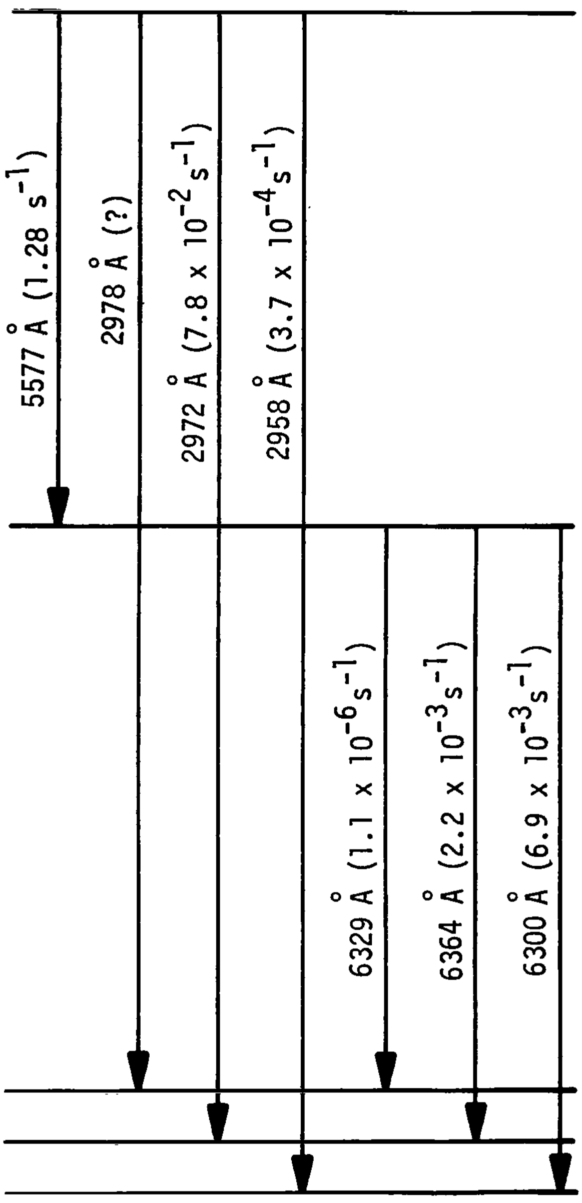

Figure 1. Low energy portion of the atomic oxygen energy level diagram [8].

Brandt [9], on the basis of theoretical calculations, decided that this process would account for 25 to 35 kilorayleighs (kR) in the day glow 6300 Å emission. Noxon [10], from analysis of ground-based photometer measurements, concluded that the great variability of the intensity of the 6300 Å emission appeared to limit the contributions of dissociative photoexcitation to less than a few kilorayleighs in the day glow. He set 3 kR as an upper limit on the steady contribution from this process. His results also implied that the rate coefficient for quenching by O_2 was nearly 1×10^{-10} cm^3 s^{-1}, a result concurred in by Dalgarno and Walker [11].

Wallace and McElroy [12] confirmed previous results which indicated that every O_2 photodissociation by solar flux in the principal Schumann-Runge continuum resulted in a ^1D oxygen atom.

Current observations seem to place an upper limit of approximately 1 kR on the contribution of this process to the day glow.

C. Dissociative Recombination

Bates [13] and Barbier [14] suggested that this process might contribute to the observed post-twilight 6300 Å emission; Chamberlain [15] showed theoretically that it is probably the primary excitation process in the twilight. Brandt [9] proposed that it could account for 15 to 25 kR in the day glow. Chamberlain [16] suggested that this process was a major source of the 6300 Å emission in the night glow. Later, Noxon [10], in his analysis of ground-based photometer measurements in the day and twilight glow, concluded that the great variability in the intensity, even under almost identical ionospheric conditions, was a strong argument against its being the dominant source. By studying the redline intensity variations during the dawn and evening twilights, he showed that the observations were quite different from what would be theoretically predicted using concurrently measured electron density-height profiles. He concluded that the upper limit to contributions from this process would be approximately 3 kR in the day glow.

Despite the consistent picture that is evolving that dissociative recombination is a major process in the twilight glow, there are still some unresolved questions concerning which chemical reactions are involved and which are important, the rates at which these reactions proceed, and their efficiencies in producing ^1D oxygen atoms.

1. CHEMICAL REACTIONS

Original concepts involved only the recombination of electrons with molecular oxygen ions, a reaction that can produce the following combinations of products:

$$O_2^+ + e \rightarrow O(^3P) + O(^3P) \qquad (1)$$

$$O(^3P) + O(^1D) \qquad (2)$$

$$O(^1D) + O(^1D) \qquad (3)$$

$$O(^1D) + O(^1S) \qquad (4)$$

$$O(^3P) + O(^1S) \qquad (5)$$

Later, the recombination of electrons with molecular nitric oxide ions process was included with the reaction proceeding in either of the two following ways:

$$NO^+ + e \rightarrow N(^4S) + O(^1D) \qquad (6)$$

or

$$NO^+ + e \rightarrow N(^2D) + O(^3P) \quad , \qquad (7)$$

followed by

$$N(^2D) + O(^3P) \rightarrow N(^4S) + O(^1D) \quad . \qquad (8)$$

Dalgarno and Walker [11] showed that the formation of ^1D oxygen atoms by reaction (6) violated the conservation of spin selection rule and also that, from an energy standpoint, ^1S oxygen atoms which could then produce ^1D oxygen atoms through a radiative transition could not be formed. However, Biondi and Fiebelman [17] pointed out that there was no direct evidence against the reaction to support the theoretical work of Dalgarno and Walker. Wallace and McElroy [12] supported the work of Dalgarno and Walker [11] by suggesting that quenching of $N(^2D)$ by $O(^3P)$ is unlikely and that the most likely agent is O_2.

Apparently neither reaction (6) or (8) is capable of producing a significant number of ^{1}D oxygen atoms; therefore, reaction (6) has not been included in this study, and only the molecular oxygen dissociative recombination process is considered.

2. CHEMICAL REACTION RATE COEFFICIENTS

Rate coefficient values for the above processes are still unresolved. Tables 1 and 2 contain values for these rate coefficients that were obtained from an extensive literature survey. In this study various combinations of these values were used parametrically to establish a consistent set which would provide the best agreement between theoretical computations and observations of the 6300 Å emission intensity in the twilight glow.

3. PRODUCTION EFFICIENCIES

Estimates of the efficiency of reactions (1) through (5) for producing ^{1}D oxygen atoms range from 0.1 to 1 per each dissociative recombination, being almost equally scattered throughout the range of values quoted. Zipf and Fastie [46] reported that approximately 10 to 15 percent of the reactions resulted in the formation of a ^{1}D. Their report was followed chronologically by Tohmatsu, Ogawa, and Tsuruta [47] with a value of approximately 16 percent; Peterson and Steiger [8] with a value of 10 percent; Brown and Steiger [48] with a value of 10 percent; Donahue, Parkinson, Zipf, Doering, Fastie, and Miller [49] with a value of 20 percent; Gulledge, Packer, Tilford, and Vanderslice [50] with a value of 20 percent; Zipf [51] with a value of 100 percent; Wickwar [36] with a value of 50 percent; and Forbes [52] with values of 12 percent at a temperature of 865 K, 18 percent at a temperature of 1145 K, and 15±7 percent at a temperature of 1000 K. Forbes [52] also concluded that reaction (6) contributed approximately 10 percent of 6300 Å emission in the night glow. In this study efficiencies of both reactions were used parametrically to determine if a "best" value could be established.

4. SOURCE OF MOLECULAR IONS

Molecular oxygen ions are produced by the charge exchange mechanism

$$O^+ + O_2 \rightarrow O + O_2^+ \quad , \tag{9}$$

while nitric oxide ions are produced by the ion-atom interchange mechanism

$$O^+ + N_2 \rightarrow NO^+ + N \quad . \tag{10}$$

TABLE 1. VALUES OF RATE COEFFICIENT, α_2, FOR DISSOCIATIVE RECOMBINATION OF O_2^+ PRODUCTION MECHANISM

$O_2^+ + e \xrightarrow{\alpha_2} O^* + O$ or $O^* + O^*$ or $O + O$	
Biondi and Brown [18]	2 (-7)[a] at 300 K
Sayer [19]	4 (-8) at 2500 K
Nicolet and Aikin [20]	3 (-8)
Kasner, Rogers, and Biondi [21]	3.8+1 (-7) corrected to 1.7 (-7)
Danilov [22]	3 (-10) T^{-1}
Whitten and Poppoff [23]	4 (-7) -4 (-8)
Ivanov-Kholodny [24]	3 (-7) $(300/T)^{1/2}$
Norton, Van Zandt, and Denison [25]	2 (-7) (300/T)
Bortner [26]	2.2 ± 0.5 (-7) $(T/300)^{-0.7}$
Swider [27]	~ 1 (-7)
Zipf [28]	1.5 (-7)
Warke [29]	1.1 (-7) at 300 K
DASA [30]	3 (-7) $T^{-1.2}$
Kasner and Biondi [31,32]	2.2 ± 0.2 (-7) $(T/300)^{-1}$
Chan [33]	2.8 ± 0.2 (-7)
G. E. Report [34]	2 ± 2 (-8) $(T/300)^{-1}$ to
	4 ± 4 (-8) $(T/300)^{-1}$
Biondi [35]	1.9 (-7)
Wickwar [36]	1.95 (-7) $(300/T)^{0.7}$

a. Value in ( ) denotes the order of rate coefficient; e.g., 2 (-7) means 2×10^{-7}.

TABLE 2. VALUES OF RATE COEFFICIENT, α_1, FOR DISSOCIATIVE RECOMBINATION OF NO^+ PRODUCTION MECHANISM

$NO^+ + e \xrightarrow{\alpha_1} N + O(^1D)$	
Nicolet and Aikin [20]	3 (-9)[a]
Gunton and Inn [37]	1.3 (-6)
Lin [38]	1 (-9) at 5000 K
Syverson, Stern, Shaw, Scheibe and Gunton [39]	1.3 (-7) at 3000 K
Doering and Mahan [40]	4 (-7)
Norton, Van Zandt, and Denison [25]	6.7 (-8) (300/T)
Dalgarno and Walker [11]	Spin forbidden
Swider [27]	~ 1 (-7)
Saxena [41]	2.8 (-7)
Weller and Biondi [42, 43]	7.4 ± 0.7 (-7) at 200 K
	4.1 (+0.3, -0.2) (-7) at 300 K
	3.1 ± 0.2 (-7) at 400 K
	$4.1\ (+0.3, -0.2)\ (-7)\ (T/300)^{-1}$
Bardsley [44]	2.6 (-7) at 300 K
G.E. Report [34]	$5.0 \pm 1\ (-7)(T/300)^{-1.2 \pm 0.2}$
Wickwar [36]	4.1 (-7) (300/T)
Meira, Jr. [45]	4.5 (-7) (300/T)

[a] Value in ( ) denotes the order of rate coefficient; e.g., 2 (-7) means 2×10^7.

Values of rate coefficients for these reactions are listed in Tables 3 and 4, respectively. These values, which were obtained by an extensive literature survey, were used parametrically in this study in an effort to establish "best" values.

Additional sources and sinks of these molecular ions that were obtained during the literature survey as well as postulated values of their reaction rate coefficients are listed in Table 5 for completeness; however, the production or loss mechanisms themselves were determined to be of minor importance in the twilight glow, because either the rate coefficient was small in comparison with other coefficients or the combination of the reactant number densities and the rate coefficient made the mechanism ineffective at the altitudes from which the 6300 Å radiation emanates during the twilight period.

D. Photoelectron Impact Excitation

Hanson [53] noticed that photoelectrons emitted above a certain altitude could escape from the sunlit atmosphere, travel along the magnetic field lines, and be injected into the conjugate atmosphere. Cole [54] then suggested that Barbier's subpolar sheet (pre-dawn enhancement of 6300 Å OI emission) could be caused by conjugate point photoelectrons causing an increase in the local electron temperature, thereby producing an increase in the rate of production of O^1D atoms by collisions between fast thermal electrons and ground state oxygen atoms. This suggestion was contested by Carlson [55] who first reported observations of pre-dawn heating of the ionosphere over Arecibo, P.R., and then showed [56] that the enhancement of the 6300 Å OI emission had to be due to direct impact excitation of atomic oxygen to the ^1D state by the incident conjugate point photoelectrons rather than the fast thermal electrons. This result was later supported by the theoretical studies of Fontheim, Beutler, and Nagy [86]; the analysis of simultaneous photometer and Thomson scatter observations by Duboin, Lejeune, Petit, and Weill [87]; and the 100 R enhancements reported by Cogger and Shepherd [88]. If the enhancement of O^1D emission had been due to heating as proposed by Cole [54], then Duboin, Lejeune, Petit, and Weill [87] should have observed only a 3 R enhancement instead of the 40 to 50 R enhancement they reported. Added evidence in support of the direct impact excitation mechanism comes from Wallace and McElroy [12] who concluded from their analysis of the measurements from five rocket-borne photometers that this mechanism is significant in the day glow, confirming the suggestions of Fournier and Nagy [89]. It appears as if the major portion of the post-twilight and pre-dawn enhancements cannot be attributed to the fast thermal electron mechanism proposed by Cole [54].

TABLE 3. VALUES OF RATE COEFFICIENT, γ_2, FOR $O_2 + O^+$ CHARGE EXCHANGE REACTION

$O_2 + O^+ \xrightarrow{\gamma_2} O_2^+ + O$	
Bates and Nicolet [57, 58]	1 (-12)[a]
Dickinson and Sayers [59]	2.5 ± 0.4 (-11)
Danilov [22]	1 (-10)
Hertzberg [60]	1 (-9)
Langstroth and Hasted [61]	1.8 ± 0 2 (-12)
Fite, Rutherford, Snow, and Van Lint [62]	≥ 1 (-10)
Norton, Van Zandt, and Denison [25]	5 (-11)
Whitten and Poppoff [63]	2 (-11)
Swider [27]	3 (-12)
Fehsenfeld, Schmeltekopf, and Ferguson [64]	4.0 (-13)
Donahue [65]	3.4 (-11)
Copsey, Smith and Sayers [66]	2 (-13)
Warneck [67]	2 (-13)
Bohme [68]	2 (-11)
Strobel [69]	1.15 (-11) (600/T)
Smith and Fouracre [70]	3.4 ± 0.5 (-10) $T^{(-0.48 \pm 0.5)}$
G.E. Report [34]	2 (-11)
Stubbe [71]	1.16 (-11) (1 + T/1660)
Bates [72]	2 (-11)
Forbes [52]	2 (-11) increases slightly with temperature
Strobel and McElroy [73]	1.07 (-9) $T^{-0.7}$
Meira, Jr. [45]	2 (-11)
Biondi [35]	4 (-11)

[a] Value in ( ) denotes the order of rate coefficient; e.g., 2 (-7) means 2×10^{-7}.

TABLE 4. VALUES OF RATE COEFFICIENT, γ_1, FOR $N_2 + O^+$ ION-ATOM INTERCHANGE REACTION

$O^+ + N_2 \xrightarrow{\gamma_1} NO^+ + N$	
Potter [74]	~1 (-8)[a]
Krassovsky [75]	~1 (-10)
Bates and Nicolet [57, 58]	~1 (-13)
Hertzberg [60]	~1 (-9)
Danilov [22]	~1 (-10)
Langstroth and Hasted [61]	4.7 ± 0.5 (-12)
Norton, Van Zandt, and Denison [25]	1 (-12)
Whitten and Poppoff [63]	2 (-12)
Swider [27]	3 (-13)
Fehsenfeld, Schmeltekopf, and Ferguson [64]	3 (-12)
Copsey, Smith, and Sayers [66]	2.4 (-12)
Aquilanti and Volpi [76]	5.0 ± 3 (-12)
Donahue [65]	1.8 (-12)
Warneck [67]	2 (-12)
Paulson, Dale, and Murad [77]	1.5 (-12)
Norton [78]	2 (-12)
Schmeltekopf, Fehsenfeld, Gilman, and Ferguson [79]	1.8 (-12)
Smith and Fouracre [70]	2.4 (-12)
G. E. Report [34]	1 (-12 ± 0.5)
Saxena [41]	3 (-12)
Stubbe [71]	1 (-12)
Bates [72]	1.2 (-12)

a. Value in ( ) denotes the order of rate coefficient; e.g., 2 (-7) means 2×10^{-7}.

TABLE 5. OTHER SOURCES AND SINKS AND ASSOCIATED VALUES OF THEIR REACTION RATE COEFFICIENTS

$O_2^+ + N_2 \rightarrow NO^+ + NO$	
Fite, Rutherford, Snow, and Van Lint [62]	Very slow compared with charge transfer or ion atom interchange
Ferguson, Fehsenfeld, Goldan, and Schmeltekopf [80]	<1 (-15)[a]
Warneck [67]	<3 (-15)
G. E. Report [34]	1 (-17 ± 2)
Bates [72]	<1 (-15)
$O_2 + N^+ \rightarrow O_2^+ + N$	
Danilov [22]	5.0 (-10)
Fehsenfeld, Schmeltekopf, and Ferguson [64]	5.0 (-10)
Copsey, Smith, and Sayers [66]	4.5 (-10)
Warneck [67]	4 (-10)
Saxena [41]	5.0 (-10)
G. E. Report [34]	5 ± 1.5 (-10)
$O_2^+ + e \rightarrow O_2 + h\nu$	
Nicolet and Swider [81]	1-5 (-12) radiative recombination can be neglected
Chan [33]	2.8 ± 0.2 (-7)
G. E. Report [34]	1 (-12 ± 1) $(T/300)^{-0.7 \pm 0.5}$

[a] Value in ( ) denotes the order of rate coefficient; e.g., 2 (-7) means 2×10^{-7}.

TABLE 5. (Continued)

$NO^+ + e \rightarrow NO + h\nu$	
Nicolet and Swider [81]	1-5 (-12)[a] radiative recombination can be neglected
G. E. Report [34]	$1\ (-12 \pm 1)\ (T/300)^{-0.7 \pm 0.5}$
$O_2^+ + e \rightarrow O_2 + h\nu$	
Nicolet and Swider [81]	1-5 (-12) radiative recombination can be neglected
Chan [33]	2.8 ± 0.2 (-7)
G. E. Report [34]	$1\ (-12 \pm 1)\ (T/300)^{-0.7 \pm 0.5}$
$NO + N_2^+ \rightarrow NO^+ + N_2$	
Ferguson, Fehsenfeld, Goldan, and Schmeltekopf [80]	5 (-10)
Goldan, Schmeltekopf, Fehsenfeld, Schiff, and Ferguson [82]	5 (+1, -3) (-10)
Warneck [67]	4.8 (-10)
G. E. Report [34]	5.0 ± 1.5 (-10)
McGowan [83]	5 (-10)
Fehsenfeld, Dunkin, and Ferguson [84]	3.4 (-10) ± 30%
Bates [72]	5.0 (-10)
$N_2^+ + O \rightarrow NO^+ + N$	
Norton, Van Zandt, and Denison [25]	2 (-11)
Ferguson, Fehsenfeld, Goldan, Schmeltekopf, and Schiff [85]	2.5 ± 1 (-10)

[a] Value in ( ) denotes the order of rate coefficient; e.g., 2 (-7) means 2×10^{-7}.

TABLE 5. (Continued)

$N_2^+ + O \rightarrow NO^+ + N$ (continued)	
Wallace and McElroy [12]	7 (-11)[a]
Saxena [41]	2.5 (-10)
G. E. Report [34]	2.5 ± 0.8 (-10)
Fehsenfeld, Dunkin, and Ferguson [84]	1.4 (-10)
Bates [72]	2.5 (-10)
$N_2^+ + O_2 \rightarrow N_2 + O_2^+$	
Danilov [22]	1 (-10)
Fite, Rutherford, Snow, and Van Lint [62]	2 (-10)
Fehsenfeld, Schmeltekopf, and Ferguson [64]	1.0 ± 0.5 (-10)
Wallace and McElroy [12]	8.6 (-11)
Aquilanti and Volpi [76]	6.5 (-11)
Warneck [67]	1.1 (-11)
G. E. Report [34]	2 ± 1 (-10)
Bates [72]	4.7 (-11)
Meira, Jr. [45]	1 (-10)
$O_2^+ + NO \rightarrow NO^+ + O_2$	
Ferguson, Fehsenfeld, Goldan, and Schmeltekopf [80]	8 (-10)
Warneck [67]	7.7 (-10)

[a] Value in ( ) denotes the order of rate coefficient; e.g., 2 (-7) means 2×10^{-7}.

TABLE 5. (Concluded)

O_2^+ + NO → NO^+ + O_2 (continued)	
Goldan, Schmeltekopf, Fehsenfeld, Schiff, and Ferguson [82]	8 (+2, -5) (-10)[a]
G. E. Report [34]	8.0 ± 2.4 (-10)
Fehsenfeld, Dunkin, and Ferguson [84]	6.3 (-10) ± 30%
Bates [72]	8 (-10)

a. Value in ( ) denotes the order of rate coefficient; e.g., 2 (-7) means 2×10^{-7}.

A third source, increased ionospheric recombination due to a lowering of the F-region, has been proposed by Noxon and Johanson [90], Nichol [91], and Pal [92]. All but approximately 20 R of the pre-dawn enhancement observed over Blue Hill, Massachusetts, could be accounted for by this source when the conjugate point was still in darkness, although there were a few enhancements that could not be attributed to any of these sources. While most of the 40 R enhancement over Hobart, Tasmania, could be attributed to this source, Nichol [91] also concluded that (1) ionization from the exosphere cascading down into the F-region after the rapid cooling at sunset, as postulated by Evans [93], was a second possible source and (2) conjugate point photoelectrons were a third source, although there was not a consistent correlation between the onset of the enhancement and conjugate point sunrise. In view of the recent results of Hernandez[1] concerning possible contamination of observations of 6300 Å OI emission by the 9-3 OH band, which are discussed in detail in Appendix D, the possibility that some of these apparently inexplicable enhancements reported by Noxon and Johanson [90] as well as the inconsistency between onset time and conjugate point sunrise observed by Nichol [91] may be due to increases in the intensity of the hydroxyl emission cannot be ruled out, even though the time inconsistency does seem to be related to the state of the local ionosphere [91]. The amount of enhancement attributed by these investigators to direct impact excitation by conjugate point photoelectrons is in excellent agreement with the results of theoretical studies by Sudworth [94] and by Nagy and Banks [95] who showed that 13 to 25 R enhancements are possible depending upon the local atmospheric conditions.

---

[1] Hernandez, G.: Contamination of the OI ($^3P_2$-$^1D_2$) Emission Line by the (9-3) Band of OH × $^2\pi$ in High Resolution Measurements of the Night Sky. Unpublished, 1973.

The analyses of both Nichol [91] and Noxon and Johanson [90] suffer from a lack of observational data required to positively determine the exact amount of the observed intensity due to each of the postulated sources. Neither Nichol [91] nor Noxon and Johanson [90] had measurements of the temperatures of either the neutral or charged portions of the local atmosphere which are required to monitor changing conditions of the environment of the observation point nor did they have measurements of the conjugate point photoelectron fluxes. The analysis of the pre-dawn enhancement over Arecibo, P.R., by Wickwar [36] was based on the most complete set of observational data since he did have the necessary electron density data, including data from above the F_2 peak, and measurements of conjugate point photoelectron fluxes, although he did not have the required temperature measurements either. His analysis showed that when the conjugate point solar zenith angle was greater than 105°, the Arecibo night glow intensity could be explained by the dissociative recombination process. However, the difference between theoretical calculations and observations increased with decreasing conjugate point solar zenith angle until a plateau of 25 to 50 R was reached at approximately at an angle of 95°, supporting Carlson's [96] report that the pre-dawn enhancement over Arecibo began at a conjugate point solar zenith angle of approximately 99°. Day-to-day variations in the onset time (angle) and intensity were highly correlated with the ionospheric conditions at the observation point in agreement with the report of Okuda and Misawa [97] that when the sunspot number was higher the onset time for pre-dawn enhancements over the Takhatta Night Glow Observatory during the period from November 1966 to February 1968 was earlier (solar activity effect on environment of the observation point).

Several investigators have reported on the possibility of geomagnetic field control of the location of enhancements. Bennett [98] found a 100 R twilight enhancement at solar cycle maximum and a 50 R enhancement at solar cycle minimum due to conjugate point photoelectrons. He concluded that enhancement could not occur at locations with $L \leq 1.1$ because the low minimum altitude of the $L = 1.1$ shell at 50°W resulted in too many collisions for the photoelectrons to be able to propagate from the conjugate point, nor could they occur at locations with $L > 3.2$ because the electric fields at the plasma-pause [99] would prevent propagation from the conjugate point. Contrary to this, Torr and Torr [100] found a 50 R twilight enhancement in winter at the Antarctica station SANAE, which lies on $L = 4.0$; Cogger and Shepherd [88] reported an enhancement at Saskatoon which lies on $L = 4.2$; and Nichol [91] found that the poleward cutoff of the enhancement was nearer $L = 4.0$ than $L = 3.2$. A solar activity dependent position for the plasmapause could reconcile this apparent discrepancy in the poleward cutoff for possible enhancements; however, there are still insufficient observational data to verify Bennett's [98] conjecture concerning the low latitude cutoff.

Huntsville, Alabama, is on approximately the 2.3 to 2.4 L-shell, and its conjugate point is approximately 47°S and 105°W [101]. Figure 2 shows the variation of the conjugate point solar zenith angle as a function of Central Standard Time for the night of January 6-7, 1972. If conjugate point photoelectrons are present on this night, they should affect the computational results until approximately 2233 Central Standard Time, which is conjugate point sundown, assuming a screening height of 180 km.

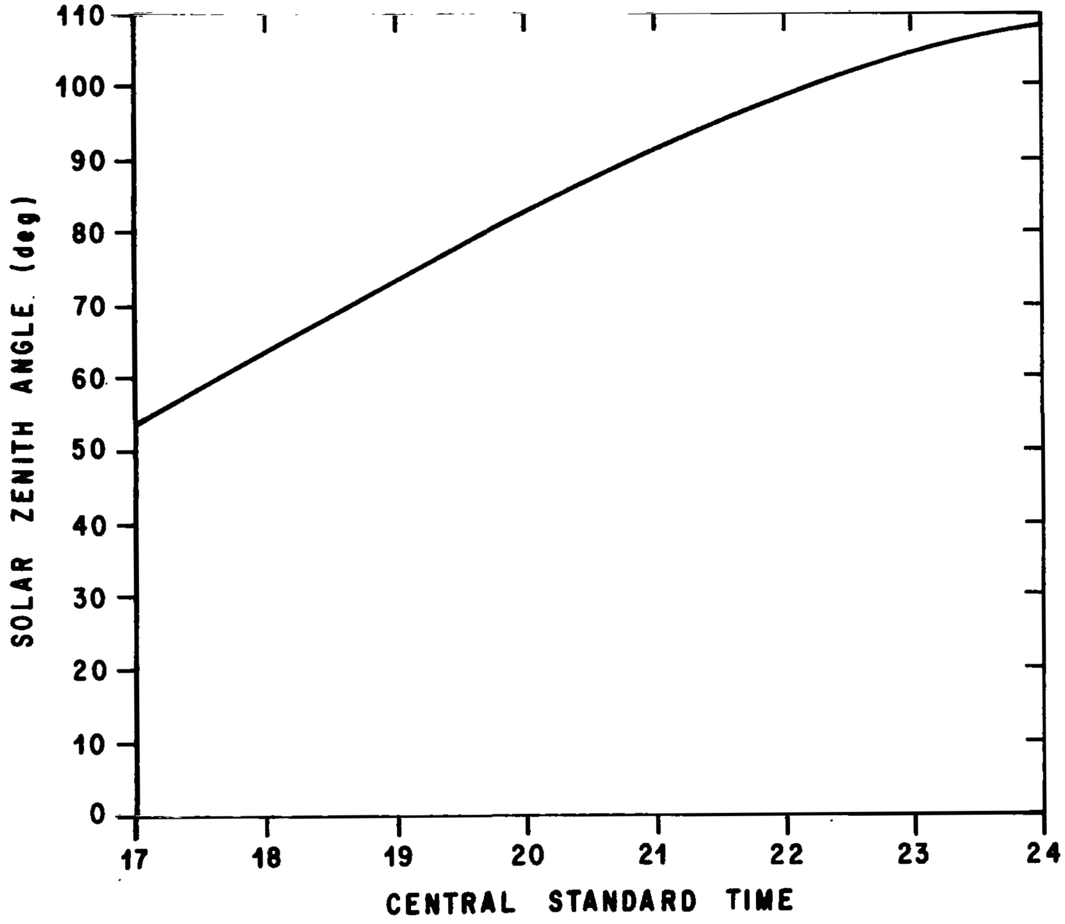

Figure 2. Conjugate point solar zenith angle as a function of Central Standard Time on January 6-7, 1972.

E. Quenching

The metastable ^1D oxygen atom has a lifetime of approximately 110 s and will probably emit a 6300 Å photon unless it is collisionally deactivated or quenched. The exact process for the quenching, which seems to be a more appropriate term for the process, is still undetermined since the ^1D state is so reactive and the emissions are very difficult to observe under laboratory conditions where rate coefficients can be measured. At the current time, N_2, O_2, O, and electrons are postulated to be the primary quenching agents. However, the rate coefficient for the $O(^1D) + O$ process is relatively slow while the electron number densities rarely exceed 10^6 cm^{-3} at night; therefore, these latter two agents do not contribute to the overall quenching process.

Rate coefficients for the first three of these quenching agents are listed in Tables 6, 7, and 8, respectively. Quenching by both N_2 and O_2 was considered to be of importance in the twilight glow; consequently, the reactions listed below were included in the computational procedure used in this study with the appropriate rate coefficients used parametrically in order to establish "best" values.

$$O(^1D) + N_2 \longrightarrow O(^3P) + N_2^* \qquad (11)$$

$$O(^1D) + O_2 \longrightarrow O(^3P) + O_2^* \qquad (12)$$

The effects of differences in the quenching rate coefficients on calculated volume emission profiles as well as integrated intensities are discussed in Section VII.

III. INSTRUMENTATION AND OBSERVATIONS

A. Instrumentation

A general purpose airglow observatory system [123] has been established at the Marshall Space Flight Center, Alabama, to study optical emissions of the night sky. In this report the system has been used to study post-sunset twilight behavior of the 6300 Å emission of atomic oxygen. The system consists of an airglow observatory, a C-4 vertical incidence ionosonde, and a phase path sounder; however, the phase path sounder was not in operation during the period of this study.

TABLE 6. VALUES OF RATE COEFFICIENT, q_1, FOR $O(^1D)$ + N_2 QUENCHING REACTION

$O(^1D) + N_2 \xrightarrow{q_1} O(^3P) + N_2^*$	
DeMore and Raper [102, 103]	3 (-11)[a]
Hunt [104]	5 (-15)
Hunten and McElroy [105]	5 (-11)
Snelling and Bair [106]	2.2 ± 1 (-11)
McGrath and McGarvey [107]	3 (-11)
G. E. Report [34]	5 (-11 ± 0.5)
Young [108]	5 (-11)
Noxon [109]	5 (-11)
Peterson and Van Zandt [110]	5 (-11) - 1 (-10)
Dalgarno [111]	Most $O(^1D)$ are quenched by N_2
Forbes [52]	3 (-11) - 7 (-11) 5 (-11) - 1 (-10) with negligible temperature dependence
Schaeffer, Feldman, and Fastie [112]	6 (-11) - 7 (-11)
Donahue, Parkinson, Zipf, Doering, Fastie, and Miller [49]	5 (-11) - 1 (-10)
Biondi [35]	4.4 (-11)
Hernandez [113]	$9\begin{pmatrix}+1.0\\-0.5\end{pmatrix}(-11)$

a. Value in ( ) denotes the order of rate coefficient; e.g., 2 (-7) means 2×10^{-7}.

TABLE 7. VALUES OF RATE COEFFICIENT, q_2, FOR $O(^1D) + O_2$ QUENCHING REACTION

$O(^1D) + O_2 \xrightarrow{q_2} O(^3P) + O_2^*$	
Wallace and Chamberlain [114]	4 (-12) - 2 (-10)[a]
Dalgarno and Walker [11]	4 (-12) - 2 (-10)
DeMore and Raper [102, 103]	3 (-11)
Zipf [115]	4 (-12) - 2 (10)
Peterson, Van Zandt, and Norton [116]	> 1 (-11)
Hunten and McElroy [105]	4 (-15)
Hunt [104]	2.5 (-14)
Warneck and Sullivan [117]	4 (-15)
Snelling and Bair [118]	2 (8) liter $mole^{-1}$ s^{-1}
G. E. Report [34]	1 (-12 ± 2) - 1 (-10 ± 2)
Gilmore, Bauer, and McGowan [119]	> 1 (-11)
Zipf [120]	1 (-11)
Young, Black, and Slanger [108]	4 (-11)
Noxon [121]	6 (-11)
Biondi [35]	4.4 (-11)
Hunt [122]	5 (-12)

a. Value in ( ) denotes the order of rate coefficient; e.g., 2 (-7) means 2×10^{-7}.

TABLE 8. VALUES OF RATE COEFFICIENT, q_3, FOR $O(^1D)$ + O QUENCHING REACTION

$O(^1D) + O(^3P) \xrightarrow{q_3} 2\,O(^3P)$	
Hunten and McElroy [105]	1.6 (-13)[a]
G. E. Report [34]	1.3 (-13 ± 0.5)
Gilmore, Bauer, and McGowan [119]	< 4 (-13)

[a] Value in ( ) denotes the order of rate coefficient; e.g., 2 (-7) means 2×10^{-7}.

Three optical measurements are required in this study: (1) the intensity of the 6300 Å emission, (2) the intensity of the background emission — in this study the 6100 Å emission is considered to be representative, and (3) the Doppler broadening of the 6300 Å emission line. Roble, Hays, and Nagy [124] have shown that this Doppler broadening of the emission line is due to the thermal motions of the metastable $O(^1D)$ oxygen atoms and that it is an accurate measure of the temperature of the neutral atmosphere at approximately the base of the exosphere. The variation of the neutral exospheric temperature during the post-sunset twilight period can be monitored by observing the 6300 Å Doppler temperature of the normal night glow.

The C-4 vertical incidence ionosonde has been used to obtain electron density-height profiles for use in the dissociative recombination portion of the theoretical model of the twilight 6300 Å emission. Since the C-4 ionosonde is only capable of making vertical soundings, only vertical scans of the 6300 Å emission have been used in this study.

1. AIRGLOW OBSERVATORY

The airglow observatory itself consists of an interference filter photometer after Purdy et al. [125] and a Fabry-Perot interferometer after Roble [123]. The photometer is capable of measuring the intensity of the night glow at four wavelengths — 5300 Å, 5577 Å, 6100 Å, and 6300 Å; however, only the latter two measurements have been used in this study. The Fabry-Perot interferometer is capable of measuring the Doppler broadening of both the 5577 Å and 6300 Å emissions from the night glow; however, only the latter wavelength emission has been used in this study. Both of these instruments, their design considerations, construction, and operating capabilities were discussed in detail in Reference 123; however, pertinent portions of that document have been included here for completeness. The suitability and capability of the instruments for making the required measurements as well as the representativeness of the observations have been well documented; therefore, they will not be discussed in detail here. Instead, the interested reader is referred to Born and Wolf [126]; Tolansky [127]; Jenkins and White [128]; Turgeon and Shepherd [129]; Wark [130]; Jarrett, Hoey, and Paffrath [131]; Jarrett and Hoey [132]; Hernandez [113]; Biondi and Feibelman [17]; Roble, Hays, and Nagy [124]; and Roble [123].

a. Fabry-Perot Interferometer. This instrument is a conventional, pressure scanned, multiple beam interferometer. A simplified block diagram of the instrument and its supporting systems is shown in Figure 3. The primary components of the instrument are a high quality set of fused quartz etalon plates with plane surfaces carefully polished flat to 1/200 of a wavelength and a very sensitive photoelectrically cooled photomultiplier tube. The plates are 15 cm in diameter and are separated by a 1 cm spacer which Roble [123] showed to be the optimum for measuring the 6300 Å emission. Recent observations have shown that this may have been an erroneous conclusion. This is discussed in detail in Appendix D. The operating parameters of the system are shown in Table 9.

Data from this pulse counting system are displayed on a scaler-timer, recorded on a strip chart recorder and an X-Y plotter, and written on a digital magnetic tape.

(1) Data Reduction Procedure. The recorded signal output of the 6300 Å emission line is adequately represented by the following equation which is described in detail by Hays and Roble [133]:

$$Y(x) = I_0 \left[A_0 + \sum_{n=1}^{\infty} A_n \exp\left(-\frac{n^2}{4} \gamma T_n\right) \cos nx \right] + C \quad , \qquad (13)$$

where

x is the phase difference;

$$I_0 = 5 \times 10^5 A\Omega \, R_y \, \tau_a \, T_T \, P_e \, (1 - R) \, (1 + R)^{-1} \qquad (14)$$

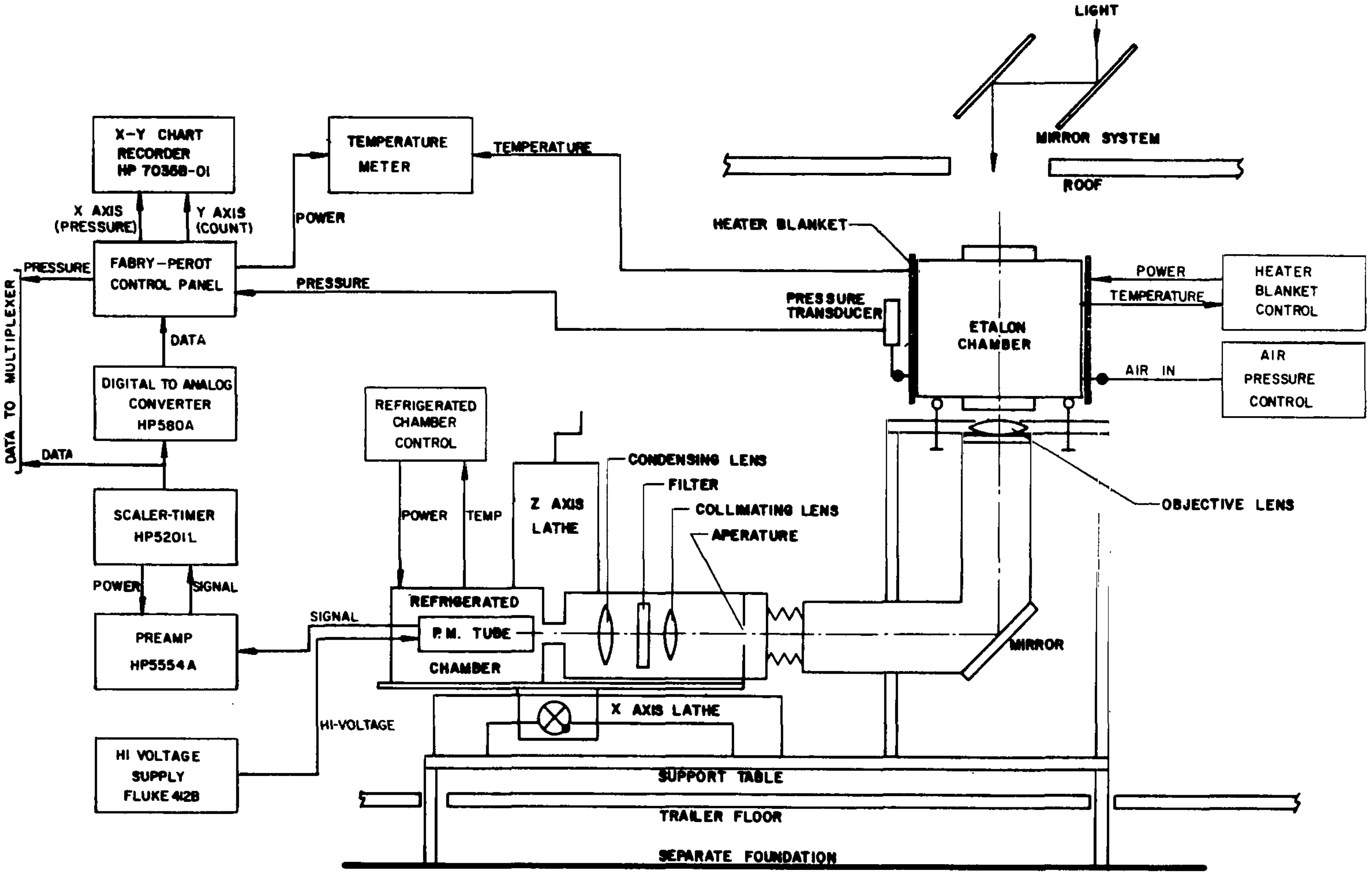

Figure 3. Schematic drawing of the Fabry-Perot interferometer and associated system components [123].

TABLE 9. OPERATING PARAMETERS OF THE FABRY-PEROT INTERFEROMETER

1. Etalon Plates	
Effective diameter	5.25 in.
Flatness	$\lambda/200$
Roughness defect, N_{D_g}	40
Reflective coatings	Five alternate layers of ZnS and cryolite
Reflectivity	0.8275
Reflective finesse, N_R	19.3
Spherical defect finesse, N_{D_f}	17.3
Spacing, t	1 cm
2. Objective Lens	48 in. (achromat)
Diameter	6 in.
3. Aperture	
Diameter	11/64 in.
Finesse	19.6
4. Instrument Field of View	0.2°
5. Interference Filter	
Diameter	2 in.
Half-width	5.2 Å
Peak transmission	55%
Peak wavelength	6307 Å

TABLE 9. (Concluded)

6. Photomultiplier (ITT-FW-130)	
Quantum efficiency at 6300 Å	5%
Photocathode surface	S-20
Effective aperture	1/10 in.
Dark count (cooled to -15°C) (uncooled)	1 to 2 counts/s 80 to 90 counts/s
7. Resolving Power	350 000
8. Operating Order	31 700
9. Free Spectral Range	0.198 Å ($0.5\ \mathrm{cm}^{-1}$)
10. Scanning Gas	(Dry nitrogen)
11. Pressure Change for One Order	1.76 psi
12. Overall Instrument Finesse	10.00

where A is the effective collecting area of the interferometer, Ω is the instrument field of view, R_y is the brightness of the source in Rayleighs, τ_a is the transmission coefficient that includes the effects of absorption and scattering of the reflective coatings, T_T is the transmission of the various optical surfaces of the instrument and pre-monochromator, and P_e is the quantum efficiency of the photomultiplier tube;

$$A_0 = \pi/2 \qquad ;$$

$$A_n = \pi^{-1} R^n \exp[-(n^2/4) D^2] \operatorname{sinc}(2nd_f/\Delta\sigma) \operatorname{sinc}(2nf/\Delta\sigma) \quad , \qquad (15)$$

where R is the reflectivity of the etalon plates, $D = 2\pi d_g/(\Delta\sigma\sqrt{\ln 2})$ with d_g being the half-width at half-height of the gaussian surface defect function, d_f is half-width at half-height of the spherical defect function, $\Delta\sigma$ is the free spectral range of the instrument, sinc $\beta = (\sin \pi\beta)/(\pi\beta)$, and f is half-width at half-height of the aperture function;

n is the number of Fourier transforms required to describe the line shape;

$$\gamma = 7.274 \times 1^{-12} M^{-1} \sigma_0 (\Delta\sigma)^{-2} \quad , \tag{16}$$

where M is the molecular weight of the emitting atom and σ_0 is the emission wave number;

T_n is the neutral gas temperature (K) ;

and

C is the continuum background.

Equations (13) and (14) were combined and solved for R_y using the following values for the various instrument parameters described previously in conjunction with the observed intensity of the 6300 Å emission above the background continuum:

$$A\Omega = 1.396 \times 10^{-3} \quad ,$$

based on an aperture with a diameter of 0.436 cm, an objective lens with a 121.9 cm focal length, a full field of view of 0.2°, and an effective diameter of the etalon plates of 13.3 cm;

$\tau_a = 1$;

$P_e = 0.05$;

and

T_T = 0.2139 based on the following.

	Optical Component	Transmission
(a)	Glass plate on top of etalon	0.91
(b)	Quartz etalon surface 1	0.91
(c)	Quartz etalon surface 2	0.91
(d)	Glass plate below etalon	0.91
(e)	Objective lens	0.91
(f)	Mirror	0.91
(g)	Collimating lens	0.91
(h)	6300 Å filter	0.55
(i)	Condensing lens	0.91
(j)	Plexiglass surface 1	0.91
(k)	Plexiglass surface 2	0.91

The instrument is designed so that the scanning is accomplished by changing the N_2 pressure in the chamber linearly with time, similar to the method discussed by Noxon and Johanson [133a].

b. Photometer. The photometer in the airglow observatory is of the turret type designed by Purdy, Megill, and Roach [125]. It has space for six interference filters in a wheel that is driven by a variable speed reversible stepping motor. This wheel positions an interference filter in front of a photomultiplier tube and then a second wheel positions in succession a dark reference, a standard light source, and a sky opening between the interference filter and the mirror system that collects the light. Once this procedure is completed, a second filter is moved into position and the entire process is repeated. This continues uninterrupted during the periods in which measurements are being made.

The standard light source is a C^{14}-activated phosphor [134-136] which provides a light of known intensity in the 4000 to 8000 Å spectral range. E. Marovich of Fritz Peak Observatory calibrated the source against a primary standard and its intensity distribution as shown in Table 10 and Figure 4. The photometer-telescope system has a 5° field of view and it uses the same scanning mirror system as the Fabry-Perot interferometer by having a 45° mirror that projects out into, but does not interfere with, the light path from the scanning mirror to the Fabry-Perot interferometer. Data from the pulse counting system of the photometer are displayed on a scaler-timer, recorded on a strip-chart recorder, and written on a digital magnetic tape.

(1) Data Reduction Procedure. The 6300 Å emission line observations were combined with the 6100 Å continuum observations to determine the intensity of the atomic oxygen redline E(6300) in a computer program using the following equation developed in Reference 123:

$$E(6300) = \frac{(S_{ss} - S_d)\bar{C}_s}{(S_{sc} - S_d)} - \frac{(S_{cs} - S_d)\,\bar{C}_c}{(S_{cc} - S_d)} \quad , \qquad (17)$$

where S_{ss} is the sky signal from the emission line filter, S_{sc} is the calibration signal from the emission line filter, S_{cs} is the sky signal from the continuum filter, S_{cc} is the calibration signal from the continuum filter, S_d is the dark signal of the photomultiplier tube, and $\bar{C}_s$ and $\bar{C}_c$ are the mean values of the standard light spectral characteristics over the wavelength region of the emission line and the continuum as modified by the filters, respectively.

B. Observational Measurements

1. INTENSITY

The Fabry-Perot interferometer and the turret photometer were operated during the twilight and post-twilight periods on several days in the winter and spring of 1971-1972. The days on which they were operated, the time periods covered by the operation, and the solar activity indices existing at the time of their operation are listed in Table 11. The photometer system has a 30 Å bandpass 6300 Å filter and measurements are possibly contaminated by other

TABLE 10. LOW BRIGHTNESS SOURCE INTENSITY DISTRIBUTION

Date: March 1, 1972

Calibration of Phosphor Light: NASA Huntsville Temperature 17°C

NRD C-3002-a
Serial D-010 3-71

Wavelength (Å)	Radiance (W cm^{-2}sr^{-1}Å^{-1} × 10^{-13})	R/Å	Wavelength (Å)	Radiance (W cm^{-2}sr^{-1}Å^{-1} × 10^{-13})	R/Å
3800	0.03	0.072	6000	1.68	6.38
3900	0.05	0.123	6100	2.07	7.99
			6200	2.34	9.18
4000	0.17	0.430	6300	2.49	9.93
4100	0.44	1.14	6400	2.46	9.97
4200	0.82	2.18	6500	2.43	10.00
4300	1.16	3.16	6600	2.32	9.69
4400	1.25	3.48	6700	2.02	8.57
4500	1.25	3.56	6800	1.75	7.53
4600	1.06	3.09	6900	1.52	6.64
4700	0.88	2.62			
4800	0.73	2.22	7000	1.43	6.34
4900	0.68	2.11	7100	1.09	4.90
			7200	0.92	4.19
5000	0.72	2.28	7300	0.73	3.37
5100	0.68	2.20	7400	0.53	2.48
5200	0.68	2.24	7500	0.41	1.95
5300	0.67	2.25	7600	0.34	1.64
5400	0.62	2.12	7700	0.23	1.12
5500	0.61	2.12	7800	0.24	1.18
5600	0.62	2.20	7900	0.12	0.600
5700	0.78	2.81			
5800	1.01	3.71	8000	0.28	1.42
5900	1.32	4.93			

Notes:
1. The units of radiance are watts per square centimeter per steradian per Angstrom.
2. The precision is to within approximately 10 percent; precision is worse toward each end of the wavelength range, especially beyond approximately 7500 Å.
3. The accuracy is to within approximately ±10 percent; this is based on a partial comparison of the standards.

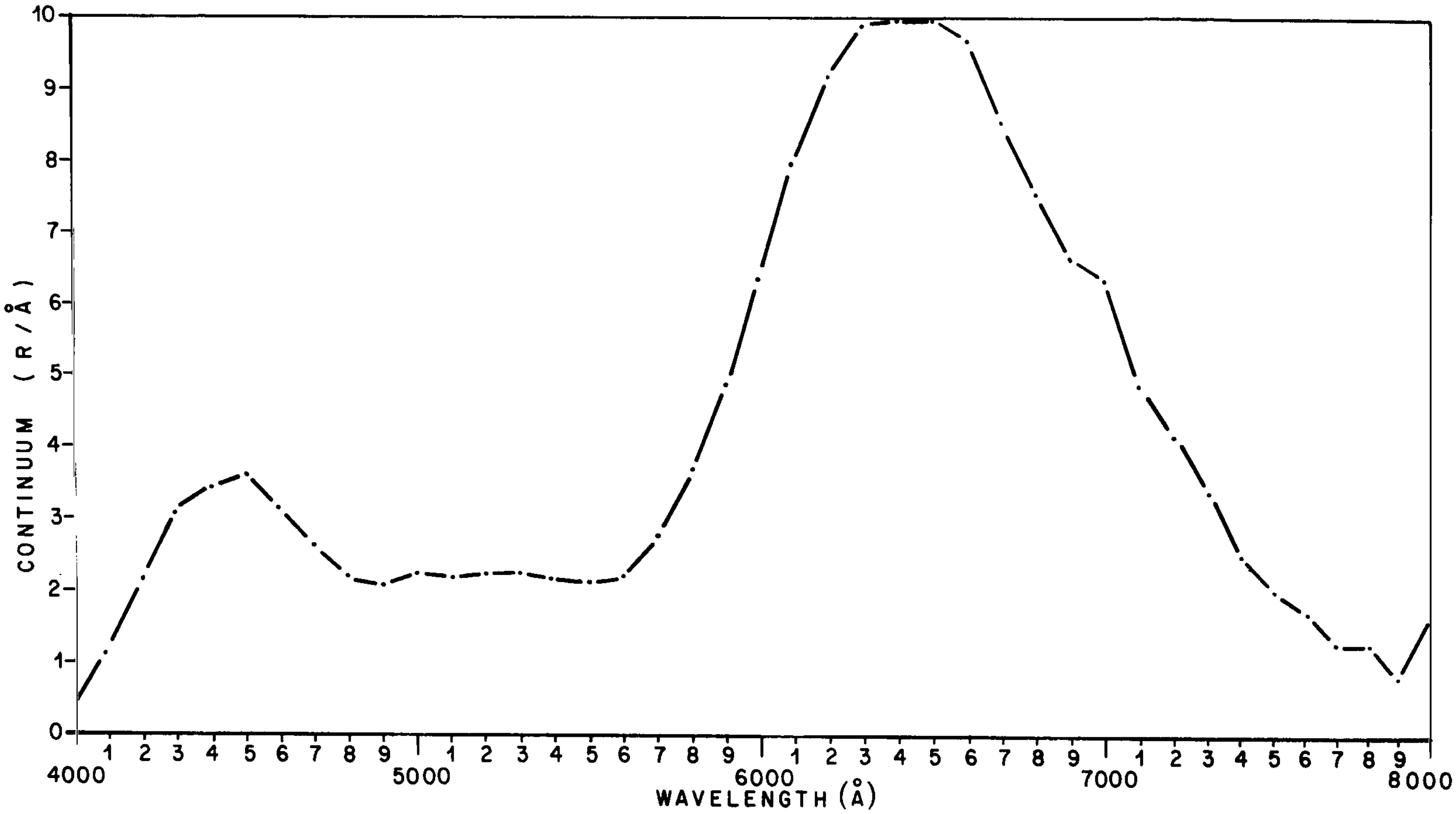

Figure 4. Low brightness source intensity distribution.

TABLE 11. OPERATION LOG

Date	Time Period	Daily 10.7 cm Flux	81 Day Mean Flux	Kp (6.7 h lag)
Nov. 10, 1971	1832-0500	104.8	109.0	0.7
Nov. 17, 1971	1720-1920	107.9	106.1	0
Dec. 1, 1971	1712-1743	120.3	110.5	1.0
Jan. 6, 1972	1726-2400	106.6	117.7	0.3
Jan. 7, 1972	1726-2400	106.5	119.0	0.4
Feb. 4, 1972	1749-1949	106.6-105.6	119.1	2.7-1.0
Feb. 7, 1972	1745-1930	105.0	119.1	1.0
Feb. 14, 1972	1752-1952	140.2	119.2	1.0

emissions; therefore, the intensity values derived using the procedures described previously may not be true values for the atomic oxygen redline. A more detailed discussion of the contaminating hydroxyl emission is given in Appendix D. Each filter in the photometer is calibrated with the low brightness source (LBS) immediately after each sky reading and there are only two optical surfaces that must be correctly accounted for in the data reduction scheme, the filter and a single mirror, because the scanning mirror system was not used for the overhead scans.

Although the Fabry-Perot interferometer (F-P) has a 5.2 Å half-width interference filter that will screen out some more of the contaminating emissions from nearby hydroxyl lines, it has 11 optical surfaces that are subject to variations with time. Therefore, intensities of the atomic oxygen redline emissions were calculated by normalizing the intensities derived from the F-P measurements using the procedure discussed in Section III.A.1.a.(1) to the photometer intensities during the 2300 to 2330 CST time period where the hydroxyl contamination should be minimal and then using the normalization factor to correct the remaining intensities calculated from the F-P measurements. This is similar to the technique employed by Noxon and Johanson [133a]. Since all of the observations used in this analysis were made at the zenith, no corrections were made for extinction. It is believed that errors resulting from this procedure are rarely more than 10 percent [133a]. Also, it is believed that the absolute values of the intensities used in this analysis are accurate to ±10 percent.

The observed intensities for the night of January 6, 1972, are shown as a function of solar zenith angle in Figure 5. The ±10 percent error bars are those due to uncertainties in the calibration of the low brightness source. Errors in intensities calculated from the F-P observations were computed using the following equation from Reference 133:

$$\overline{\Delta I} = \left(\frac{I_0\alpha' + \beta' C}{N}\right)^{1/2}$$

where I_0 and C are defined in Section III. A. 1. a. (1), N is the number of data points in each line shape profile, and α' and β' are given in Figure 4 of Reference 133. In this study the errors ranged from a maximum of 6.9 R at the first observation when the integrated intensity was approximately 250 R to a minimum of 1.2 R at the last two observations when the integrated intensity was approximately 18 R. These are all within the ±10 percent errors due to the LBS calibration uncertainties. This night was selected for a detailed analysis because viewing conditions permitted observations during both the sunset and post-sunset twilight periods and the C-4 ionosonde was operational for the entire period. Additional observational data are shown in Appendix C. In general there is a very rapid decrease in intensity during the first hour after sunset followed by a much slower decrease during the second hour and then usually a gentle decrease for the remainder of the period. Occasional minor perturbations, on the order of a few Rayleighs, are seen in the histories; these may be due to either small scale perturbations in the electron densities or to wave-like motions that perturb the neutral atmosphere. Determinations of the exact causes of these perturbations will require a much more detailed analysis, which is not within the scope of this investigation. The absolute values of the observed intensities are much more variable from day to day. Once again, a more detailed analysis is required to establish the causes of these variations. However, in general, it seems that these larger variations are associated with the formulation of the Jacchia models of the neutral atmosphere in which both the molecular oxygen and nitrogen number densities increase with increasing exospheric temperature. This outward expansion of the neutral atmosphere during periods of increased solar activity causes an increase in the intensity of the 6300 Å emission with all other variables, especially the ionosphere, remaining constant.

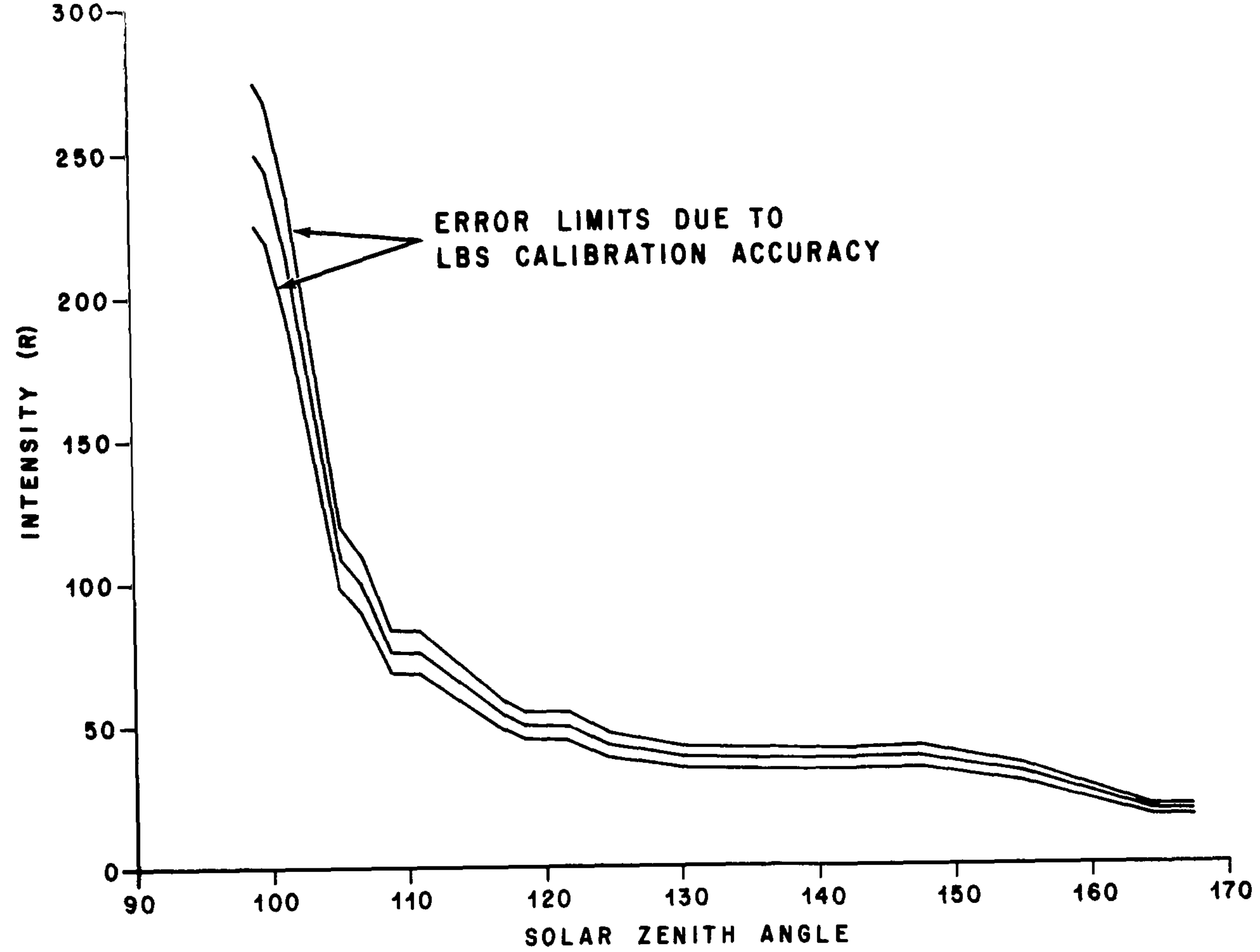

Figure 5. 6300 Å intensity as a function of solar zenith angle on January 6, 1972.

2. NEUTRAL TEMPERATURE MEASUREMENTS

The Doppler broadening of the 6300 Å emission line has been shown to be a good measure of the temperature of the neutral atmosphere. The procedure used to derive temperatures from the Fabry-Perot interferometer measurements has been discussed in detail by Hays and Roble [133]. Some typical Fabry-Perot interferometer fringes from the twilight period of January 6, 1972, are shown in Figures 6 through 13. The figures show intensity counts from the photomultiplier tube of the F-P system as a function of pressure in the etalon chamber, with the pressure being directly related to wavelength. These are, therefore, scans across the 6300 Å emission lines, and in theory the half-widths, line widths at half-heights, are proportional to the temperature of the emitting particles. In Figures 6 and 7, the rapidly decreasing intensity of the combined background and line are readily distinguishable. In the remaining figures the decrease in intensity appears to be almost negligible.

One of the assumptions in the data reduction technique discussed in References 123 and 133 is that the intensities of both the background and the emission line remain constant during the pressure (wavelength) scan. Since this is not the case for the first four or five fringes in the twilight period, the varying intensities had to be corrected before the data could be reduced. Both log and exponential curves were fit through the intensity counts from the F-P system during those portions of the pressure scans when only the background was being measured. The curve which fit the data best was then used to correct for the varying background intensity. Each fringe that showed a variable background was reconstructed by subtracting from each intensity data point the intensity value computed from the curve fit through the background intensity values only. Arbitrarily then, a value of 200 was added to each data point to preclude the possibility of obtaining negative intensity values. Figures 14 through 17 show the results of this reconstruction. These four figures correspond to Figures 6 through 9, respectively, i.e., the immediate post-sunset portion of the January 6, 1972, twilight period. In the immediate post-sunset period, the 6300 Å line is so intense that pressure scans can be accomplished in less than approximately 2 min; therefore, the varying intensity of the line itself during the scan period is so small that no additional correction is required.

These "raw" data were then reduced using a computerized version of the technique discussed in References 123 and 133. The derived temperatures are shown as a function of solar zenith angle in Figure 18.

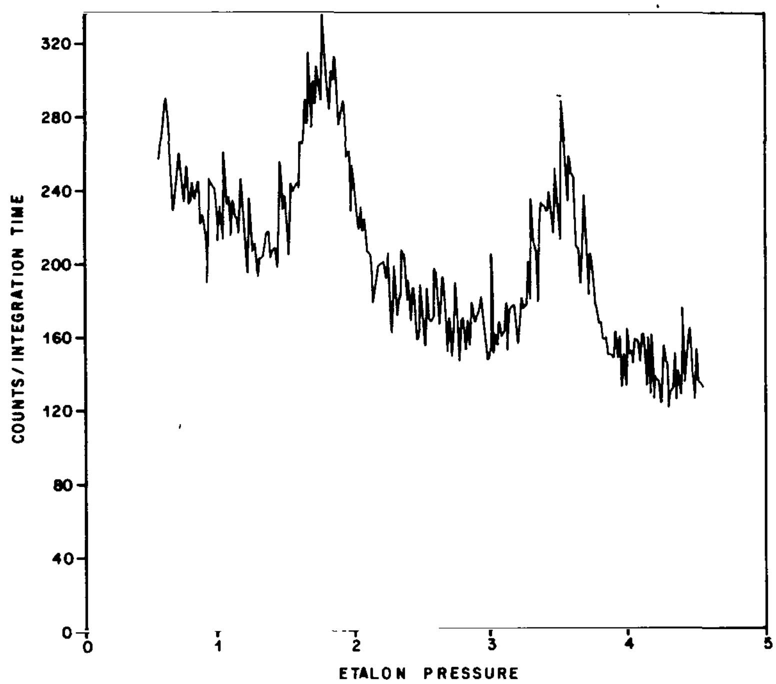

Figure 6. Fabry-Perot interferometer observations of the 6300 Å emission line shapes at 1728 and 1732 CST on January 6, 1972.

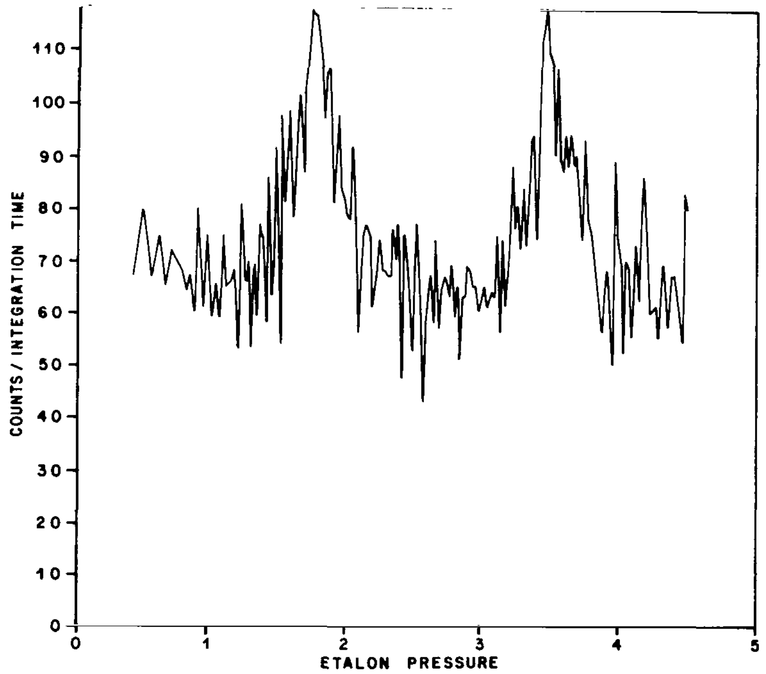

Figure 7. Fabry-Perot interferometer observations of the 6300 Å emission line shapes at 1740 and 1742 CST on January 6, 1972.

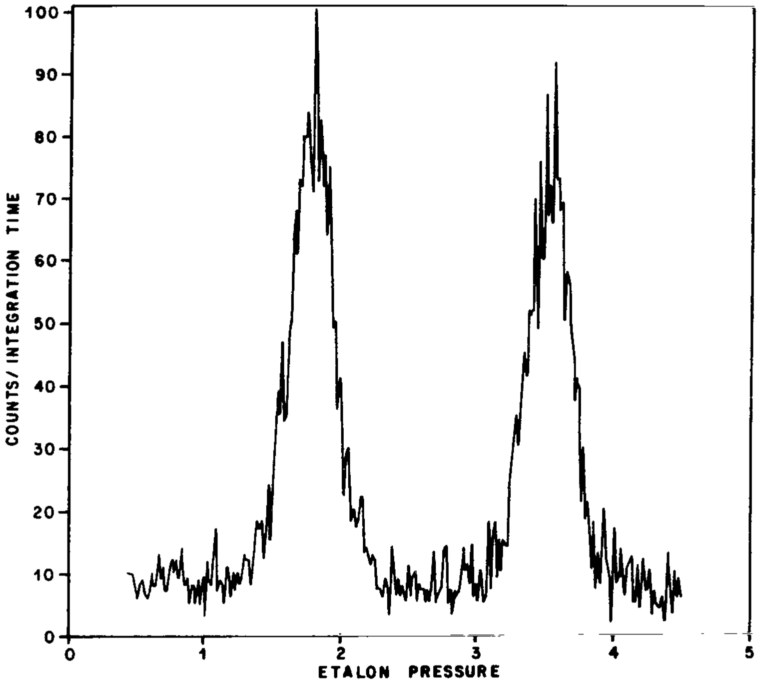

Figure 8. Fabry-Perot interferometer observations of the 6300 Å emission line shapes at 1751 and 1756 CST on January 6, 1972.

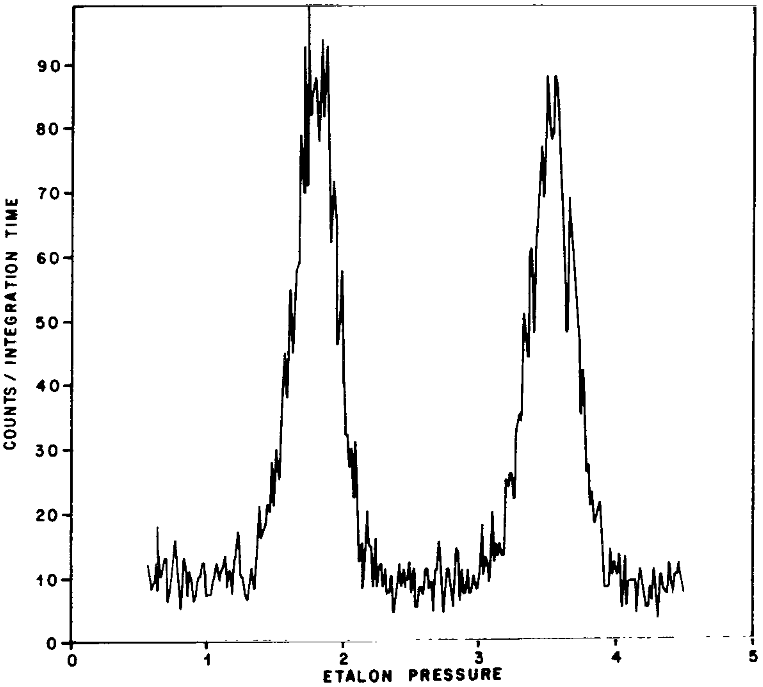

Figure 9. Fabry-Perot interferometer observations of the 6300 Å emission line shapes at 1805 and 1811 CST on January 6, 1972.

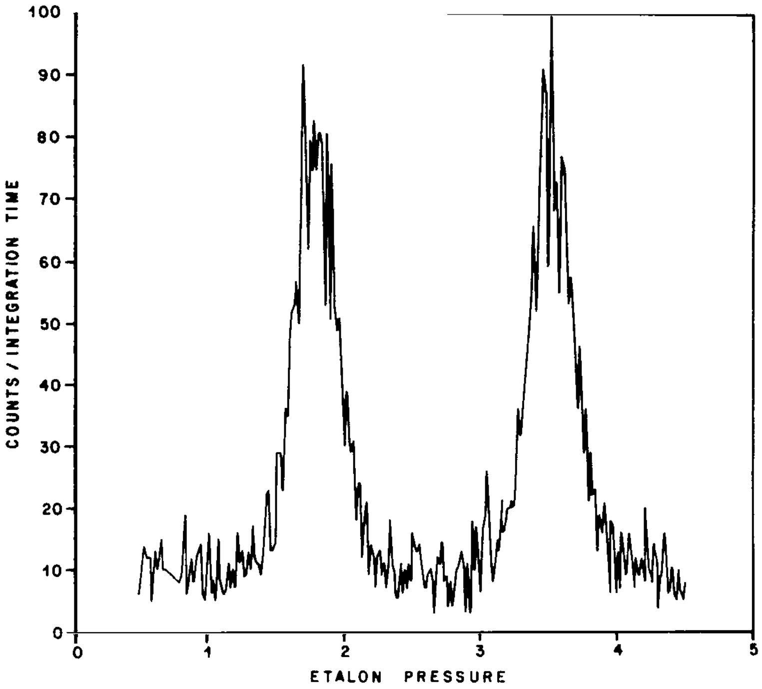

Figure 10. Fabry-Perot interferometer observations of the 6300 Å emission line shapes at 1822 and 1832 CST on January 6, 1972.

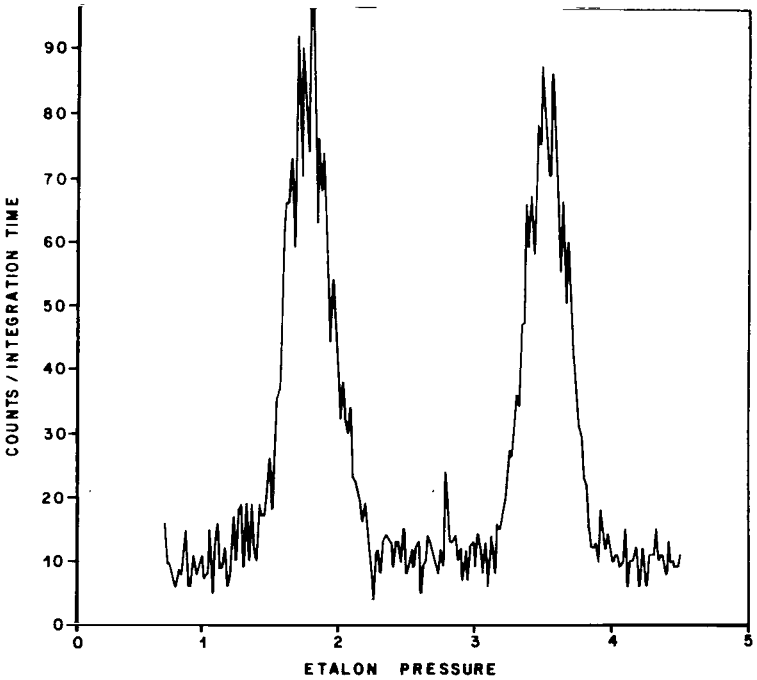

Figure 11. Fabry-Perot interferometer observations of the 6300 Å emission line shapes at 1845 and 1855 CST on January 6, 1972.

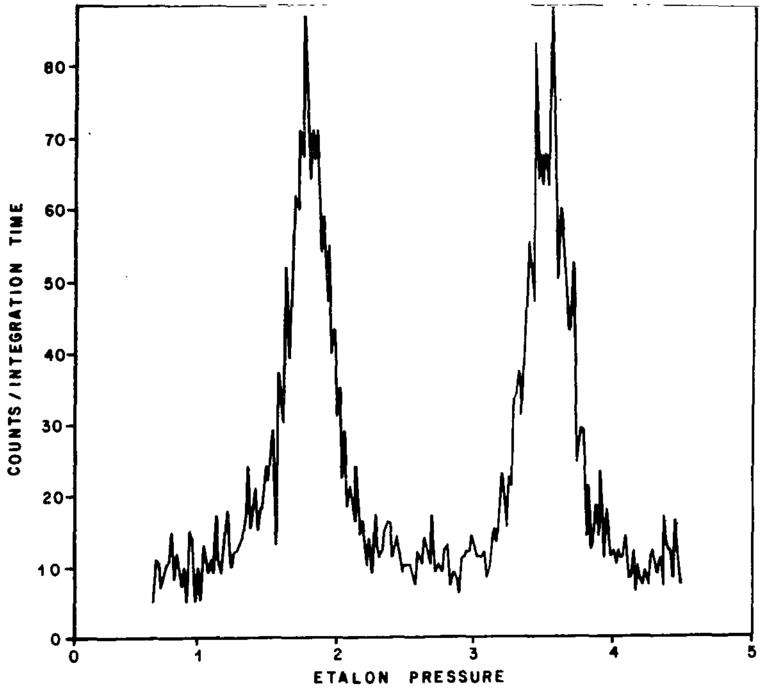

Figure 12. Fabry-Perot interferometer observations of the 6300 Å emission line shapes at 1903 and 1910 CST on January 6, 1972.

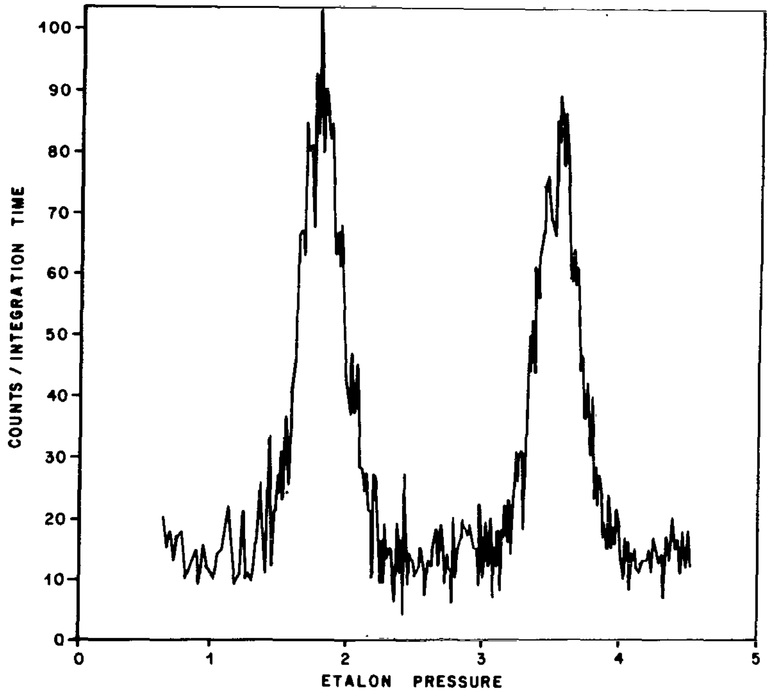

Figure 13. Fabry-Perot interferometer observations of the 6300 Å emission line shapes at 1926 and 1940 CST on January 6, 1972.

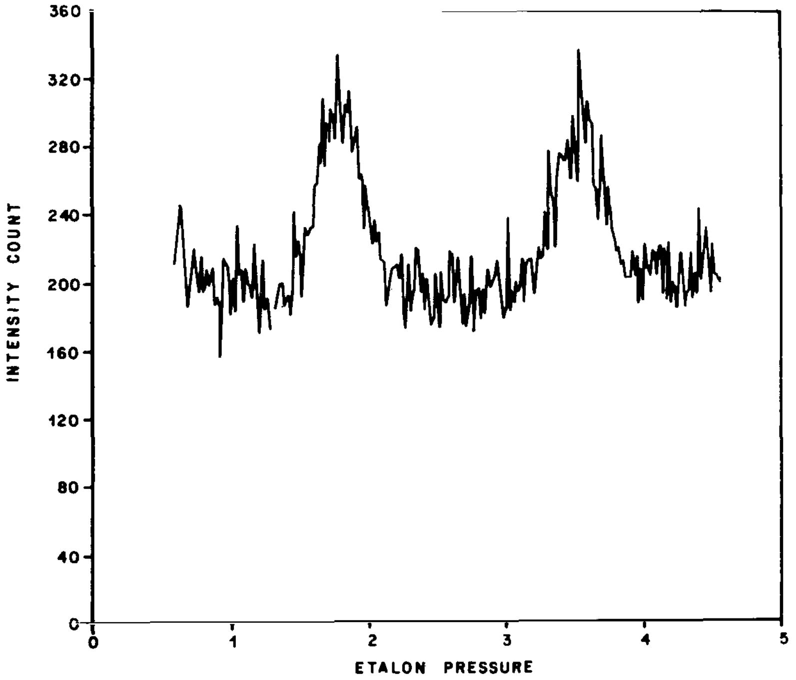

Figure 14. 6300 Å emission line shapes at 1728 and 1732 CST on January 6, 1972, after correcting for and removal of the variable intensity of the background.

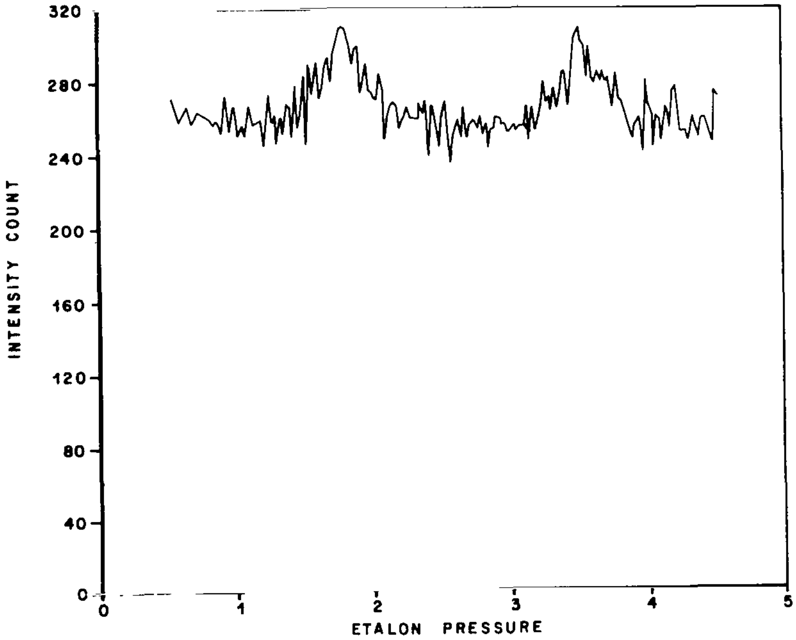

Figure 15. 6300 Å emission line shapes at 1740 and 1742 CST on January 6, 1972, after correcting for and removal of the variable intensity of the background.

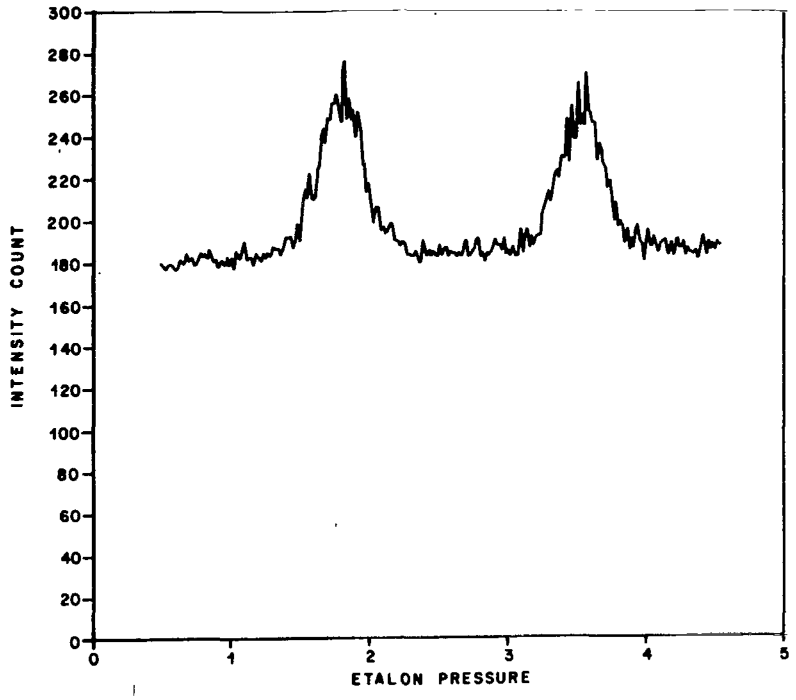

Figure 16. 6300 Å emission line shapes at 1751 and 1756 CST on January 6, 1972, after correcting for and removal of the variable intensity of the background.

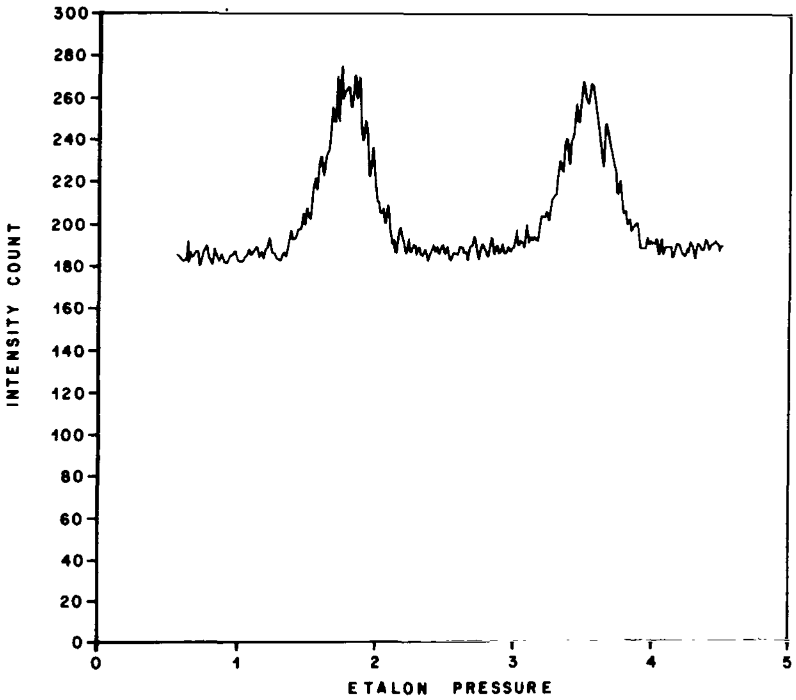

Figure 17. 6300 Å emission line shapes at 1805 and 1811 CST on January 6, 1972, after correcting for and removal of the variable intensity of the background.

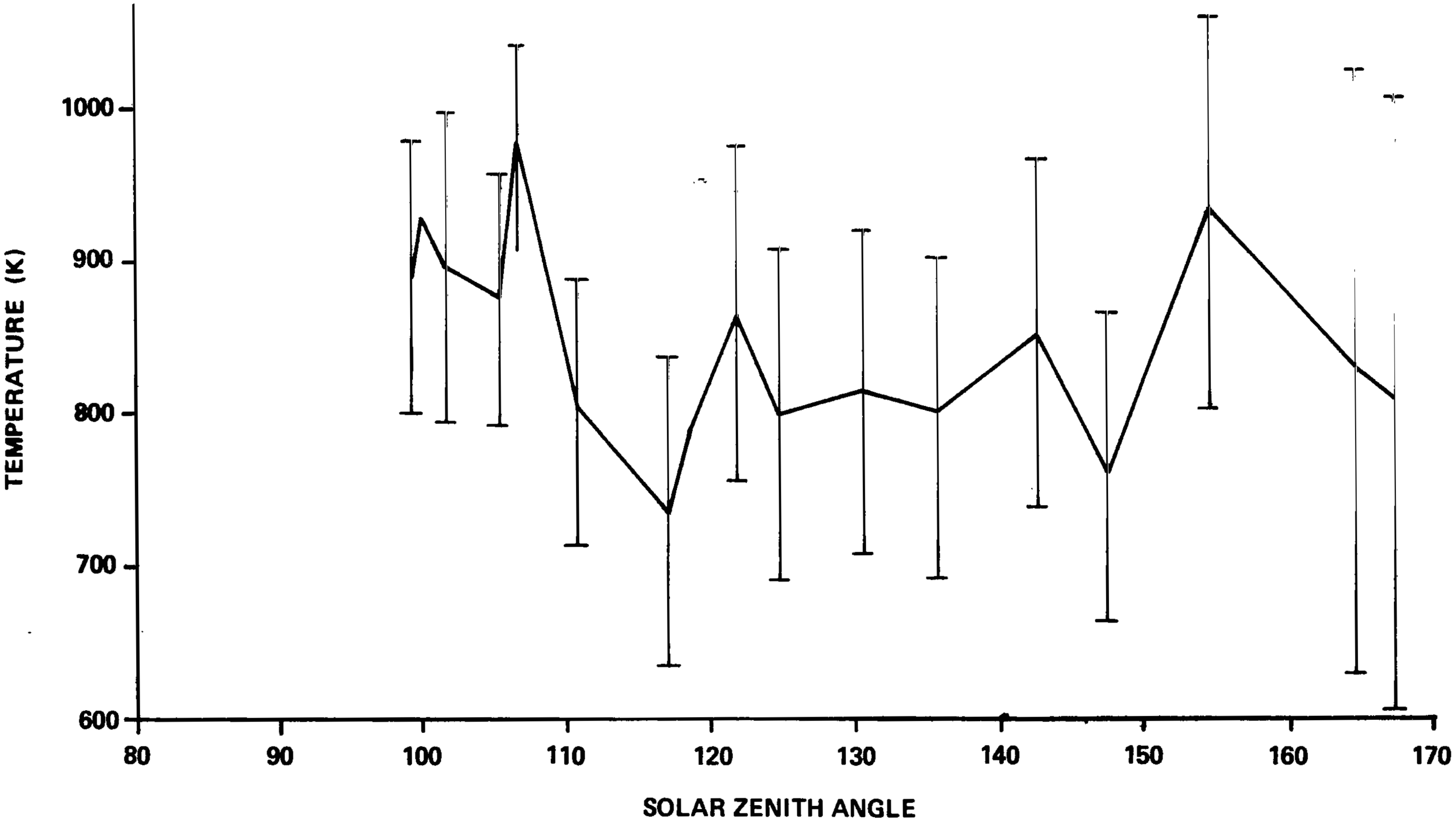

Figure 18. Thermospheric temperatures derived from the Fabry-Perot interferometer observed 6300 Å emission line shapes as a function of solar zenith angle on January 6, 1972.

The error bars shown on the figure were calculated from the following equation from Reference 133:

$$\Delta T = \left(\frac{\alpha}{NI_0} + \frac{\beta}{NI_0^2}\right)^{1/2}$$

where I_0 and C are defined in Section III. A. 1. a. (1), N is the number of data points in the line shape profile, and α and β are given in Figure 3 of Reference 133.

3. ELECTRON DENSITY MEASUREMENTS

The electron density-height profiles used in this theoretical analysis were obtained from C-4 ionosonde measurements. True height analysis was accomplished using a computer program based on the technique proposed by Doupnik and Schmerling [137]. The electron density-true height profiles above the F_2 peak were computed using a constant scale height two times that of the atomic oxygen scale height at the F_2 peak with a kinetic temperature of 1500 K.

Figure 19 is a plot of contours of constant electron density versus solar zenith angle for the approximate 7 h period following sunset. Both the height of the F_2 peak and the maximum electron density decrease relatively smoothly with time, and no large scale motions of the charged particles are apparent in this record.

During the course of this investigation much effort was spent in establishing the electron density-true height profiles. Several different reduction techniques were compared using known electron density-true height profiles as input data. Various starting techniques, amounts of input data, location of input data, and types of input data (X-ray only, O-ray only, X- and O-ray data) were used in the available data reduction programs to determine which output results most closely matched the known profiles. The electron density-true height profiles referenced above are believed to be most representative of the ionospheric conditions existing over Huntsville, Alabama, on the night of January 6, 1972. They were determined by using the combination of starting point, amount, type, and location of input data established during the study as the one combination that produced output results which most nearly matched the known electron density-true height profiles. Although these results are satisfactory insofar as this analysis is concerned, this area requires a concerted

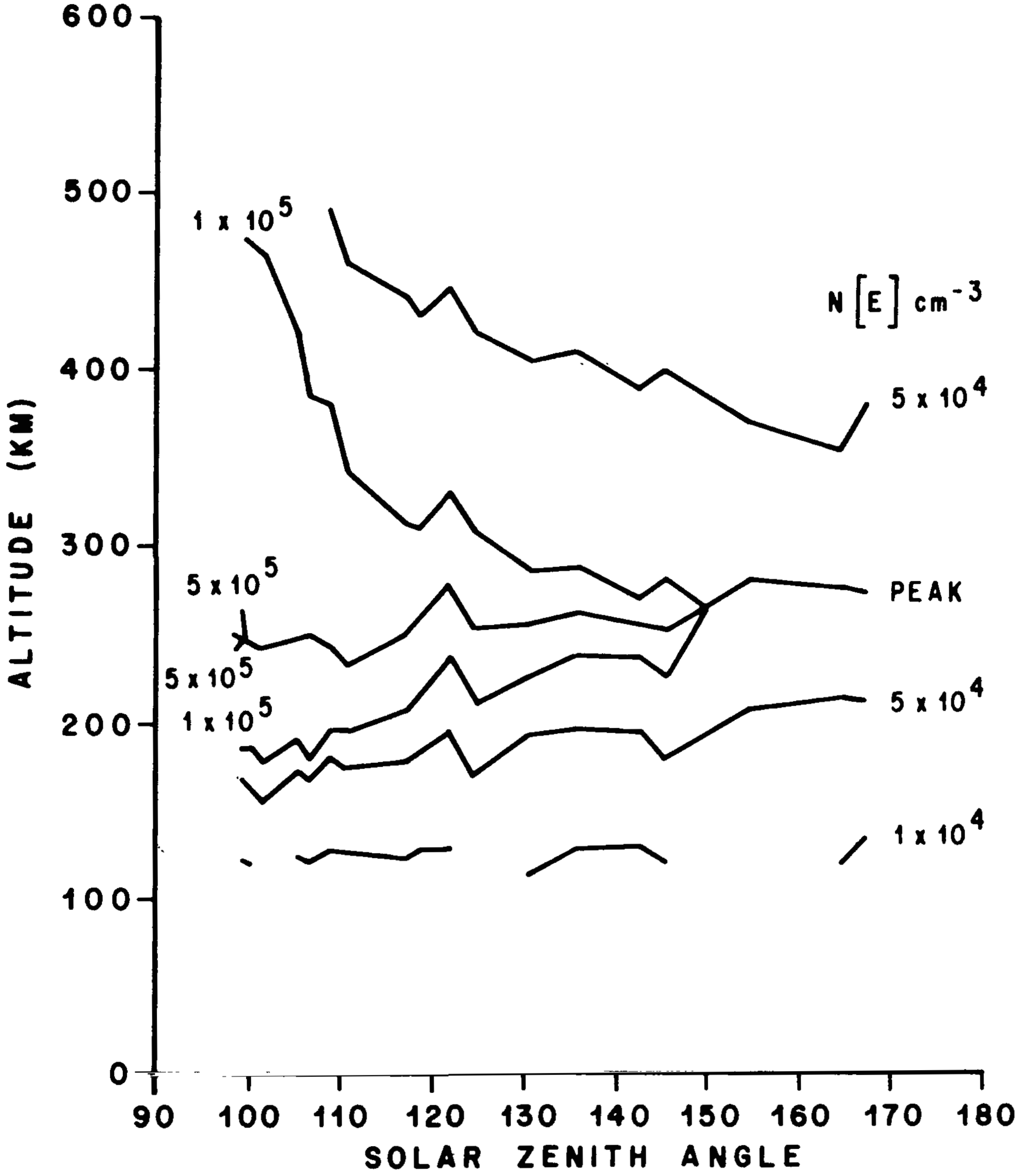

Figure 19. Contours of constant electron number density.

research effort. Until such time as this additional research is concluded, electron density-true height profiles, other than possibly those reduced by the group at NOAA, Boulder, Colorado, should not be used without additional verification.

IV. NEUTRAL ATMOSPHERE

A. Models

Three models of the neutral upper atmosphere of the Earth were used in this analysis. The original Jacchia 1964 model and the same model with the 120 km boundary conditions recommended by Reber[2] both used the analytical representation of the neutral gas temperature-height profile developed by Bates [3] and modified by Walker [138] to calculate constituent number density-height profiles. The third model used was the Jacchia 1971 model which was used in its original form. Table 12 contains the boundary condition values used as inputs to the Jacchia 1964 model atmosphere. Corresponding number densities at 120 km altitude for the constituents in the Jacchia 1971 model atmosphere are variable and dependent upon the exospheric temperature. Differences in the computed 6300 Å emission integrated intensities and volume emission profiles only from the differences inherent in these models are discussed in detail in Section VII.

TABLE 12. NEUTRAL CONSTITUENT NUMBER DENSITIES AT 120 km

N_2	O_2	O	Source
3.7131×10^{11} cm^{-3}	6.0645×10^{10} cm^{-3}	9.4607×10^{10} cm^{-3}	Reber [2]
4.0×10^{11} cm^{-3}	7.5×10^{10} cm^{-3}	7.6×10^{10} cm^{-3}	Jacchia [1]

B. Columnar Number Densities

The production of ^1D oxygen atoms and the subsequent emission of the 6300 Å photons are dependent upon the number densities of the neutral constituents as well as their total densities in a unit column between the altitude of the emitting atoms and the source of the agent causing the excitation, the Sun in the case of dissociative photoexcitation and the magnetic conjugate point in the case of photoelectrons.

---

[2] Private communication, 1973.

To calculate the total columnar number densities for use in the dissociative photoexcitation calculations, information is required on the constituent number density variation with height in the atmosphere. All major atmospheric constituents are believed to be in diffusive equilibrium above approximately 120 km altitude; therefore, at any altitude, z, above 120 km the constituent number density, $n_i(z)$, can be calculated from

$$n_i(z) = n_i(z_0) \frac{T(z_0)}{T(z)} \exp - \int_{z_0}^{z} \frac{dz}{H_i(z)} , \tag{18}$$

where z_0 is a reference height in the diffusive equilibrium region of the atmosphere, taken as 120 km in this study; T is the kinetic temperature; and $H_i(z)$, the scale height of the ith constituent at altitude, z, is defined as

$$H_i(z) \equiv RT(z)/M_i g(z) , \tag{19}$$

where R is the universal gas constant, M_i is the molecular mass of the ith constituent, and g(z), the acceleration due to gravity at the height z in kilometers, is defined as

$$g(z) = 9.80665 \times 10^{-3} \left(\frac{6356.77}{6356.77 + z} \right)^2 . \tag{20}$$

From the perfect gas law and the hydrostatic equation, the total number density in a unit vertical column above a height, z, in an isothermal atmosphere is

$$N_i(z) = n_i(z)\, H_i(z) . \tag{21}$$

For nonvertical incidence during twilight observations, the zenith angle of the Sun must be known. For geographic latitude, θ, local time (angle from noon), Ψ, and solar declination, δ, the zenith angle, χ, is obtained from

$$\cos\chi = \cos\theta \cos\delta \cos\Psi + \sin\theta \sin\delta \quad . \tag{22}$$

During the twilight period studied here, the zenith angle ranged from 97.5° to 166°. When the zenith angle, χ, is 60° or less, the curvature of the atmosphere may be neglected and the constituent total columnar number density above an altitude, z, is approximated by

$$N_i(z) \simeq n_i(z)\, H_i(z) \sec\chi \quad . \tag{23}$$

However, this is not the case during the twilight period and the curvature of the atmosphere must be included in the calculations. Chapman [139, 140] first investigated the problem of calculating total columnar number densities in a slant path through a spherical isothermal atmosphere. In an isothermal atmosphere the scale height, H_i, for a given constituent is constant and independent of height. If the constituent is in hydrostatic equilibrium, the total columnar number density above an altitude z, can be calculated from

$$N_i(z) = n_i(z)\, H_i(z) \left\{ x(I) \sin\chi \int_0^{\chi} \csc^2\lambda \exp\left[x(I)\left(1 - \frac{\sin\chi}{\sin\lambda}\right)\right] d\lambda \right\} \quad , \tag{24}$$

where $x(I) = (R_E + z)/H_i(z)$ and R_E is the Earth's radius. The Chapman function, generally denoted as $Ch(x, \chi)$, is the quantity between the braces. It was developed on the assumption of an isothermal atmosphere, a situation which exists only above about 250 km in the Earth's atmosphere. Since the height profile of the constituent number density, $n_i(z)$, is almost exponential, the major contribution to the total column density comes from a narrow altitude range near z over which the temperature is nearly constant. The total column density is relatively insensitive to the temperature-height profile; therefore, the constituent scale height at the observational altitude can be used in the Chapman function. A number of approximations to the Chapman function have been developed; however, the one used in this study was introduced by Rishbeth and Garriott [141]:

$$Ch(x,\chi) = [\pi/2\, x(I)\, \sin\chi]^{1/2} \exp\left[\frac{x(I)}{2} \cos^2\chi\right] \left\{1 \pm \mathrm{erf}\left[\frac{x(I)}{2} \cos^2\chi\right]^{1/2}\right\} , \tag{25}$$

where the symbols are as previously defined and the plus sign is used for zenith angles $\geq 90°$ while the minus sign applies to zenith angles $< 90°$.

C. Exospheric Temperatures

The exospheric temperatures required to establish the constituent number density height profiles in the atmospheric models used in the analysis were derived from the analysis of the Doppler broadened emission line profiles measured with the Fabry-Perot interferometer after the varying background correction had been made.

V. THEORETICAL APPROACH

The theoretical model established to study the 6300 Å emission intensities during the twilight period contains two production sources of ^1D oxygen atoms.

A. Photodissociation

The number of ^1D oxygen atoms produced at each altitude level by solar photons in the principal Schumann-Runge continuum was calculated by

$$n\left[O(^1D)\right]_z = \sum_{\lambda=1125}^{1775} \sigma(\lambda,O_2) \times FLUX(\lambda)_z \times n(O_2)_z \quad , \tag{26}$$

where $\sigma(\lambda,O_2)$ is the molecular oxygen absorption cross section for radiation of wavelength λ, and $FLUX(\lambda)_z$ is the photon flux of wavelength λ at height z. The photon flux of wavelength λ at each altitude z was calculated from

$$\mathrm{FLUX}(\lambda)_z = \mathrm{FLUX}(\lambda)_\infty \times \mathrm{EXP}\left\{\sum_I \left[-N(I)_z \times \sigma(\lambda, I) \right]\right\} \quad , \qquad (27)$$

where $\mathrm{FLUX}(\lambda)_\infty$ is the flux of solar photons of wavelength λ at the top of the atmosphere, 500 km in this study; $N(I)_z$ is the column density of the constituent I above level z; and $\sigma(\lambda, I)$ is the absorption cross section of the constituent I for photons of wavelength λ. The column density of the constituent I is calculated from

$$N(I)_z = n(I)_z \times H(I)_z \times CH(I)_z \quad , \qquad (28)$$

where $n(I)_z$ is the number density of the constituent I at altitude z; $H(I)_z$ is its scale height at altitude z computed from

$$H(I)_z = \frac{RT_z}{M(I) g_z} \quad , \qquad (29)$$

and $CH(I)_z$, the Chapman function for constituent I which is used to correct for the atmosphere at the large zenith angles during the twilight period, is calculated from equation (25). Each photodissociation was assumed to produce one ^1D oxygen atom.

B. Dissociative Recombination

Dissociative recombination of both O_2^+ and NO^+ with thermal electrons, as discussed in Section II, where both of these ions are produced as a result of collisions between atomic oxygen ions and oxygen and nitrogen molecules [equations (9) and (10)] was included in the computations. Since the atomic oxygen ion density-height profiles required for the calculations were not available, the O^+ number density at each altitude, z, was computed from

$$n[O^+]_z = \frac{0.95 \times [n(E)_z]^2}{n(E)_z + \frac{\gamma_1 n(N_2)_z}{\alpha_1} + \frac{\gamma_2}{\alpha_2} \times n(O_2)_z} \tag{30}$$

in a manner similar to that of Wickwar [142], where $n(E)_z$ is the electron number density at altitude z, $n(N_2)_z$ and $n(O_2)_z$ are the molecular nitrogen and oxygen number densities at altitude z, and the Greek symbols are the rate coefficients for the following reactions:

$$O^+ + N_2 \rightarrow NO^+ + N \qquad : \gamma_1 \tag{31}$$

$$NO^+ + e \rightarrow N + O(^1D) \qquad : \alpha_1 \tag{32}$$

$$O^+ + O_2 \rightarrow O_2^+ + O \qquad : \gamma_2 \tag{33}$$

$$O_2^+ + e \rightarrow O + O^* \qquad : \alpha_2 \quad . \tag{34}$$

In this formulation O^+ is assumed to be in a steady-state chemical equilibrium and it can never exceed 95 percent of the electron density, even at and above the F_2 peak. Neither of these assumptions is critical to the calculated production of 6300 Å emission intensity.

The number of ^1D oxygen atoms at altitude z from this production mechanism is calculated by

$$n[O(^1D)]_z = n[O^+]_z \left[n(O_2)_z \times \gamma_2 \, EFF1 + n(N_2)_z \times \gamma_1 \, EFF2 \right] \quad , \tag{35}$$

where EFF1 and EFF2 are the efficiencies of these reactions for producing ^1D oxygen atoms.

The number density of $O(^1D)$s at altitude z is the total of these two production mechanisms.

C. Volume Emission Rate

The volume emission rate at altitude z is computed from

$$E_{6300} = \frac{6.9 \times 10^{-3} \times n[O(^1D)]_z}{9.1 \times 10^{-3} + q_1 \times n(N_2)_z + q_2 \times n(O_2)_z} \; (\text{photons cm}^{-3}\ \text{s}^{-1}) \quad , \tag{36}$$

where q_1 and q_2 are the rate coefficients for quenching by molecular nitrogen and oxygen, respectively.

D. Integrated Emission Intensity

Integrated emission intensity is calculated by using a trapezoidal integration technique.

VI. SOLAR FLUXES AND ABSORPTION CROSS SECTIONS

Two separate sets of solar flux values in the Schumann-Runge continuum with associated O_2 absorption cross sections were used in this study. Table 13 contains solar flux values from Friedman and Tousey of the Naval Research Laboratory as reported by Hinteregger, Hall, and Schmidtke [6]. The cross sections contained in this same table are from Metzger and Cook [7]. Table 14 contains solar fluxes and absorption cross sections recommended by Ackerman [5].

VII. DISCUSSION

On the night of January 6, 1972, conjugate point sundown occurred at approximately 2233 CST, assuming a screening height of 180 km; therefore, the airglow over the observation point (Huntsville, Ala.) after this time could only be the result of dissociative recombination of the molecular ions, O_2^+ and NO^+. On this night only the observations at 2303 and 2330 CST occurred after 2233 CST.

TABLE 13. SCHUMANN-RUNGE CONTINUUM SOLAR FLUXES OF FRIEDMAN AND TOUSEY WITH ASSOCIATED O_2 ABSORPTION CROSS SECTIONS FROM METZGER AND COOK [6,7]

Wave Length (Å)	Solar Fluxes ($cm^{-2}\ s^{-1}$)	Cross Sections (cm^2)
1775 - 1725	1.06×10^{12}	1.70×10^{-19}
1725 - 1675	7.00×10^{11}	8.60×10^{-19}
1675 - 1625	4.20×10^{11}	2.20×10^{-18}
1625 - 1575	2.60×10^{11}	5.20×10^{-18}
1575 - 1525	1.33×10^{11}	8.00×10^{-18}
1525 - 1475	7.30×10^{10}	1.13×10^{-17}
1475 - 1425	3.70×10^{10}	1.43×10^{-17}
1425 - 1375	1.83×10^{10}	1.43×10^{-17}
1375 - 1325	1.77×10^{10}	5.80×10^{-18}

Airglow intensities for these two times were calculated using the set of equations discussed in detail in Section V with all three atmospheric models discussed in Section IV and the electron density-height profiles discussed in Section III. The neutral atmospheric constituent distributions are established by the derived exospheric temperatures. Once these components are established, the only inputs to the set of equations that affect the calculated intensities are the rate coefficients for equations (31) through (34), the efficiencies of the $O(^1D)$ production mechanisms in equation (35), and the quenching coefficients in equation (36).

TABLE 14. SCHUMANN-RUNGE CONTINUUM SOLAR FLUXES AND ASSOCIATED O_2 ABSORPTION CROSS SECTIONS RECOMMENDED BY ACKERMAN [5]

ΔA (Å)	q (cm^{-2} s^{-1})	$\sigma(O_2)$ (cm^2)
Lyα 1.215,67	3.00×10^{11}	1.00×10^{-20}
1.170 - 1.163	1.03×10^{8}	2.00×10^{-20}
1.176 - 1.170	2.66	1.25×10^{-18}
1.183 - 1.176	1.12	2.55×10^{-19}
1.190 - 1.183	1.24	3.00×10^{-20}
1.198 - 1.190	1.82	3.75×10^{-19}
1.205 - 1.198	1.90	4.45×10^{-18}
1.212 - 1.205	7.40	8.35
1.220 - 1.212	2.28×10^{9}	6.00×10^{-19}
1.227 - 1.220	3.67	2.35
1.235 - 1.227	1.36	4.50
1.242 - 1.235	1.61	3.35
1.250 - 1.242	1.32	1.75×10^{-17}
1.258 - 1.250	1.41	8.95×10^{-19}
1.266 - 1.258	3.11	4.30
1.274 - 1.266	1.06	1.10
1.282 - 1.274	1.37	2.05
1.290 - 1.282	1,02	4.43
1.299 - 1.290	1.14	5.55
1.307 - 1.299	7.29	4.20
1.316 - 1.307	2.20	6.85
1.324 - 1.316	1.59	1.45×10^{-18}
1.333 - 1.324	2.21	2.25
1.342 - 1.333	1.24×10^{10}	2.30×10^{-18}
1.351 - 1.342	1.99×10^{9}	4.55
1.360 - 1.351	3.09	7.23
1.370 - 1.360	2.57	9.50

TABLE 14. (Concluded)

ΔA (Å)	q ($cm^{-2} s^{-1}$)	$\sigma(O_2)$ (cm^2)
1.379 - 1.370	2.74	1.23×10^{-17}
1.389 - 1.397	3.10	1.32
1.408 - 1.389	7.60	1.36
1.428 - 1.408	1.01×10^{10}	1.40
1.449 - 1.428	1.30	1.48
1.470 - 1.449	1.82	1.41
1.492 - 1.470	2.33	1.29
1.515 - 1.492	2.66	1.15
1.538 - 1.515	2.90	9.91×10^{-18}
1.562 - 1.538	3.60	8.24
1.587 - 1.562	4.75	6.58
1.613 - 1.587	6.40	4.97
1.639 - 1.613	5.49	3.45
1.667 - 1.639	1.19×10^{11}	3.08
1.695 - 1.667	1.76	1.23
1.724 - 1.695	2.32	7.22×10^{-19}
1.739 - 1.724	1.44	4.58
1.754 - 1.739	1.83	2.74

A. Reaction and Quenching Rate Coefficients

It was assumed that the results of Dalgarno and Walker [11] were correct and that no $O(^1D)$ atoms were formed from the dissociative recombination of NO^+. Since quenching of $O(^1D)$ atoms by O_2 is insignificant in comparison with quenching by N_2 and its reaction rate coefficient appears to be reliably known (Table 7), the value of 5×10^{-11} cm^3 s^{-1} was used throughout the calculations. With the exception of the N_2 quenching coefficient and the efficiency of the $O_2^+ + e$ production mechanism, the remaining rate coefficients also appear to be reliably known; therefore, the following values were used throughout the calculations:

$$NO^+ + e \xrightarrow{\alpha_1} N + O \qquad \alpha_1 = 4.1 \times 10^{-7}\ (300/T)\ \mathrm{cm^3\ s^{-1}}$$

$$O_2^+ + e \xrightarrow{\alpha_2} O + O \qquad \alpha_2 = 1.95 \times 10^{-7}\ (300/T)^{0.7}\ \mathrm{cm^3\ s^{-1}}$$

$$O^+ + O_2 \xrightarrow{\gamma_2} O_2^+ + O \qquad \gamma_2 = 2 \times 10^{-11}\ \mathrm{cm^3\ s^{-1}}$$

$$O^+ + N_2 \xrightarrow{\gamma_1} NO^+ + N \qquad \gamma_1 = 1 \times 10^{-12}\ \mathrm{cm^3\ s^{-1}}$$

$$O(^1D) + O_2 \xrightarrow{q_2} O_2 + O \qquad q_2 = 5 \times 10^{-11}\ \mathrm{cm^3\ s^{-1}}$$

With these input parameters fixed, there are only two parameters that can be varied to obtain agreement between the calculated and observed intensities at 2303 and 2330 CST. These are the N_2 quenching coefficient and the efficiency of the $O_2^+ + e$ production mechanism. All possible combinations of these two rate coefficients were used with all three model atmospheres. In all of the succeeding figures the solid line connects the observed intensity values while the broken line connects the calculated intensity values. Figures 20 through 22 show results using the Jacchia 1964 model atmosphere.

In Figure 20 the molecular nitrogen quenching coefficient is 1×10^{-10} $\mathrm{cm^3\ s^{-1}}$ and the $O_2^+ + e$ production mechanism efficiency is 1.00, which means that one $O(^1D)$ atom is formed from every dissociative recombination. These are maximum values for both of these parameters, as reported in the literature. The calculated intensities at both 2303 and 2330 CST are approximately three times the observed intensities. Calculated intensities during the remainder of the period being studied are substantially larger than the observed intensities.

In Figure 21 the quenching coefficient remains as 1×10^{-10} $\mathrm{cm^3\ s^{-1}}$ while the dissociative recombination production efficiency is decreased to 0.50, which means that only one $O(^1D)$ atom is formed from every two recombinations. The calculated intensities at 2303 and 2330 CST are still almost 50 percent larger than the observed intensities. A similar decrease is evident in the calculated intensities during the remainder of the period being analyzed, although they are still larger than the observed intensities.

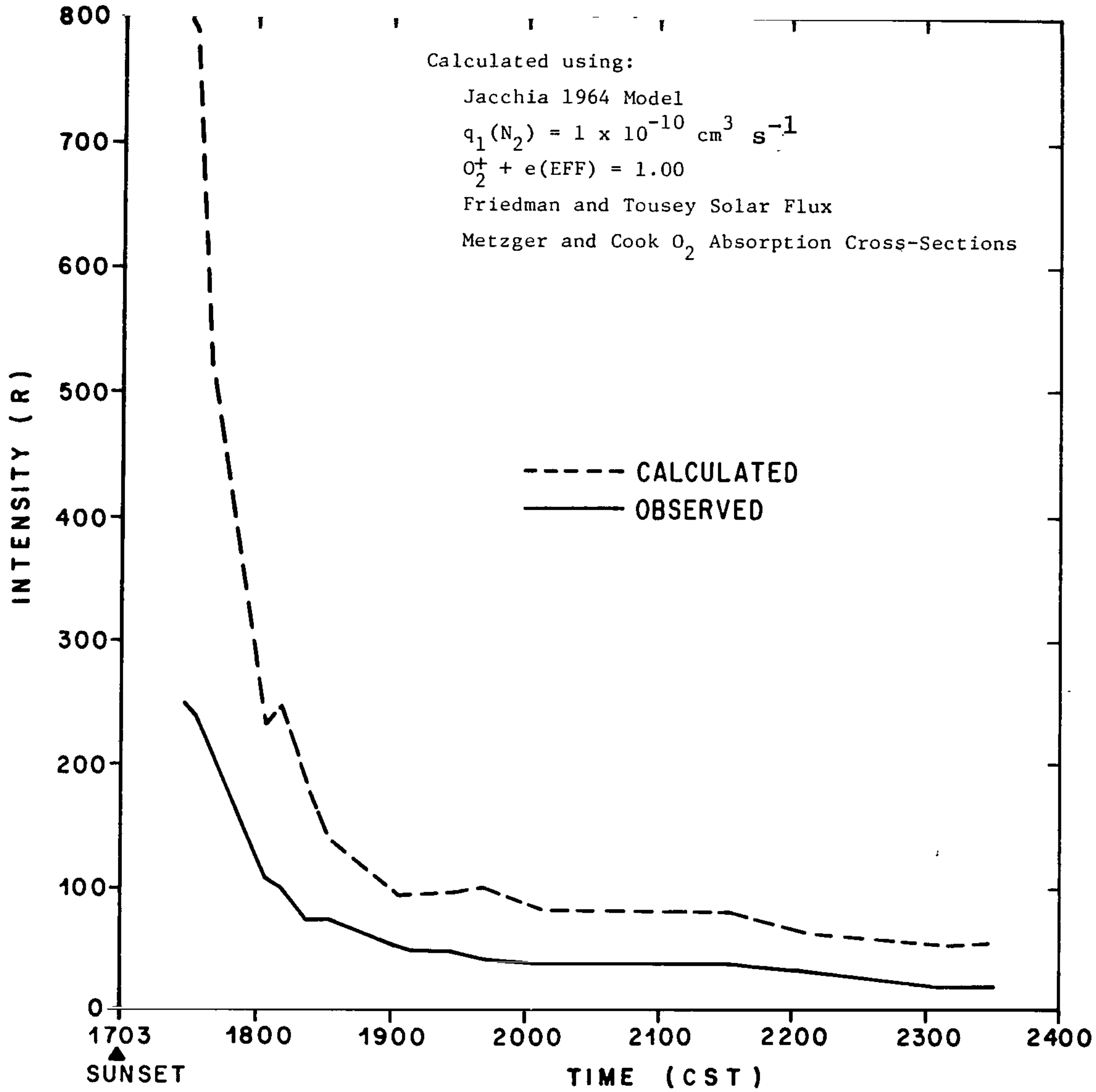

Figure 20. 6300 Å emission line intensities derived from Fabry-Perot interferometer observations and theoretically calculated intensities as a function of time after sunset on January 6, 1972.

In Figure 22 the quenching coefficient value remains at 1×10^{-10} cm^3 s^{-1} while the efficiency of the dissociative recombination production mechanism is decreased to 0.333, which means that only one O(^{1}D) atom is produced from every three recombinations. Agreement is excellent between calculated and observed intensities at both 2303 and 2330 CST. Once again, as expected,

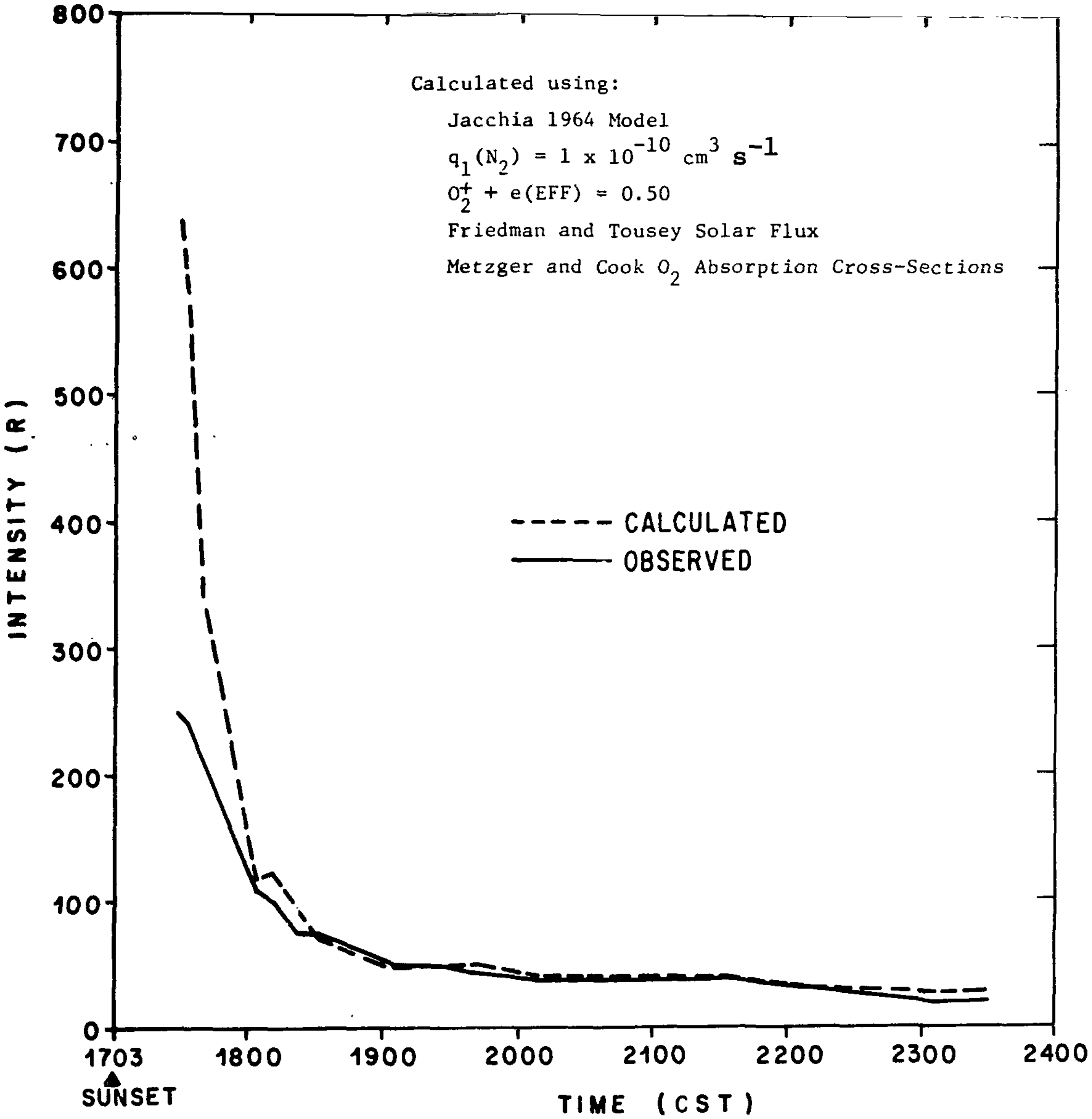

Figure 21. 6300 Å emission line intensities derived from Fabry-Perot interferometer observations and theoretically calculated intensities as a function of time after sunset on January 6, 1972.

agreement has improved between calculated and observed intensities during the remainder of the period. For the Jacchia 1964 model atmosphere, then, the best combination of parameters is a quenching coefficient of 1 × 10^{-10} cm^3 s^{-1} and a dissociative recombination efficiency of 0.333. This result tends to reinforce the assumption that the NO^+ + e mechanism does not produce any

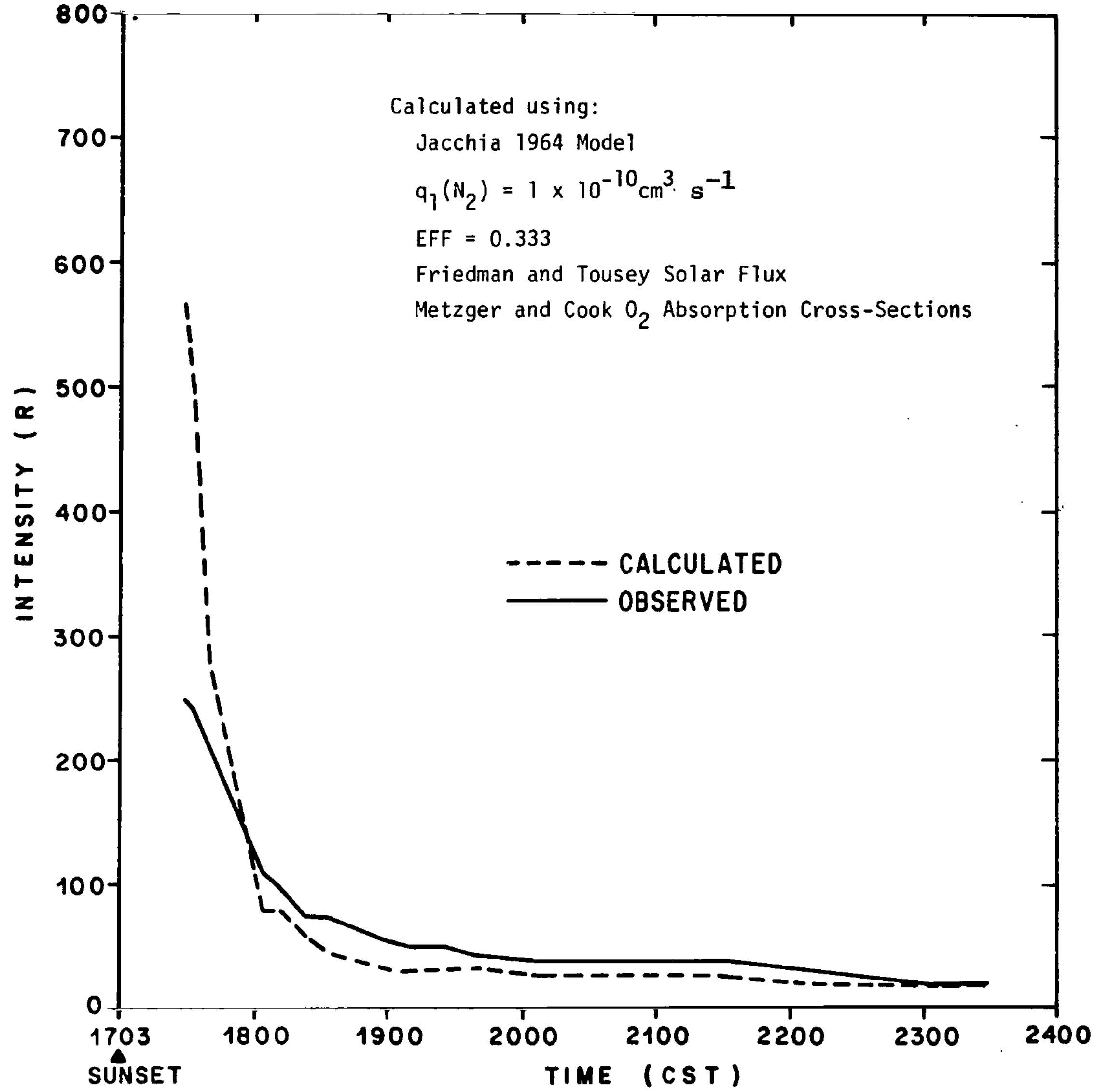

Figure 22. 6300 Å emission line intensities derived from Fabry-Perot interferometer observations and theoretically calculated intensities as a function of time after sunset on January 6, 1972.

$O(^1D)$ atoms, since any additional $O(^1D)$ atoms would require either a quenching coefficient larger than the value used, which is the maximum found in the literature, or an O_2^+ + e production efficiency of less than 0.333. This, however, contradicts the results of Wickwar [142] who found that a value of 0.50 provided the best results. A larger quenching coefficient would not agree with the results obtained by Hernandez [113] from the Ionospheric Modification Experiment which yielded a value of $9\begin{pmatrix}+1.0\\-0.5\end{pmatrix} \times 10^{-10}$ cm^3 s^{-1} based on a Jacchia 1964 model atmosphere formulation using an N_2 number density boundary value of 2.0×10^{11} cm^{-3} instead of the 4.0×10^{11} cm^{-3} values used herein.

Figures 23 and 24 show results using the Jacchia 1971 model atmosphere. In Figure 23 the quenching coefficient is 5×10^{-11} cm^3 s^{-1}, and the dissociative recombination production efficiency is 0.50. The calculated intensities at both 2303 and 2330 CST are approximately 60 percent larger than the observed emission intensities. Calculated intensities are greater than the observed intensities throughout the observation period. In Figure 24 the quenching coefficient is increased to 1×10^{-10} cm^3 s^{-1}. Agreement between calculated and observed intensities at both 2303 and 2330 CST is perfect. Calculated intensities are greater than observed intensities during that portion of the period when sunlight contributes to the emission intensity, prior to approximately 1805 CST, and less than observed intensities from approximately 1805 to 2303 CST. Any other combination of values of these parameters would result in the use of either a value of the quenching coefficient larger than the maximum value quoted in the literature or a value of the dissociative recombination production mechanism efficiency of less than 0.50, the value currently quoted in the literature as being most acceptable.

Figures 25 through 27 show the results of these combinations using the 120 km boundary conditions recommended by Reber[3] with the Jacchia 1964 model formulation and a constant temperature shape parameter of 0.01875, also recommended by Reber. These values were established by Reber in conjunction with his efforts to establish a new U.S. Standard Atmosphere; however, the resulting number density-height profiles he established are significantly different from those calculated herein because he used vertical flux and molecular diffusion terms that effectively changed the models from static to pseudo-dynamic. These fictitious flux terms, which were used to ensure compatibility between the model and observational data, increased the molecular nitrogen number densities while decreasing the molecular oxygen number densities at all altitudes. Both of these modifications would result in a decrease in the calculated intensity of the emission line.

In Figure 25 the quenching coefficient is 5×10^{-11} cm^3 s^{-1}, while the dissociative recombination production mechanism efficiency is 0.50. Calculated intensities are almost 80 percent larger than the intensities observed at both 2303 and 2330 CST. Calculated intensities are larger than the observed intensity value throughout the period.

---

[3] Ibid.

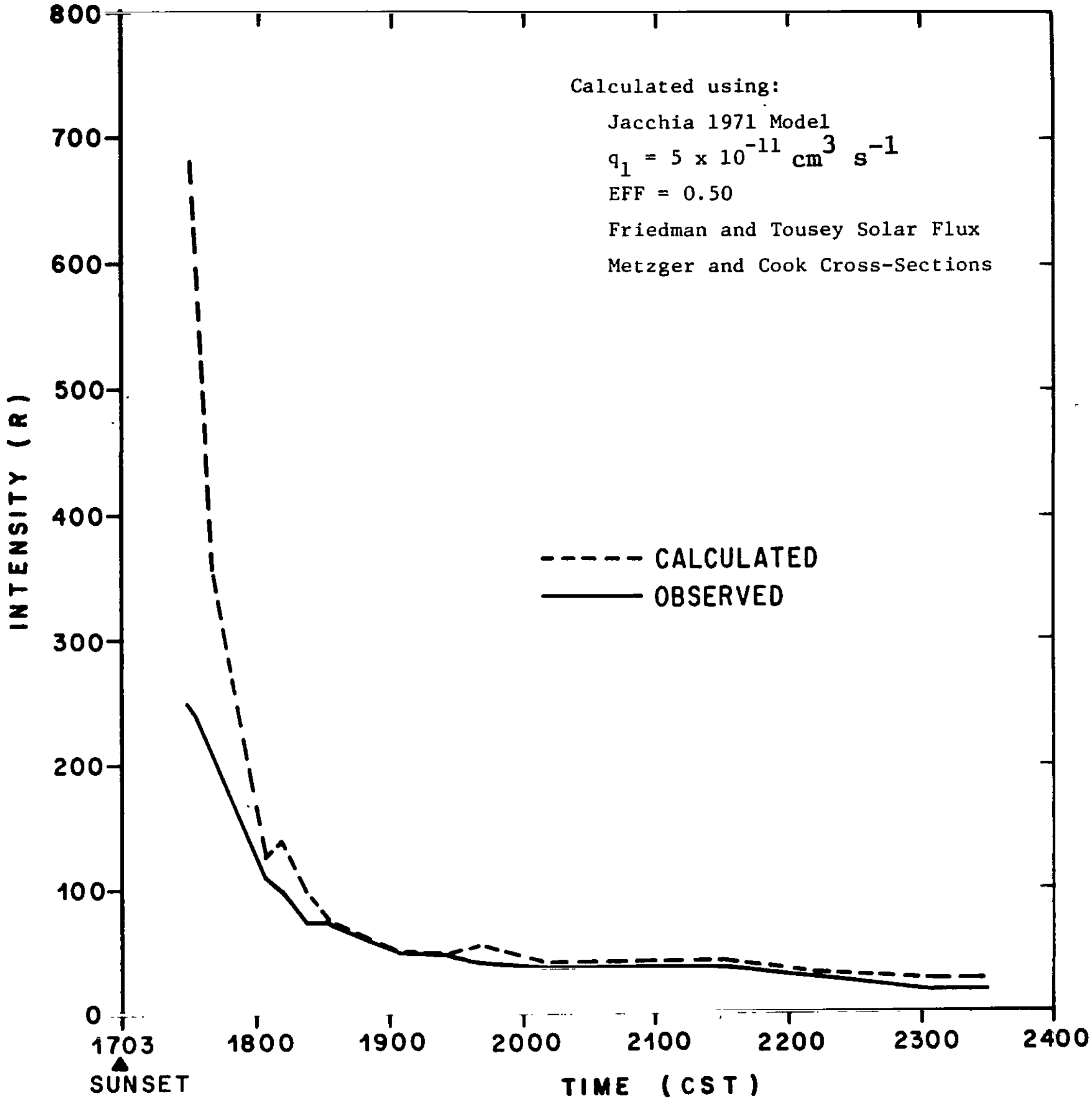

Figure 23. 6300 Å emission line intensities derived from Fabry-Perot interferometer observations and theoretically calculated intensities as a function of time after sunset on January 6, 1972.

In Figure 26 the quenching coefficient has been increased to 1×10^{-10} cm^3 s^{-1} without changing the efficiency of the dissociative recombination production mechanism. Agreement between calculated and observed emission intensities has been improved throughout the period; however, the calculated intensities are still larger than those observed at both 2303 and 2330 CST.

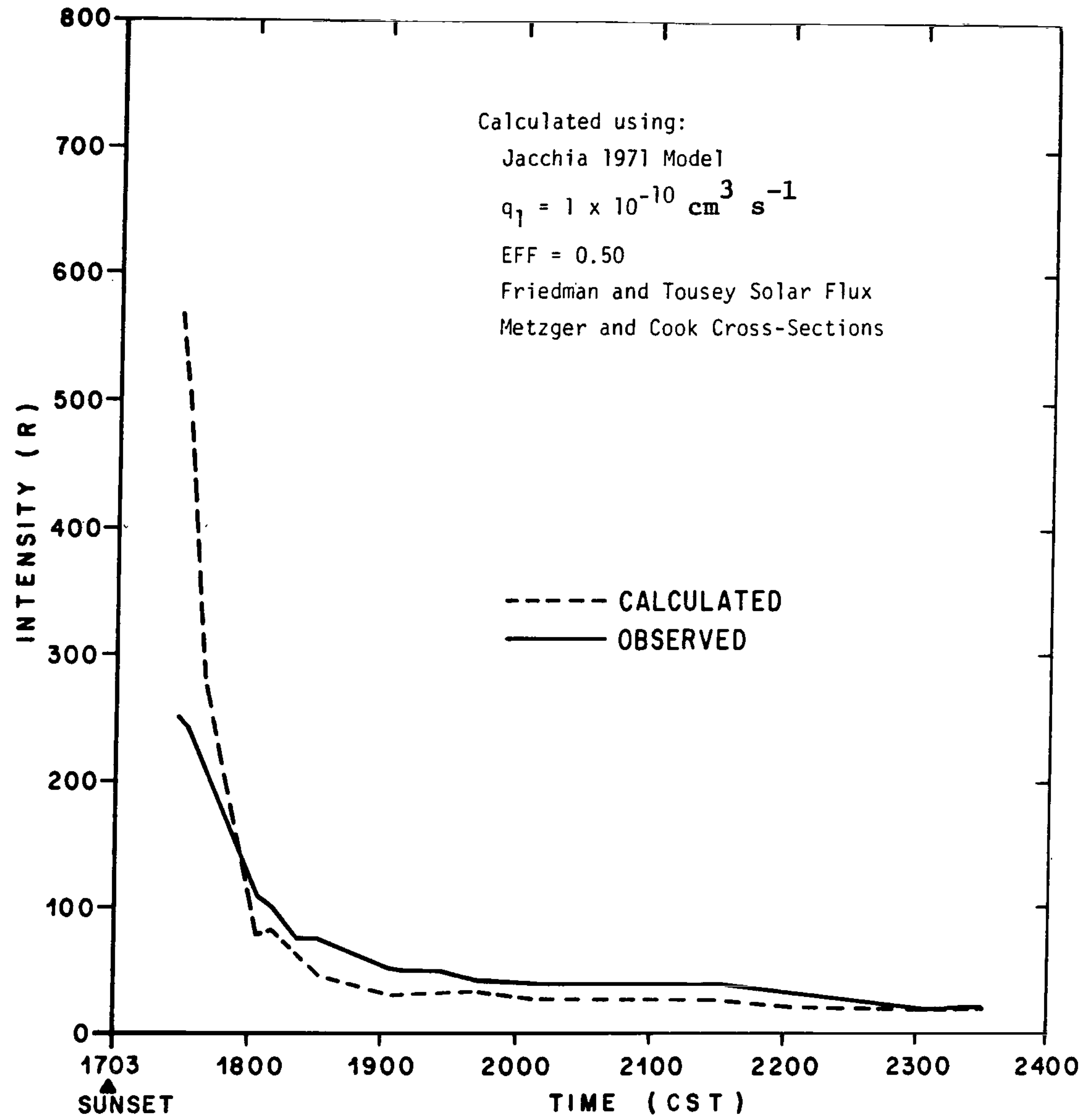

Figure 24. 6300 Å emission line intensities derived from Fabry-Perot interferometer observations and theoretically calculated intensities as a function of time after sunset on January 6, 1972.

In Figure 27 the quenching coefficient remains at 1×10^{10} cm^3 s^{-1}, while the production mechanism efficiency has been reduced to 0.434. Agreement between calculated and observed intensities at both 2303 and 2330 CST is excellent. That is the best combination of values for this model atmosphere; however, if the fictitious flux and diffusion terms recommended by Reber had

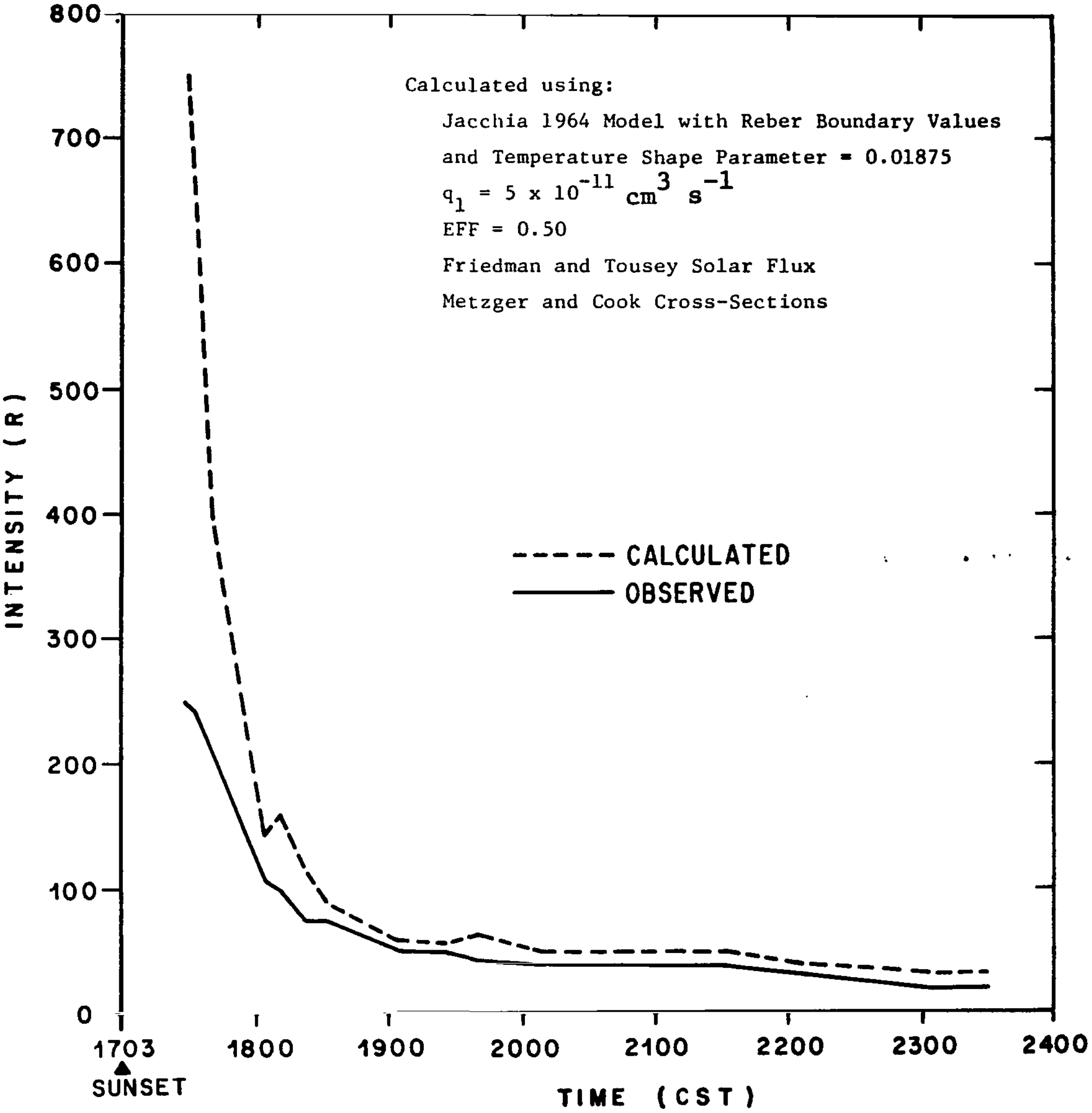

Figure 25. 6300 Å emission line intensities derived from Fabry-Perot interferometer observations and theoretically calculated intensities as a function of time after sunset on January 6, 1972.

been included so that his number density-height profiles would have been produced by the model, a quenching coefficient of approximately 9×10^{-11} cm^3 s^{-1} and a production mechanism efficiency of approximately 0.60 would probably have been the best combination of values.

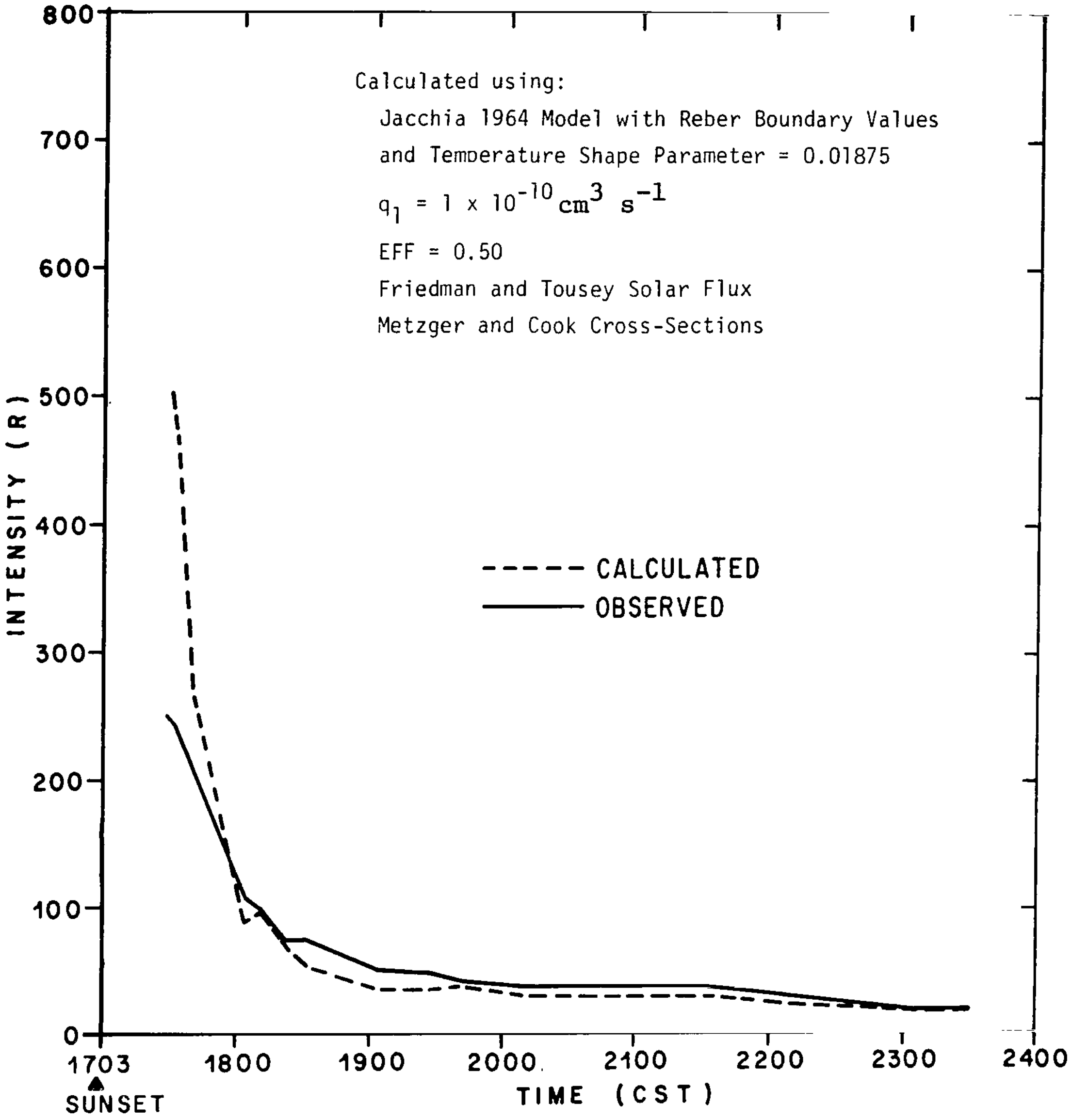

Figure 26. 6300 Å emission line intensities derived from Fabry-Perot interferometer observations and theoretically calculated intensities as a function of time after sunset on January 6, 1972.

B. Solar Radiation Fluxes and Associated Absorption Cross Section Effects

Once agreement between calculated and observed intensities resulting only from the dissociative recombination process has been attained, it seems reasonable to assume that the preferred values of the quenching rate coefficient

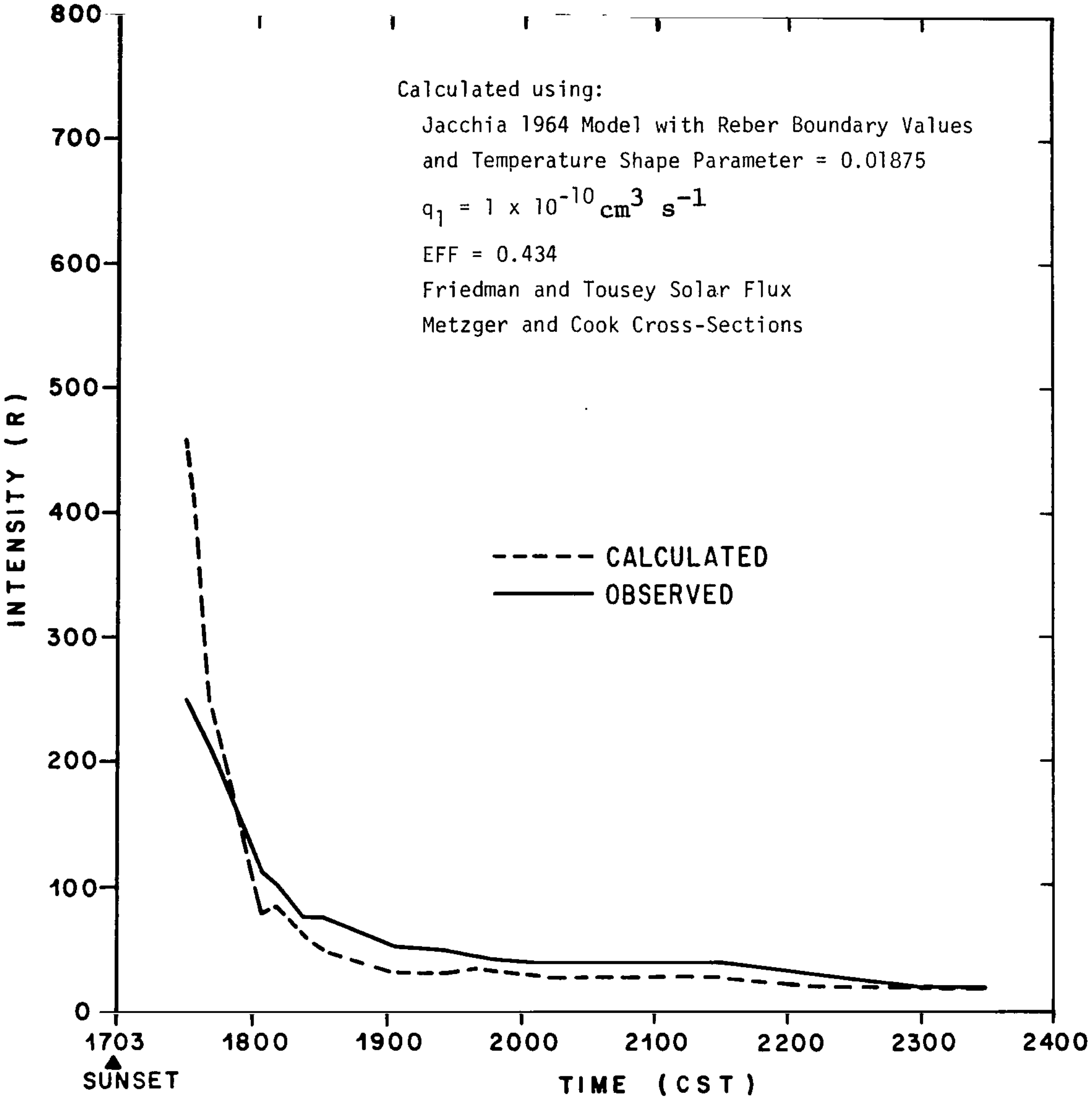

Figure 27. 6300 Å emission line intensities derived from Fabry-Perot interferometer observations and theoretically calculated intensities as a function of time after sunset on January 6, 1972.

and the O_2^+ + e production mechanism efficiency so established for each atmospheric model should remain constant during the remainder of the comparisons in which other parameters make an important contribution. In this section the Schumann-Runge continuum fluxes and their associated absorption cross sections are varied to study their effects on the calculated intensities.

Figures 28 and 29 are comparisons of observed intensities with intensities calculated using the Jacchia 1964 model atmosphere, a quenching rate coefficient of 1×10^{-10} cm^3 s^{-1}, an O_2^+ + e production mechanism efficiency of 0.333, and Hinteregger et al. [6] reported fluxes with the Metzger and Cook [7] cross sections (Table 13) and the Ackerman [5] recommended fluxes and cross sections (Table 14), respectively.

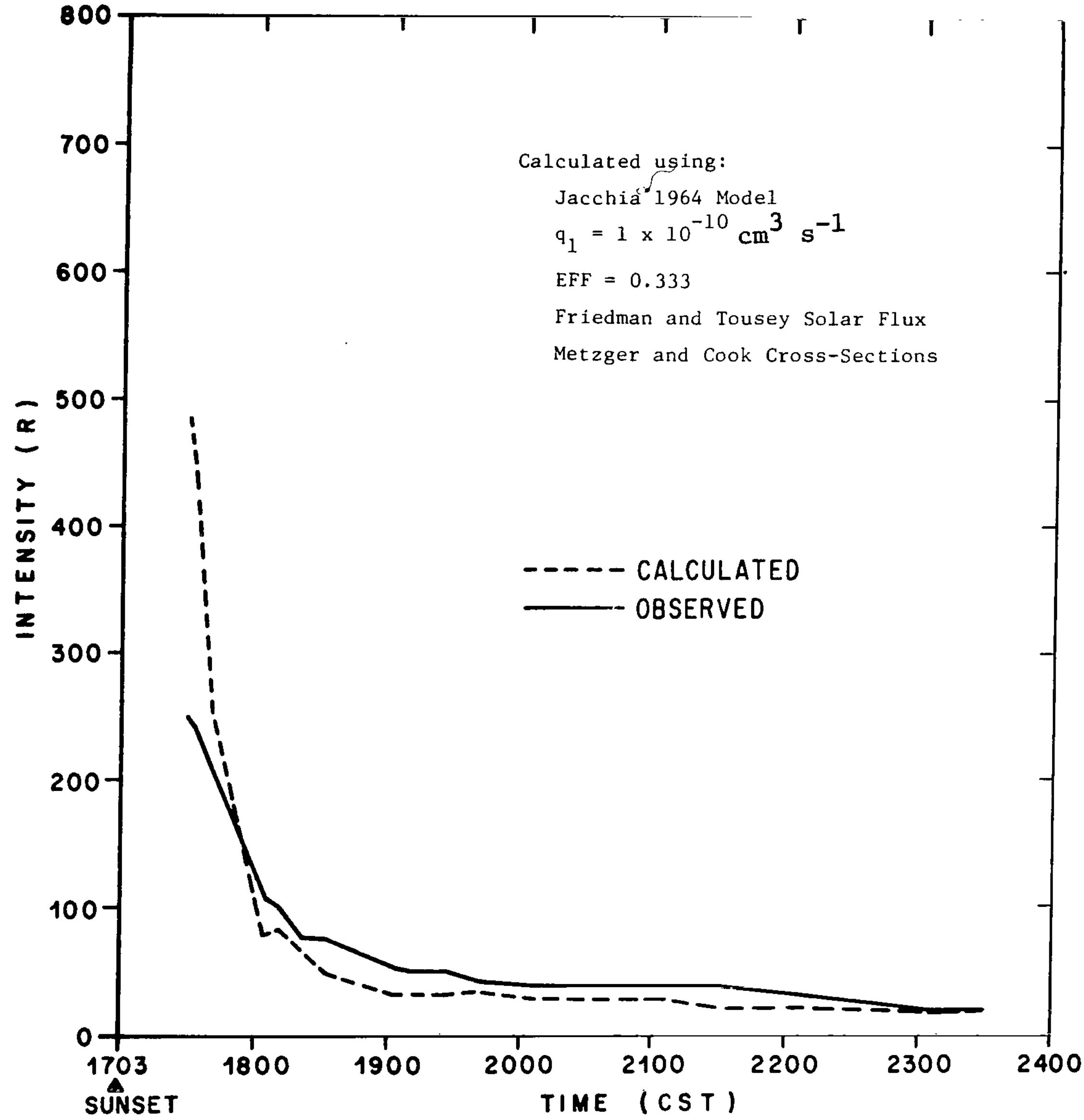

Figure 28. 6300 Å emission line intensities derived from Fabry-Perot interferometer observations and theoretically calculated intensities as a function of time after sunset on January 6, 1972.

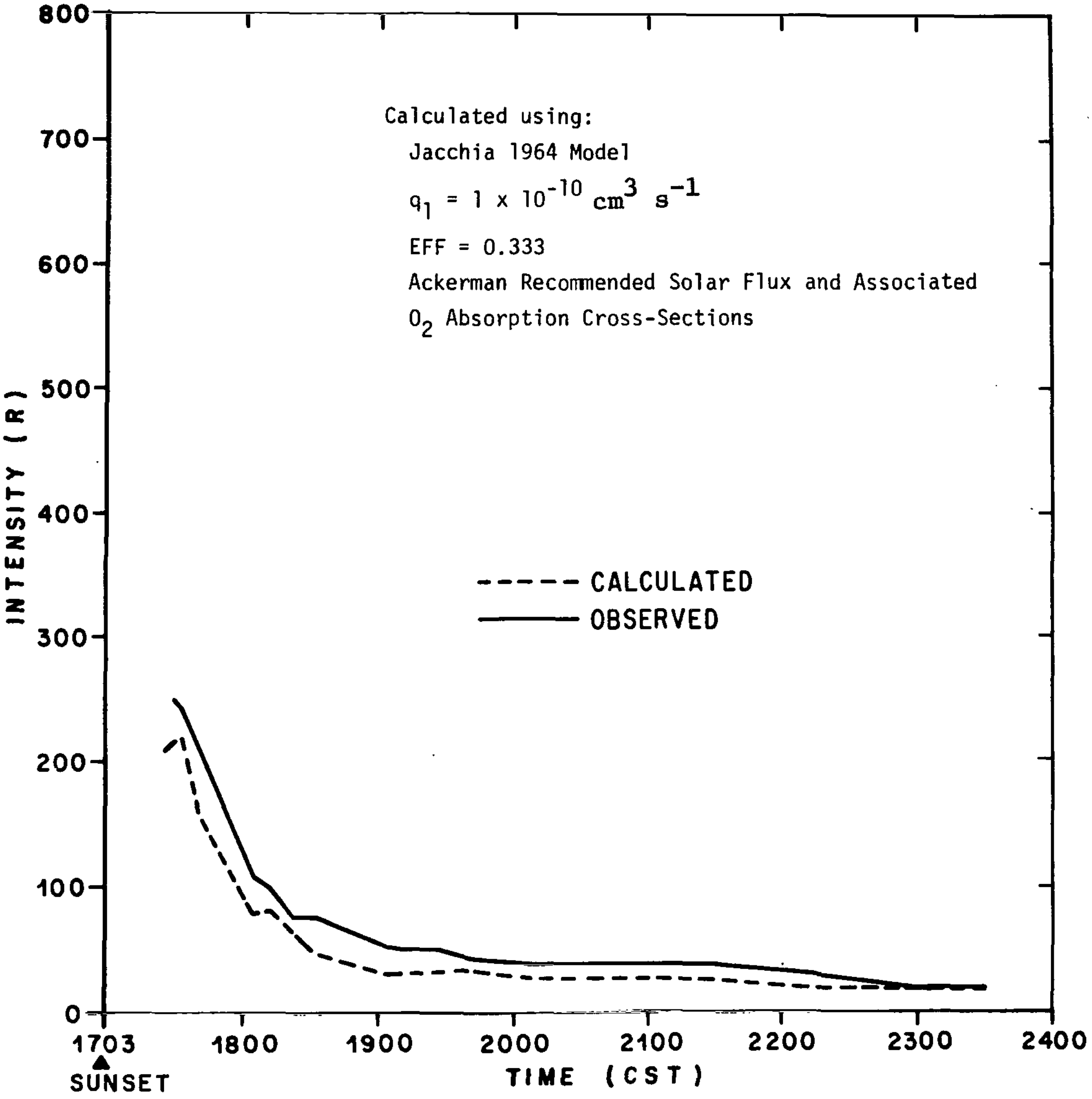

Figure 29. 6300 Å emission line intensities derived from Fabry-Perot interferometer observations and theoretically calculated intensities as a function of time after sunset on January 6, 1972.

In Figure 28 the agreement of the calculated and observed intensities at 2303 and 2330 CST deteriorates immediately and becomes progressively worse as one gets nearer the time of sunset. Between sunset and approximately 1811 CST, the time period when the dissociative photoexcitation process contributes significantly to the overall intensity of the 6300 Å emission, the calculated intensities are significantly larger than the observed intensities. From 1811 CST to approximately 2300 CST, the calculated intensities are smaller than the observations with the difference between the two decreasing with time after sunset.

In Figure 29 the agreement of the calculated and observed intensities at 2303 and 2330 CST once again becomes progressively worse the nearer one gets to the time of sunset; however, the major difference between these results and those shown in Figure 28 is that the calculated intensities are always smaller than the observed intensities.

From a comparison of these two analyses, it appears that either the Hinteregger et al. reported fluxes are not representative of the incoming solar flux on the night of January 6, 1972, or the associated Metzger and Cook cross sections are incorrect. It also appears that if the Ackerman recommended fluxes and absorption cross sections are indeed representative of the solar conditions, there is another source of $O(^1D)$ atoms on this night. The magnitude of this contribution is shown as a function of time in Figure 30. This is comparable to the results reported by Wickwar [36] and attributed to direct impact excitation of atomic oxygen by conjugate point photoelectrons. His results and those here show that the enhancement continues until at least conjugate point sundown which occurred on January 6, 1972, at approximately 2233 CST assuming a screening height of 180 km. At this time the conjugate point solar zenith angle was approximately 103°, which is less than the approximate 105° conjugate point solar zenith angle at which Wickwar [36] reported a cessation of the enhancement over Arecibo, P.R. The time at which the conjugate point (CP) photoelectron contribution ceased is in excellent agreement with Figure 5 of Reference 143 which shows that during a period of low solar activity, CP photoelectrons should not be present over the Huntsville area after 2300 CST in January. The magnitude of this conjugate point photoelectron impact excitation contribution is much larger than the approximate 20 R contribution over Blue Hill Observatory, Mass., reported by Noxon and Johanson [133] and somewhat larger than that reported by Wickwar [36].

Figures 31 and 32 are comparisons of observed intensities with calculated intensities using the Jacchia 1971 model atmosphere, a quenching rate coefficient of 1×10^{-10} cm^3 s^{-1}, and a dissociative recombination production mechanism efficiency of 0.50 with the Hinteregger et al. [6] and Metzger and Cook [7] combination of fluxes and cross sections and the Ackerman [5] fluxes and cross sections, respectively. The only differences in these two calculations occur prior to 1805 CST where the intensities calculated with the Hinteregger et al. and Metzger and Cook data combination (Fig. 31) are approximately 80 percent

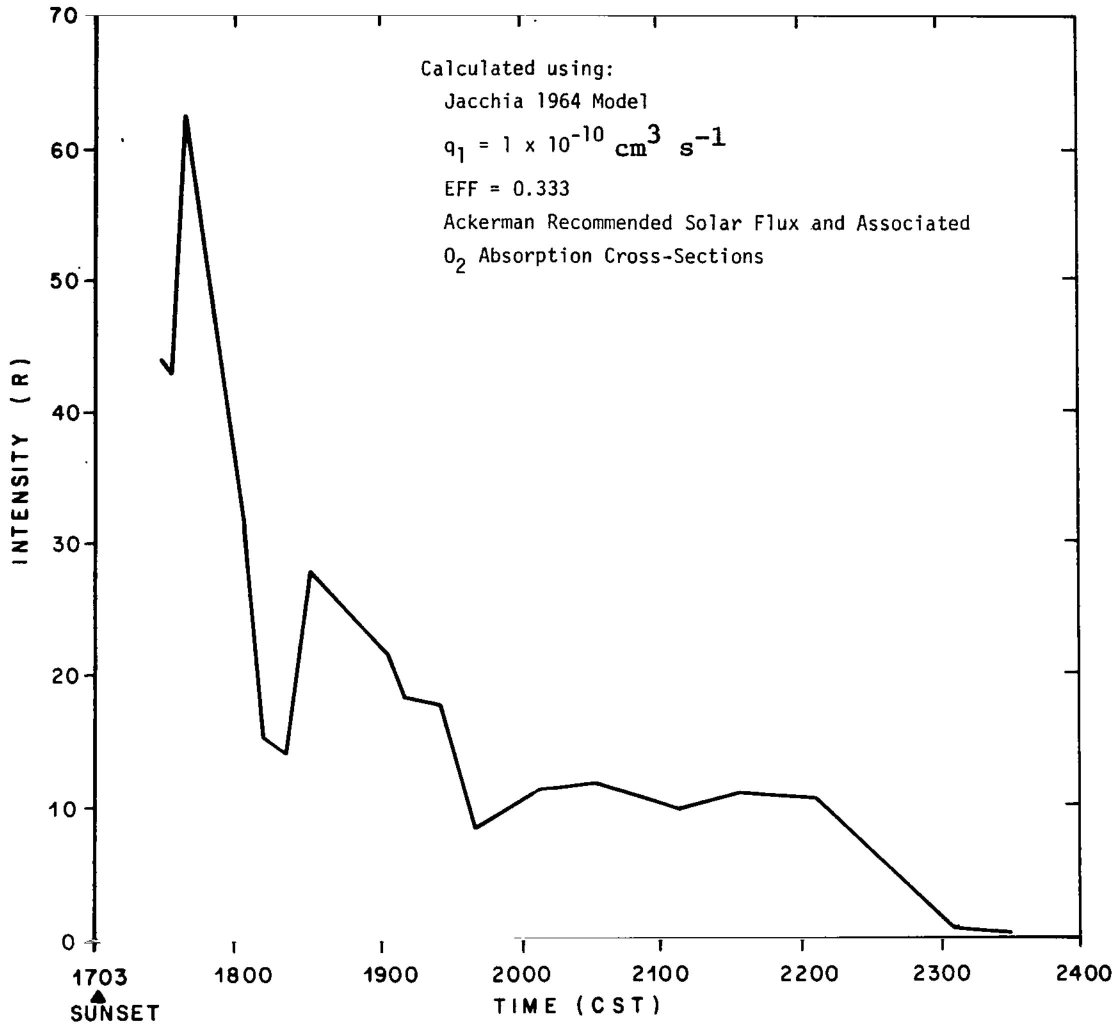

Figure 30. Difference between observed and calculated 6300 Å emission line intensities as a function of time after sunset, attributed to direct impact excitation of atomic oxygen by conjugate point photoelectrons.

larger than the observed intensities, while those calculated with the Ackerman data are about 20 percent less than the observed. If the Jacchia 1971 model is truly representative of the atmosphere on this night, the Hinteregger et al. and Metzger and Cook combination is not a representative set of solar fluxes and absorption cross sections. On the other hand, if the Jacchia 1971 model and the Ackerman data are both representative, there must be a third source of O(^{1}D) atoms. Again, this could be the direct impact excitation of oxygen atoms by conjugate point photoelectrons with the contribution at Huntsville continuing

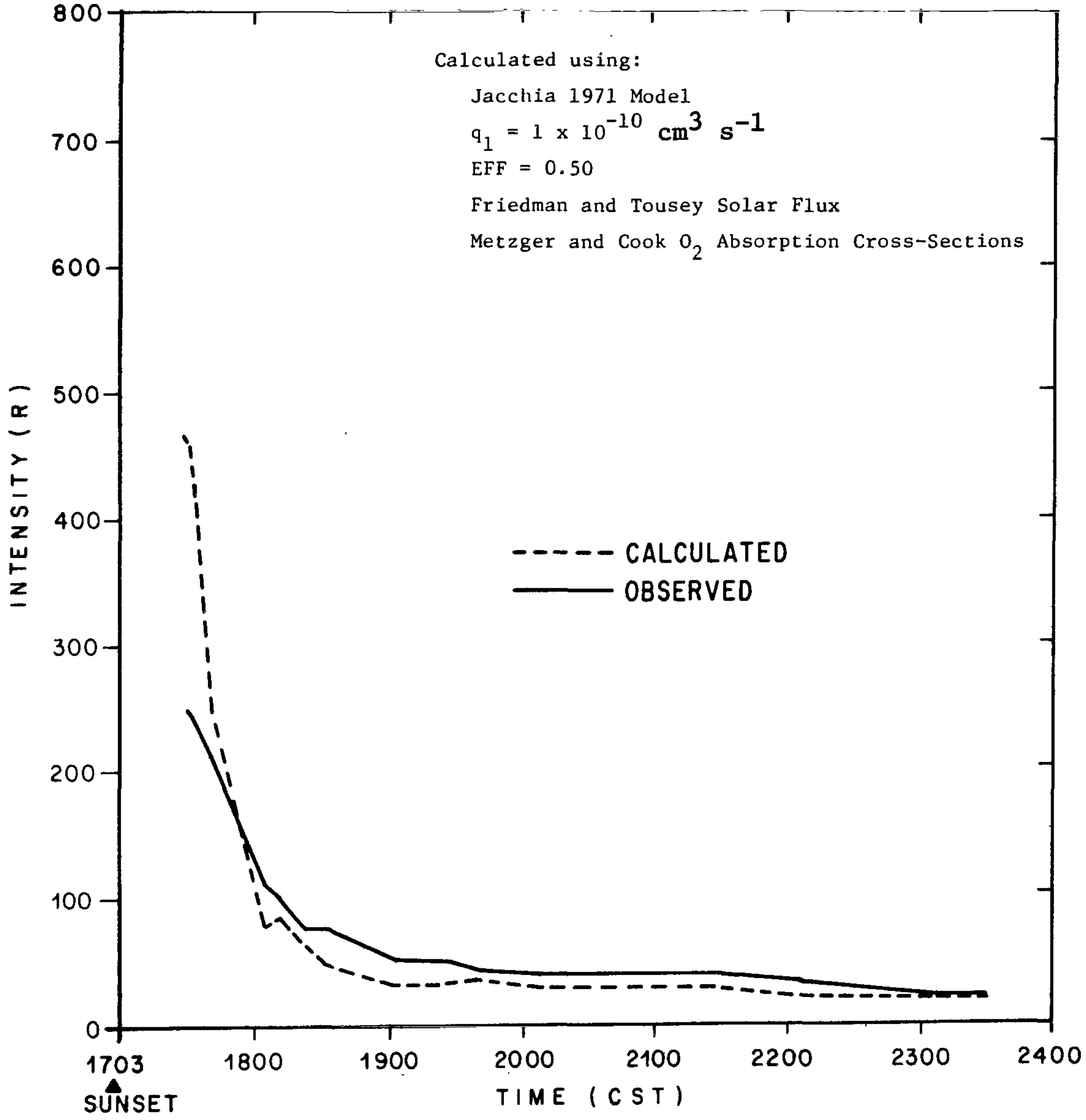

Figure 31. 6300 Å emission line intensities derived from Fabry-Perot interferometer observations and theoretically calculated intensities as a function of time after sunset on January 6, 1972.

until conjugate point sundown at approximately 2233 CST. Figure 33 shows the magnitude of this third contribution as a function of time. As with the results obtained using the Jacchia 1964 model, the contribution ceases approximately at the same cutoff time observed over Arecibo, P. R., as reported by Wickwar [36].

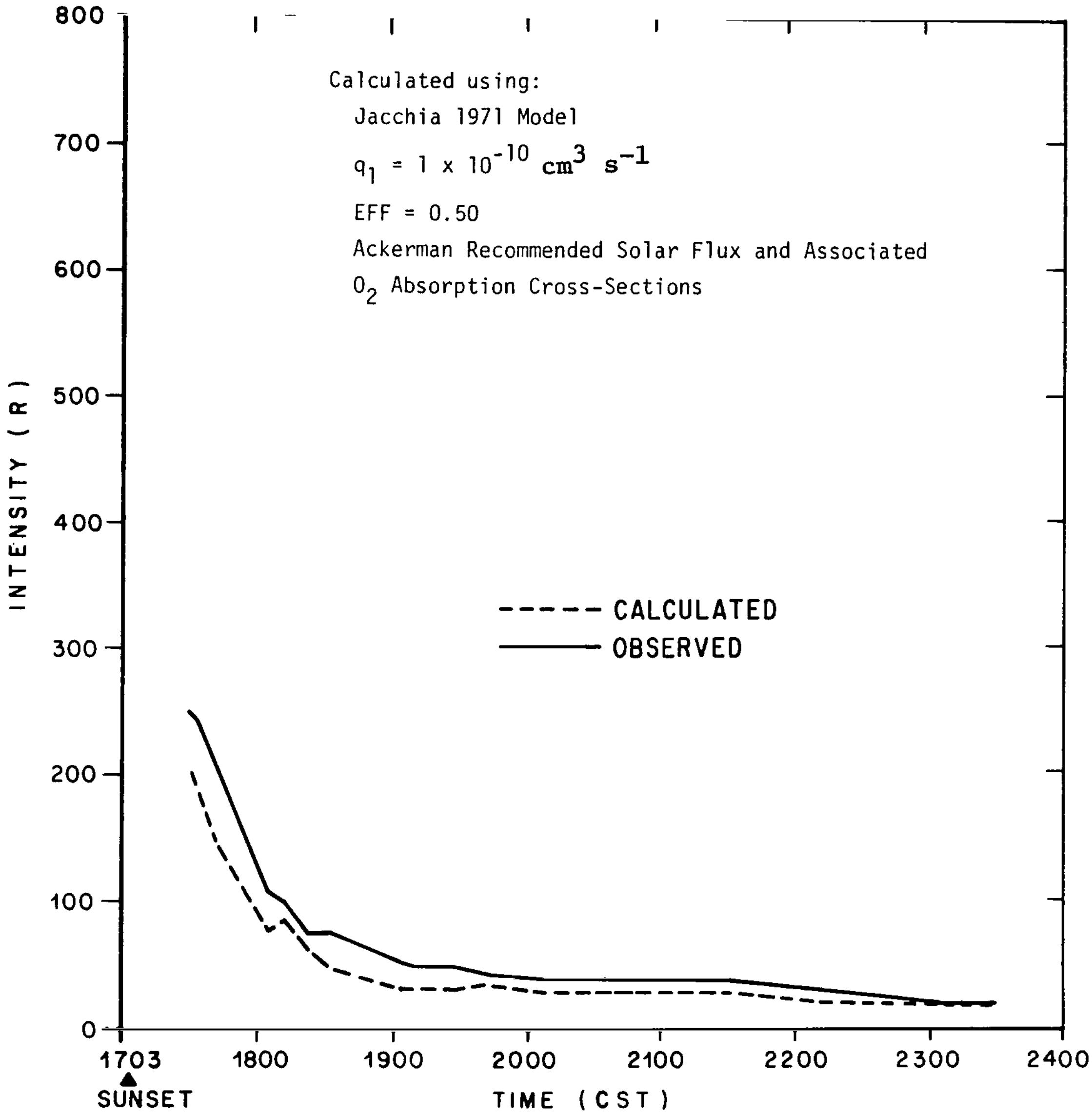

Figure 32. 6300 Å emission line intensities derived from Fabry-Perot interferometer observations and theoretically calculated intensities as a function of time after sunset on January 6, 1972.

Figures 34 and 35 show the same comparison using the Jacchia 1964 model formulation with the boundary conditions and temperature shape parameter proposed by Reber without the vertical diffusion and flux corrections. Although these results can be discussed only qualitatively, they are identical to those

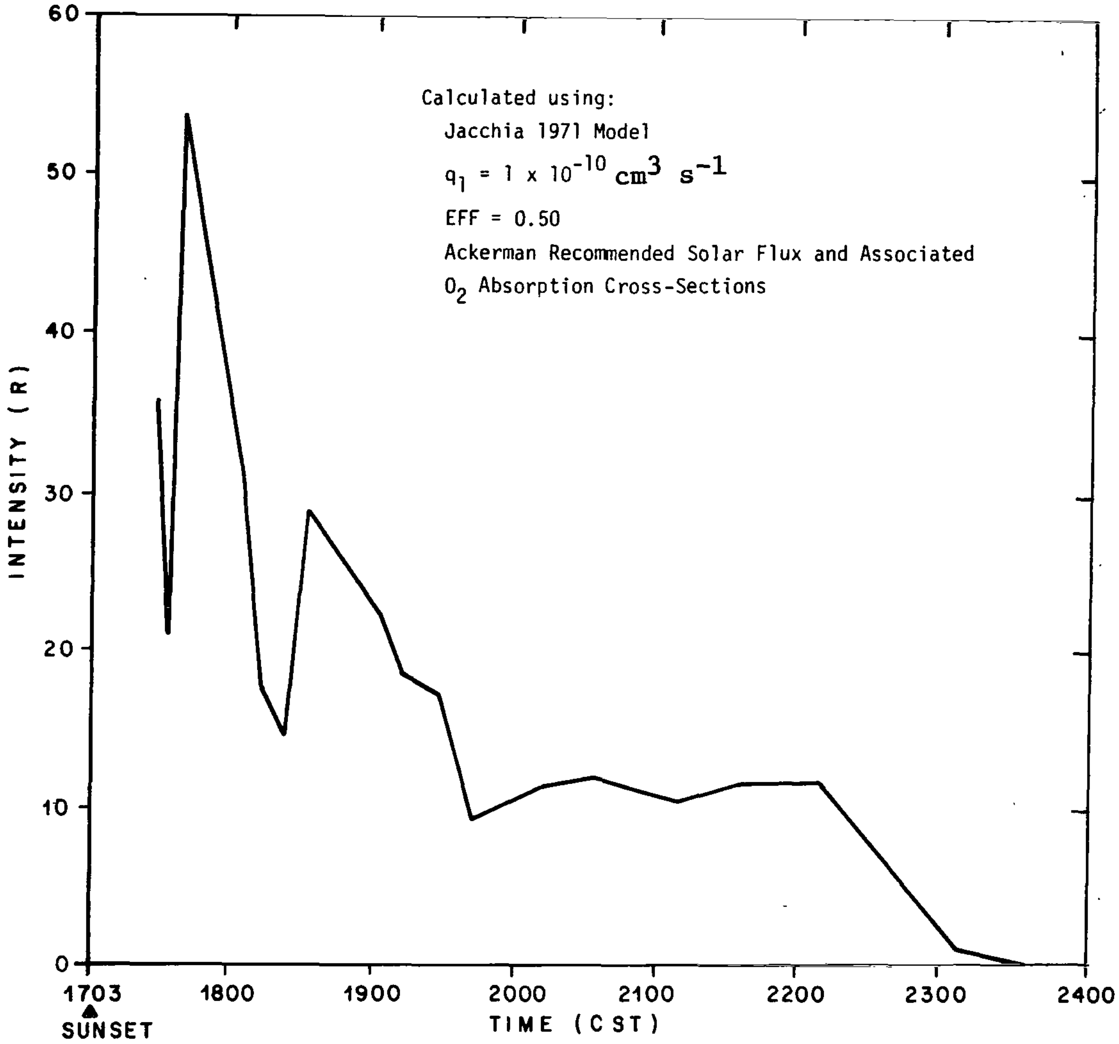

Figure 33. Difference between observed and calculated 6300 Å emission line intensities as a function of time after sunset, attributed to direct impact excitation of atomic oxygen by conjugate point photoelectrons.

using both the Jacchia 1964 and 1971 model atmospheres. If both this model and the Ackerman data are representative, then a third source of $O(^1D)$ atoms of approximately the same magnitude is present with the variation with time as shown in Figure 36.

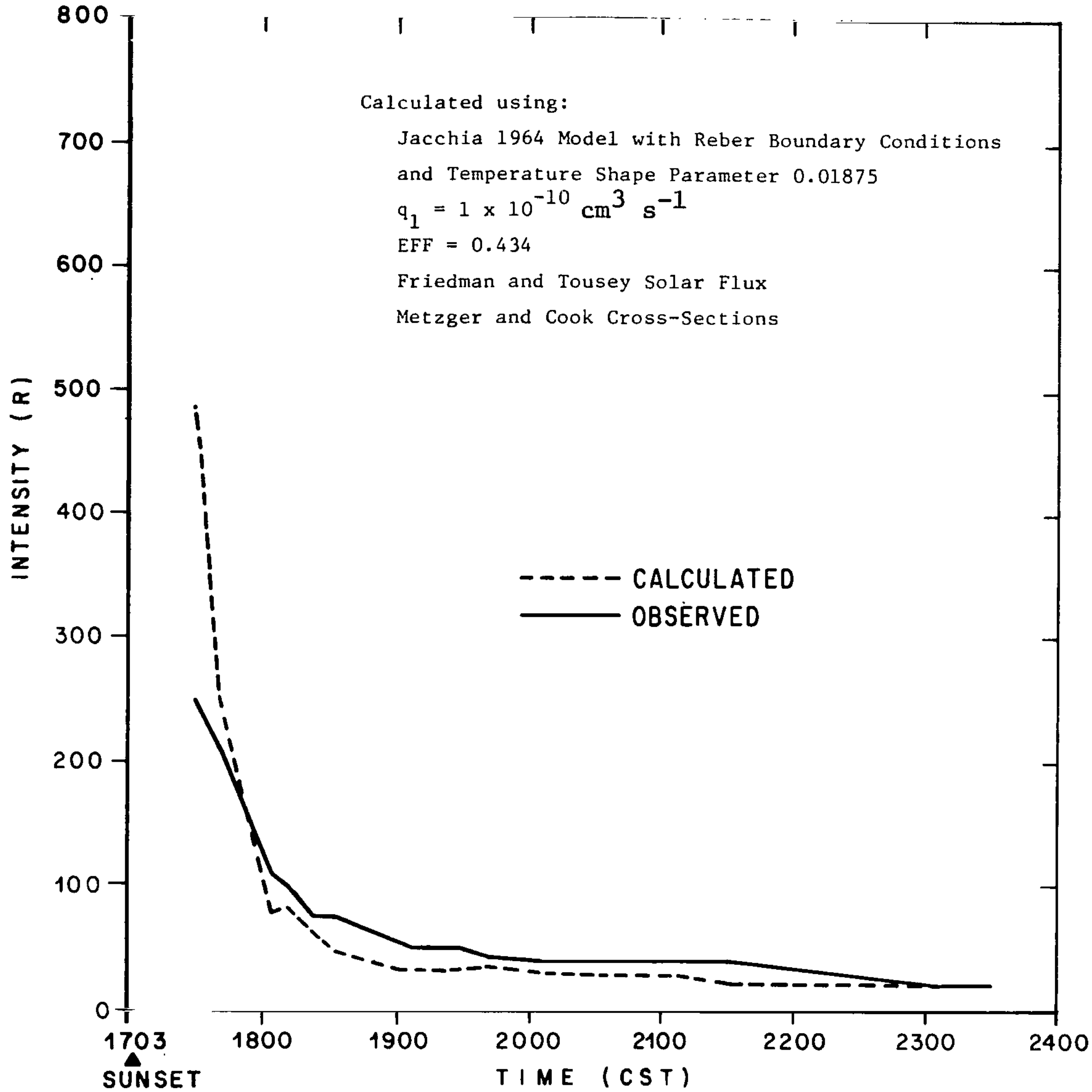

Figure 34. 6300 Å emission line intensities derived from Fabry-Perot interferometer observations and theoretically calculated intensities as a function of time after sunset on January 6, 1972.

C. Neutral Gas Temperature Effects

Estimated errors in temperatures derived from the F-P observations range from approximately ±85 K near sunset to approximately ±195 K at midnight, as shown in Figure 18. If the actual temperatures are higher than

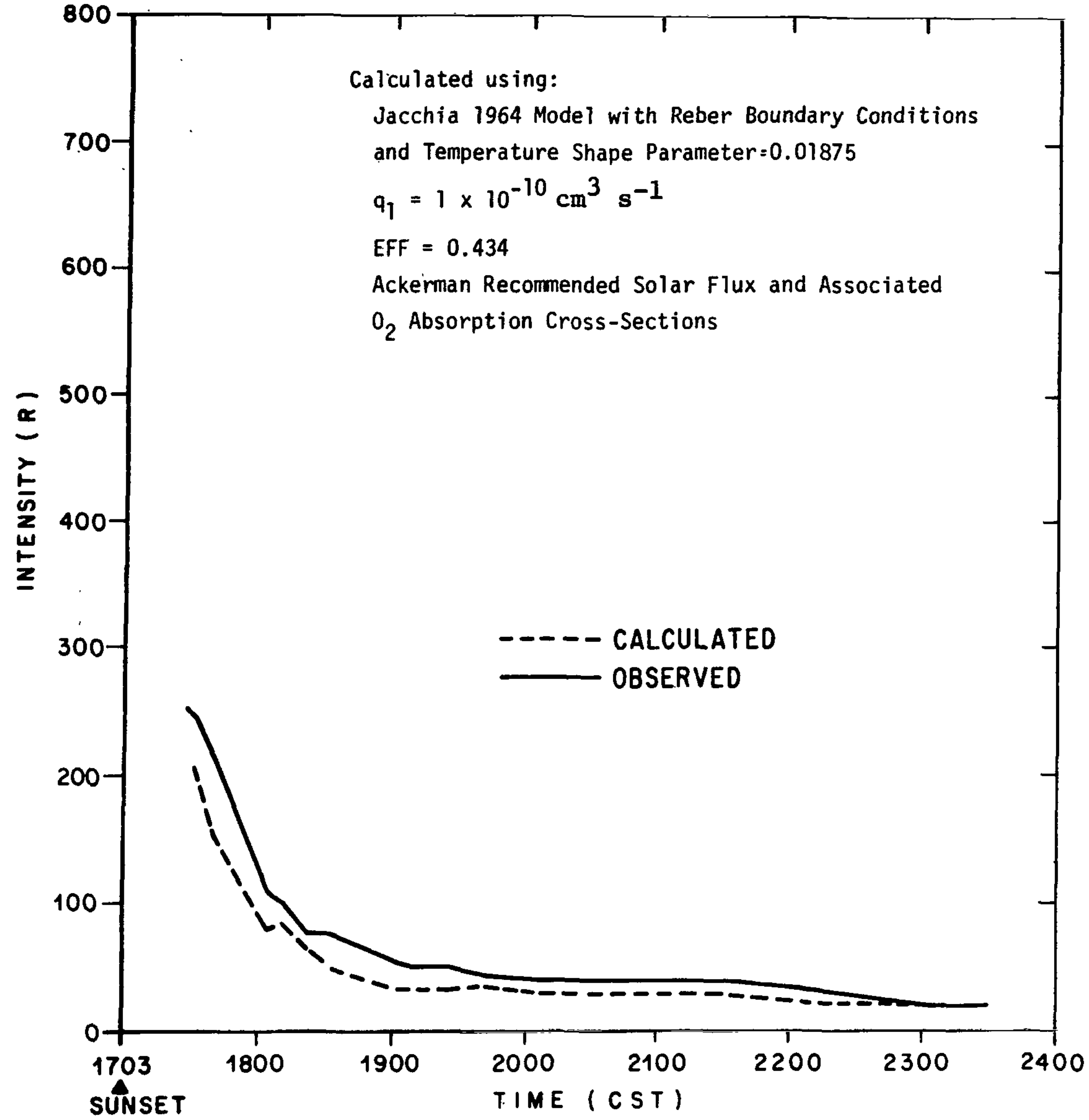

Figure 35. 6300 Å emission line intensities derived from Fabry-Perot interferometer observations and theoretically calculated intensities as a function of time after sunset on January 6, 1972.

the ones derived from the Fabry-Perot interferometer measurements that were used in theoretically calculating the intensities used in this analysis, then:

1. The N_2 quenching rate coefficient of 1×10^{-10} cm^3 s^{-1}, determined as a result of this analysis, is too small by approximately 9 to 10 percent, or

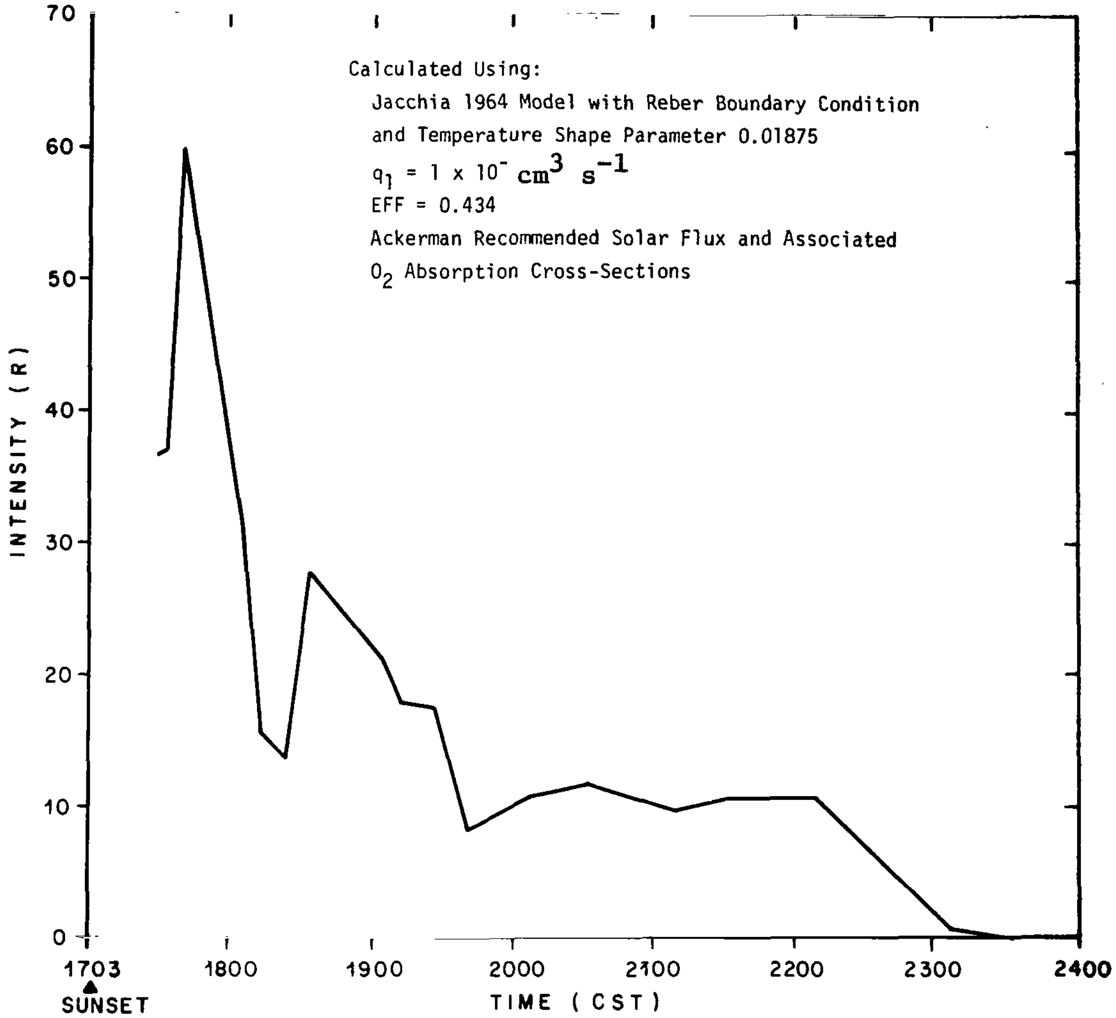

Figure 36. Difference between observed and calculated 6300 Å emission line intensities as a function of time after sunset, attributed to direct impact excitation of atomic oxygen by conjugate point photoelectrons.

2. The dissociative recombination production mechanism efficiency of 0.50 is too large by approximately 9 to 10 percent, or

3. Both of these results are in error by a lesser amount such that the combination is in error by approximately 9 to 10 percent.

Figures 37 and 38 are plots of constant N_2 number density and volume emission rate, respectively, as a function of solar zenith angle for January 6-7, 1972, for each time during the observational period when simultaneous

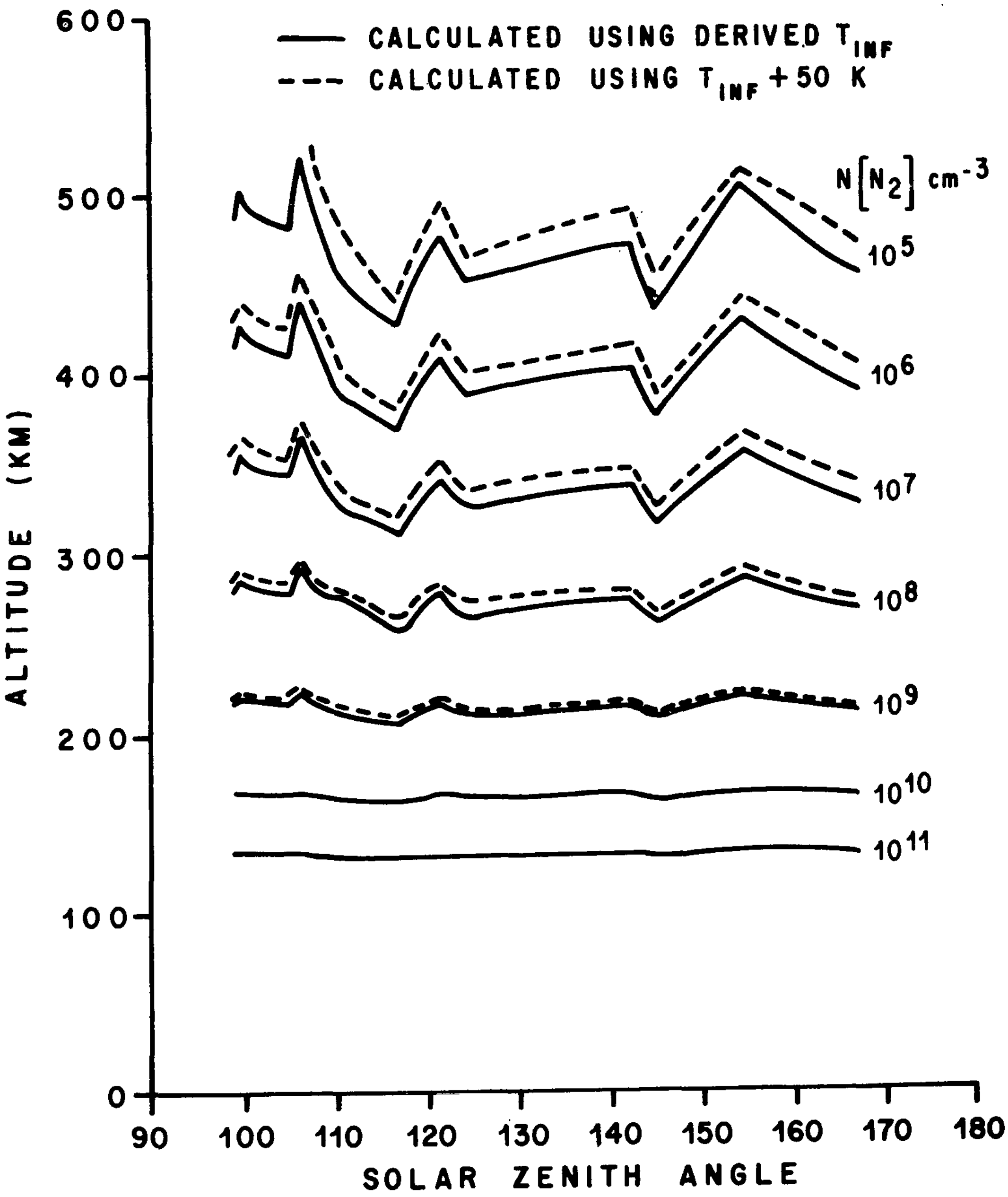

Figure 37. Contours of constant N_2 number density.

observations of the electron density-height profile, the integrated intensity and an exospheric temperature from the Fabry-Perot interferometer, and integrated intensity from the turret photometer were available. The solid line in each of the figures shows the computational results using the actual temperatures derived

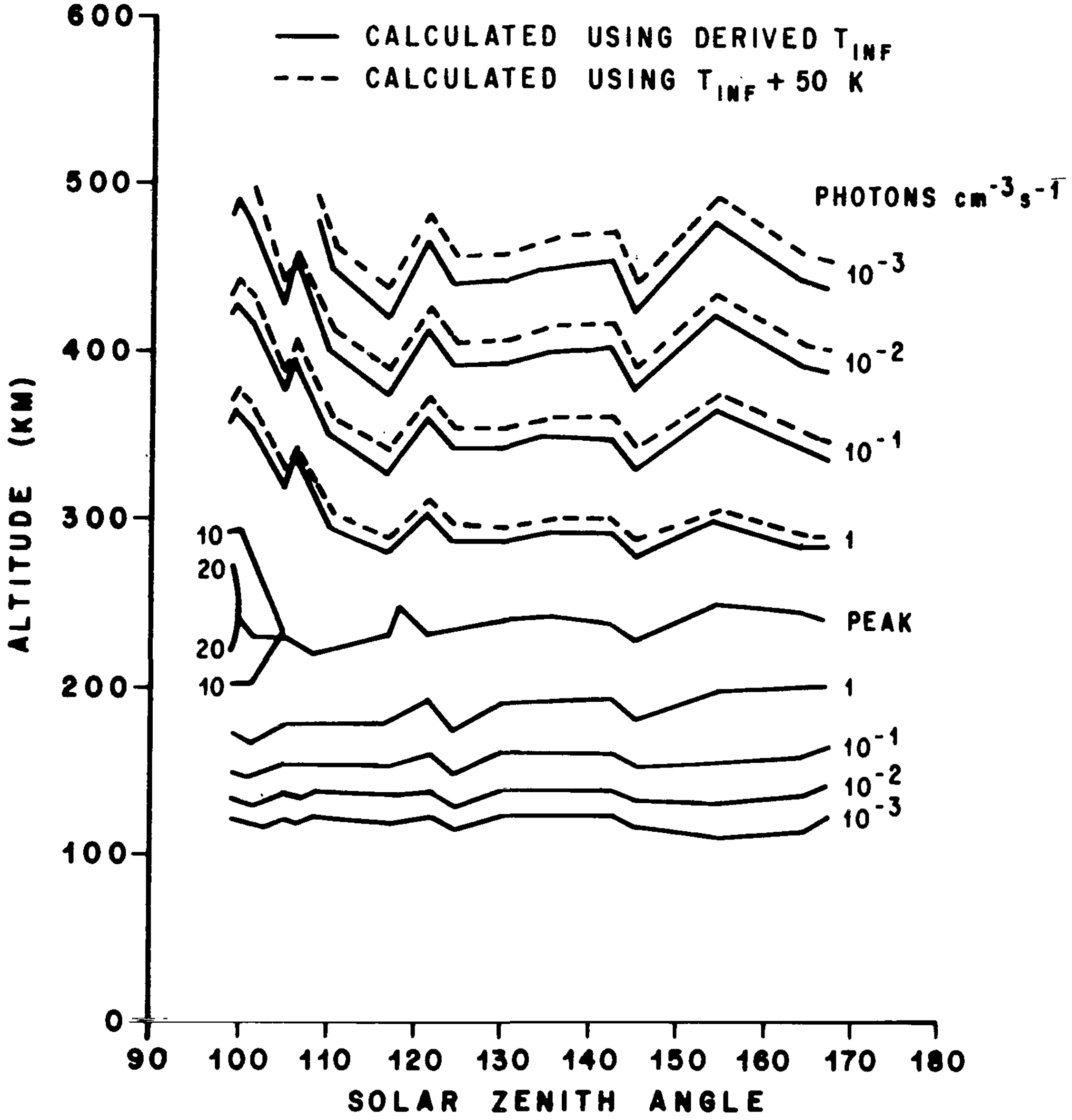

Figure 38. Contours of constant volume emission rate.

from the F-P measurements, while the dotted lines show the results using temperatures increased by 50 K. Figure 37 shows that the model of the atmosphere expands upward with increased exospheric temperature, while Figure 38 shows that the contours of constant volume emission rate are also displaced upward while the peak volume emission rate values are increased approximately

2 to 3 percent. The calculated integrated intensities are increased 9 to 10 percent. Figure 39 shows calculated and observed intensities as a function of time with the same inputs to the calculations, while Figure 40 shows the third source contribution under these conditions. Exospheric temperatures derived from Fabry-Perot interferometer measurements are used in these calculations

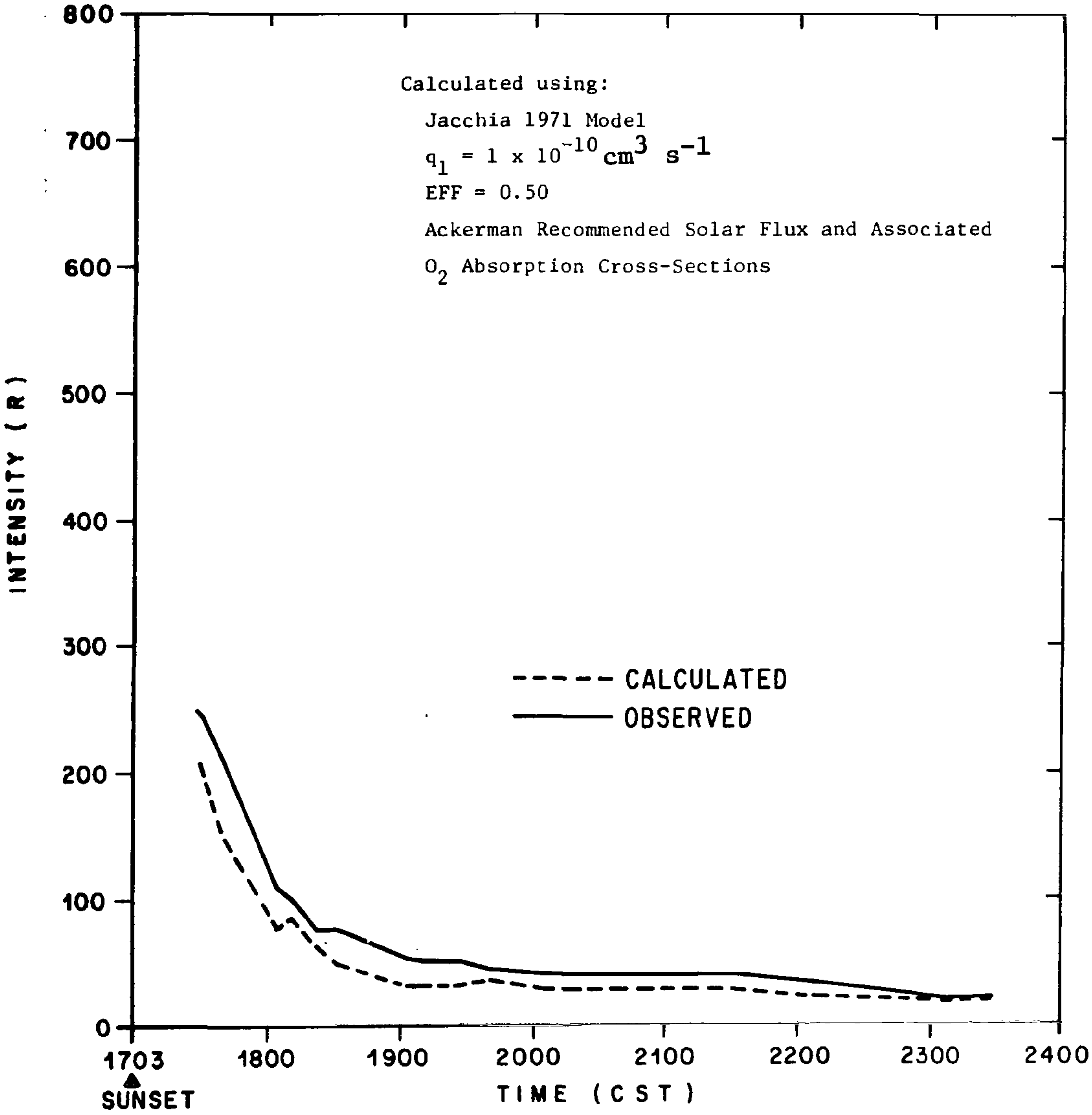

Figure 39. 6300 Å emission line intensities derived from Fabry-Perot interferometer observations and theoretically calculated intensities as a function of time after sunset on January 6, 1972.

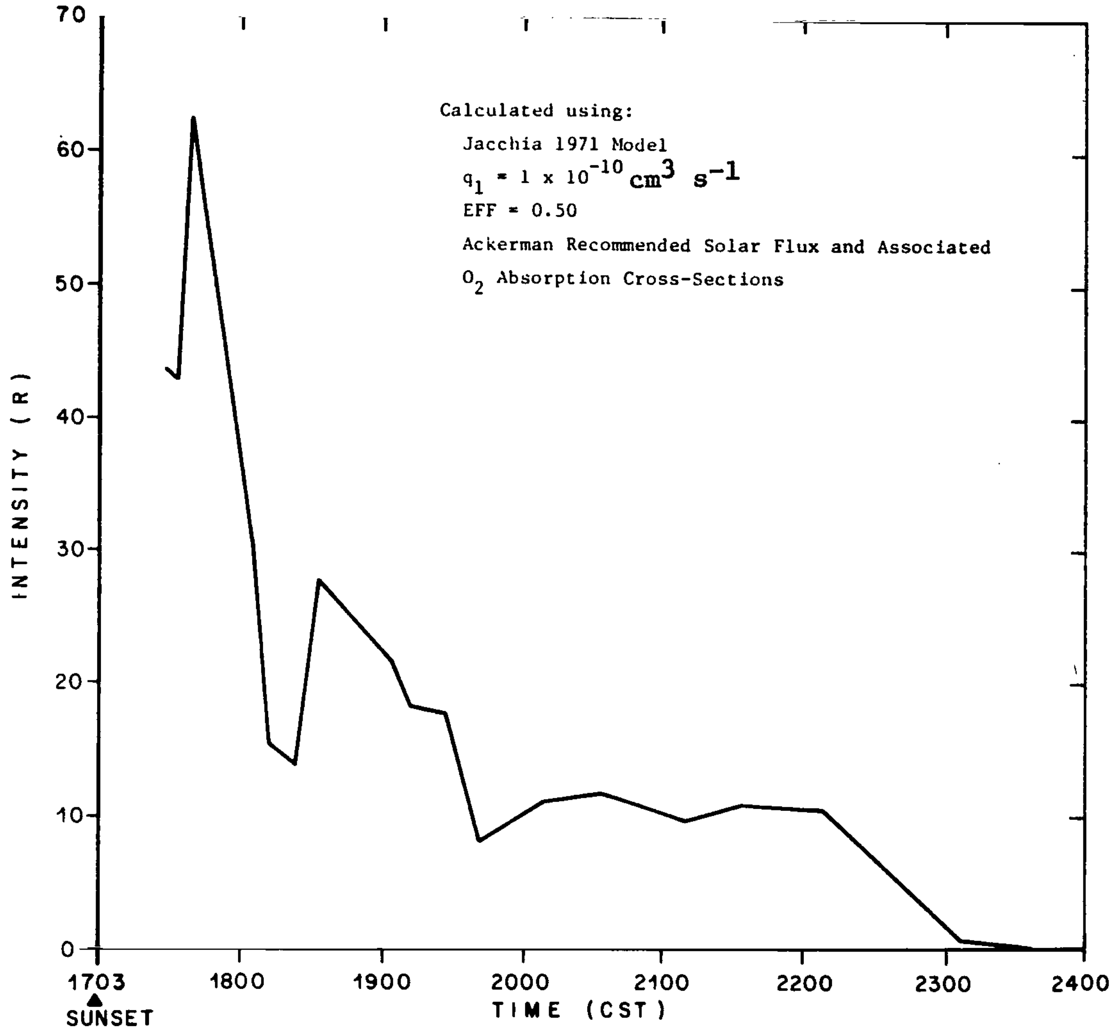

Figure 40. Difference between observed and calculated 6300 Å emission line intensities as a function of time after sunset, attributed to direct impact excitation of atomic oxygen by conjugate point photoelectrons.

with the Jacchia 1971 model atmosphere, a quenching rate coefficient of 1×10^{-10} cm^3 s^{-1}, a dissociative recombination production mechanism efficiency of 0.50, and the Ackerman [5] recommended values for the Schumann-Runge continuum with associated absorption cross sections. In these figures the altitude of the peak of the volume emission rate, I, can be considered to be the same as the altitude of the derived temperature. The height of this peak is variable; however, in all instances it is between 220 and 255 km. In the Jacchia 1971 model atmosphere this is well below the altitude where the atmosphere becomes isothermal, for all practical purposes; therefore, the derived temperatures should be lower by 15 to 25 K than the true exospheric temperatures.

Figure 41 shows the observed and calculated intensities on January 6, 1972, where the calculations are based on the same inputs as those used for the results shown in Figure 39 with the exception that the exospheric temperature

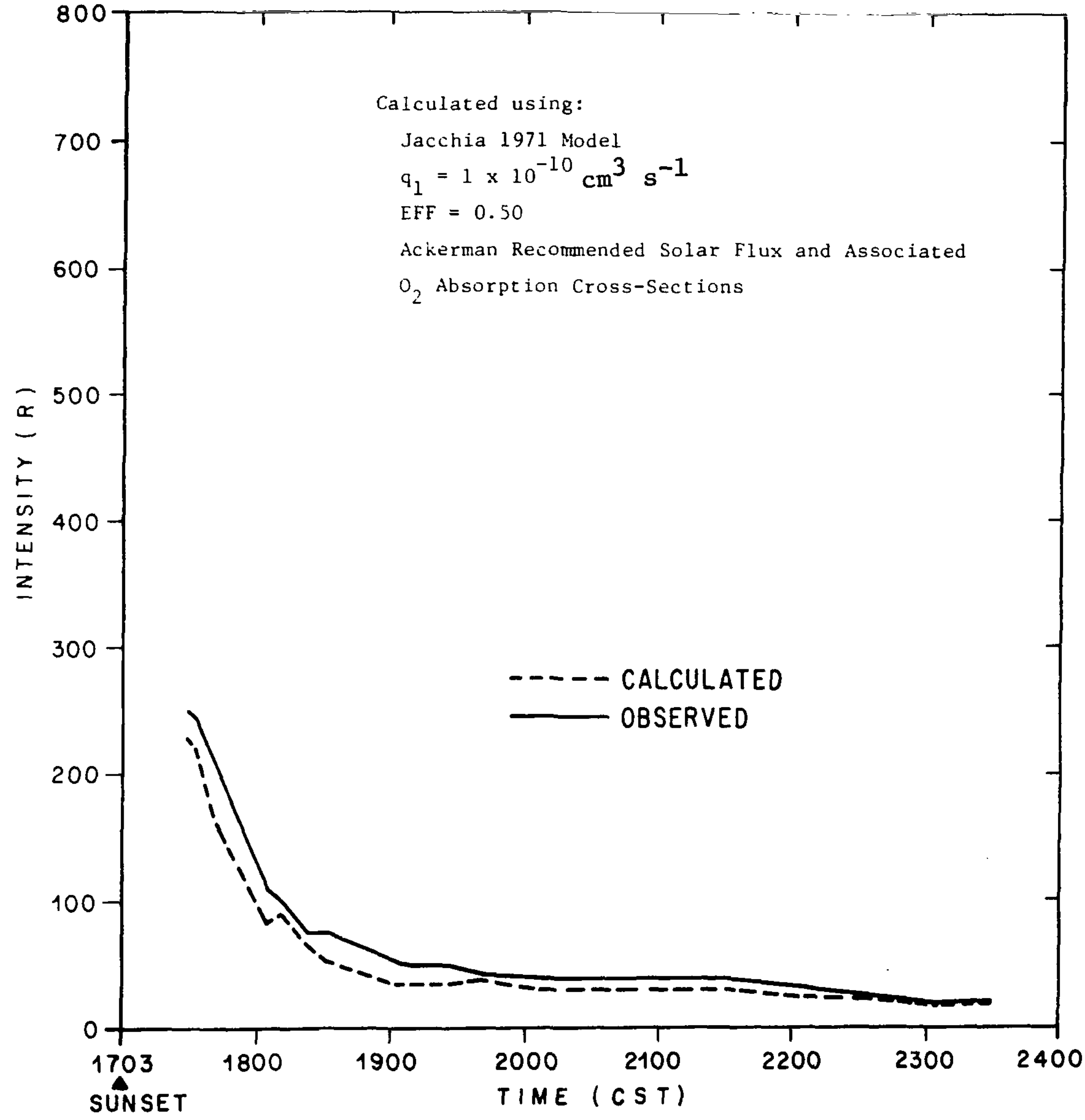

Figure 41. 6300 Å emission line intensities derived from Fabry-Perot interferometer observations and theoretically calculated intensities as a function of time after sunset on January 6, 1972.

values are all increased 50 K. The third source contributions under these conditions are shown in Figure 42. Since the contributions at 2303 and 2330 CST are both negative, the dissociative recombination process efficiency would have to be reduced and, once this is done, the results would be identical to those shown on Figure 40. Similar calculations have been made for the other models; however, since the results are almost identical, they are not shown here.

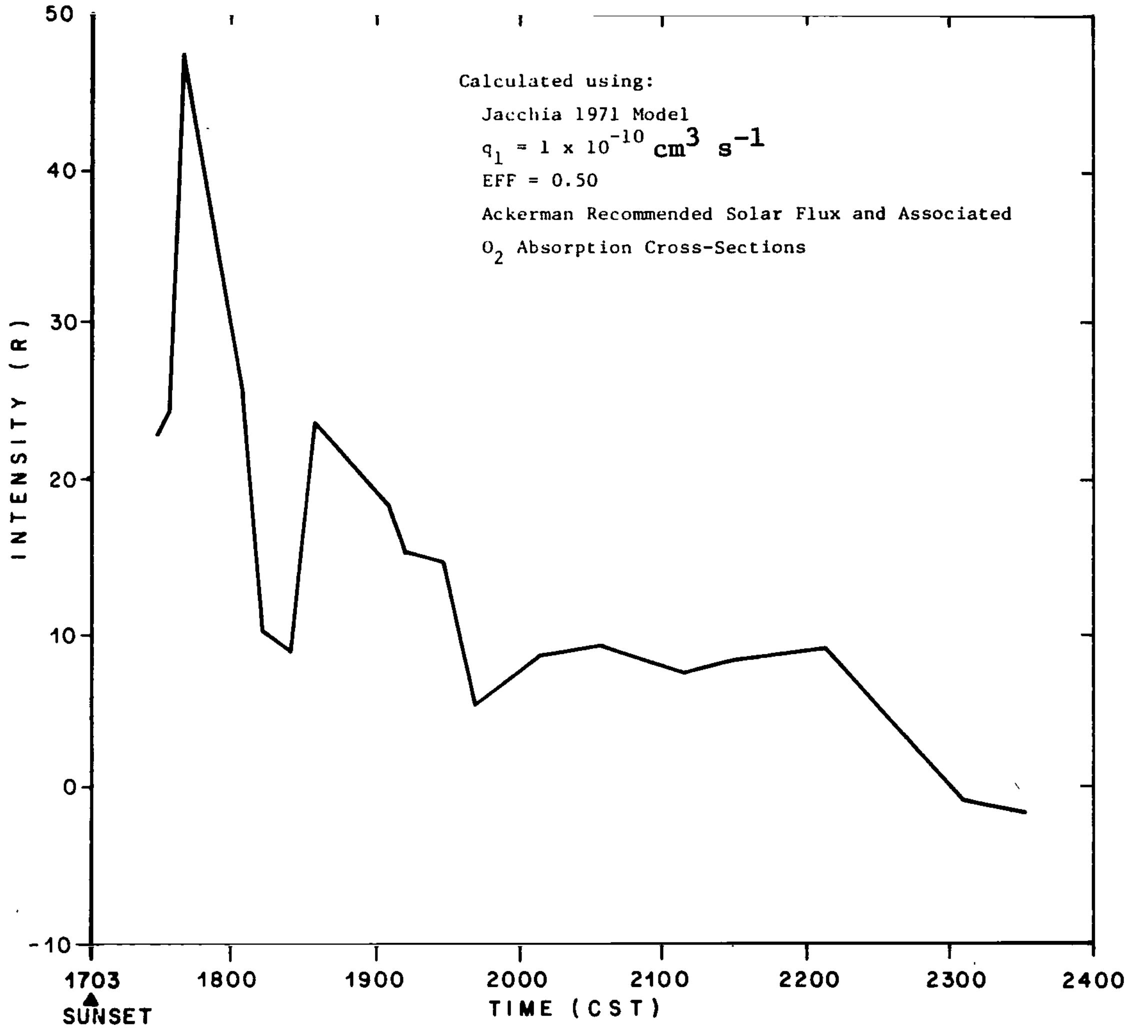

Figure 42. Difference between observed and calculated 6300 Å emission line intensities as a function of time after sunset, attributed to direct impact excitation of atomic oxygen by conjugate point photoelectrons.

D. Electron Density-True Height Profile Effects

There are several problems associated with the true height analysis of ionograms which, although they are outside the scope of this analysis, affect the results. Problems associated with the reduction of daytime ionograms obviously do not affect the results of this analysis; however, the start problem discussed in detail in ionospheric literature, as well as all the scale problems, can significantly affect the results.

Scaling problems arise from multiple traces resulting from multiple reflections, some of which, or perhaps all, are from off-vertical reflections, proper selection of points to be used in the program, correct tracing of the negative on the scaling form, and correct identification of the ordinary and extraordinary ray signals. From the ionograms created by the standard C-4 ionosonde used in this study, it is impossible to discriminate between vertical and off-vertical returns if there are multiple traces on the film. Fortunately, for this analysis, enough ionograms were available to preclude the use of any with multiple traces; however, there is no way of knowing whether the single traces on the ionograms are from vertical incidence reflections or not. They have all been assumed to be from vertical incidence reflections.

As previously stated in Section III, the start problem was investigated by using several different programs in conjunction with several known electron density-true height profiles until the data reduction program output the known electron density-true height profiles, to the accuracy required, from which the input data were originally selected. This technique should minimize the possibility of large errors in the electron density-true height profiles; however, if errors do occur, the analysis shows that the reduction technique tends to underestimate the height of the F_2 maximum. These errors in height can be on the order of 10 to 20 km with the mean errors expected to be closer to 10 km. If the actual height of the F_2 maximum is approximately 10 km higher than the height calculated by the true height reduction technique, that portion of the intensity due to dissociative recombination computed using the calculated height will be approximately 20 percent greater than it actually is. This will lead to overestimating the value of the quenching coefficient and/or the molecular nitrogen number density and/or underestimating the dissociative recombination production mechanism efficiency and/or the molecular oxygen number density or various combinations of these.

Accurate electron density-true height profiles, especially near the F_2 maximum, are a necessity in 6300 Å emission line intensity analyses.

E. General

Figure 43 is a composite of the observational and theoretical data for the night of January 6, 1972. From Figures 43(a) and (b) it is readily apparent that each time the height of the F_2 maximum changed, there was a corresponding change in the temperature derived from the Fabry-Perot interferometer. The second line on Figure 43(a) shows that the altitude of the calculated maximum volume emission rate also varied in agreement with the two measured quantities; therefore, the temperature of a higher altitude layer of the atmosphere is being measured. Correspondence between changes in the altitude of the F_2 maximum and the height of the peak value of the volume emission rate is not as good during the early portion as it is during the latter portion of the twilight period. This is because there is a substantial contribution from the dissociative photoexcitation process in addition to the dissociative recombination process. This supports the conditions of Roble, Hays, Nagy [124] that the $O(^1D)$ atoms are in thermal equilibrium with the neutral atmosphere and 6300 Å emission can be used to monitor the exospheric temperature.

Figure 43(c) shows the electron density at the F_2 maximum, while Figure 43(d) shows a combination of observed and calculated intensities as a function of solar zenith angle. The top curve in Figure 43(d) represents the total observed intensity on the night of January 6, 1972. The bottom curve in this figure connects the intensity values attributed from the theoretical calculations at each observation time to the dissociative recombination of molecular oxygen ions.

On the left side of Figure 43 the difference between the short horizontal line and the observed intensity curve is attributed, from the calculations, to the dissociative photoexcitation of molecular oxygen by solar fluxes in the Schumann-Runge continuum. The remainder of the observed intensity, the difference between the bottom curve and the curve composed of the short horizontal lines at a value of 183 R and the total intensity curve between solar zenith angles of 104° and 162°, is believed to be due to direct impact excitation of atomic oxygen by conjugate point photoelectrons. As expected, there appears to be an excellent correspondence between the electron density curve and the curve that represents the intensity attributable, from the calculations, to the dissociative recombination process. This is shown in more detail in Figure 44 where the ○ 's show the observed intensity as a function of the electron density at the F_2 peak. There appears to be an excellent correspondence between the two parameters with the exception of those three points relating the higher intensities to the larger electron densities, and the deviation here is due to the contribution to the intensity from the dissociative photoexcitation process. If

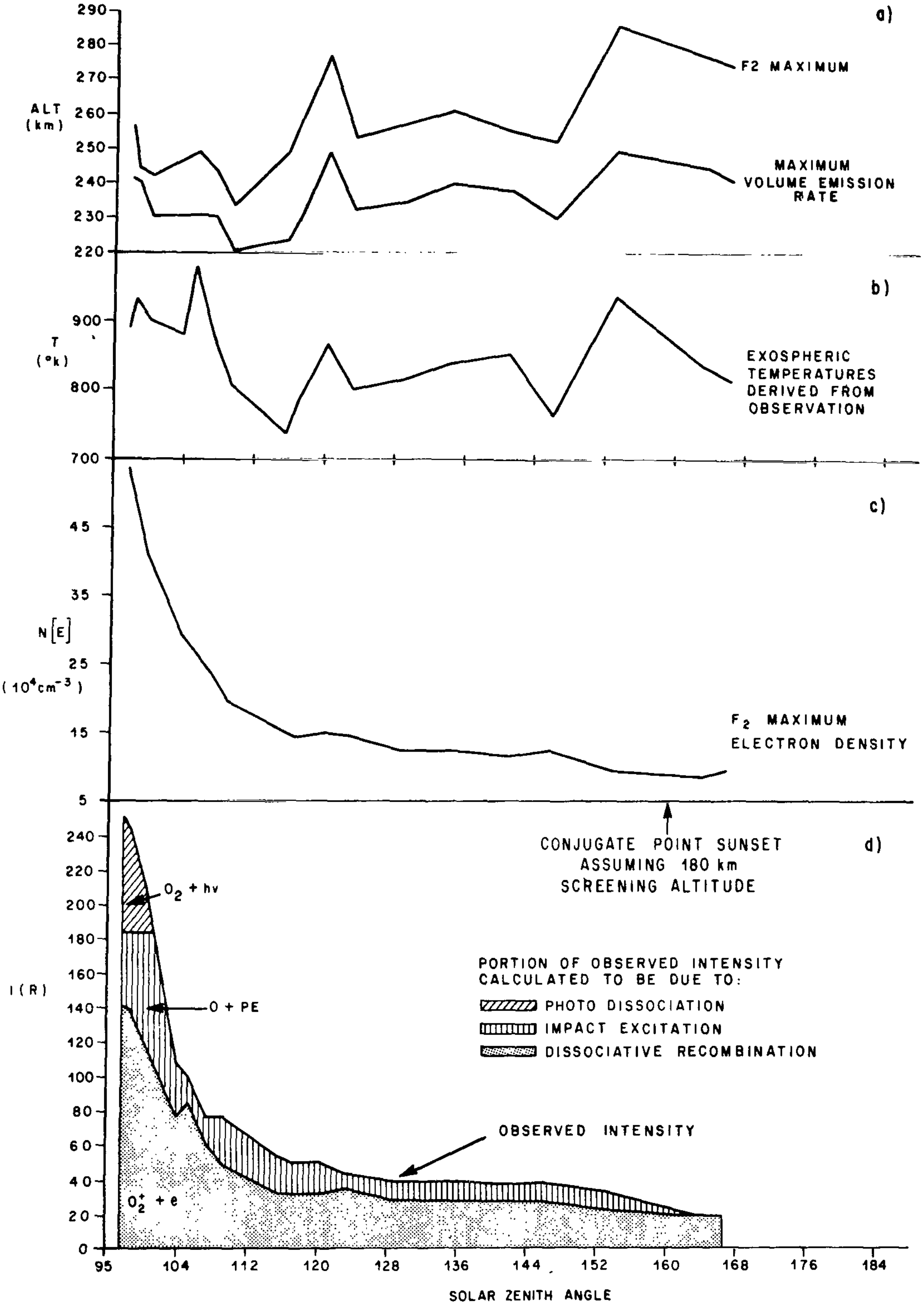

Figure 43. Composite of observational and theoretical data as a function of local solar zenith angle on January 6, 1972.

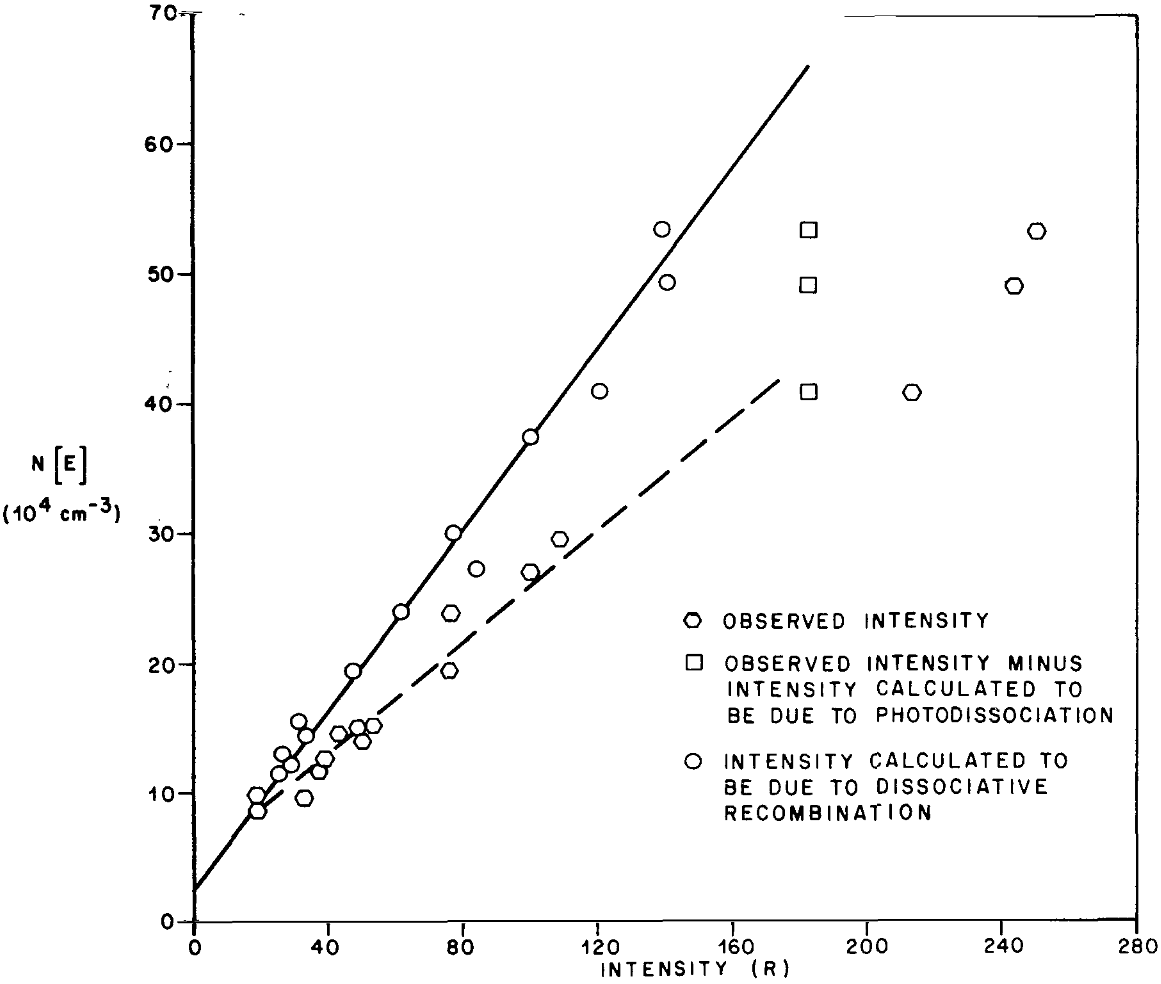

Figure 44. Observed and calculated 6300 Å intensities versus the electron number density at the F_2 peak.

this intensity was adequately calculated and its contribution removed, it would seem as if the resulting intensities should fall on the straight line defined by the other observed intensities and electron densities. The squares, which denote the results of subtracting the intensity calculated to be due to dissociative photoexcitation from the observed intensity, do not indicate the same correspondence between the electron density and 6300 Å intensity as the other observations; therefore, it appears as if there is a possibility that either the dissociative photoexcitation process is improperly modeled or there is a change in the electron density-dissociative recombination intensity relationship when the sun is contributing to the emission line intensity. These results are identical to those shown in Figure 43 (d), and both seem to indicate that the dissociative photoexcitation and dissociative recombination processes combine in some manner to effectively control the effect of conjugate point photoelectrons on the local 6300 Å OI emission. On Figure 44 the circles show the intensities, calculated on the basis of the dissociative recombination process only, as a function of the electron density at the F_2 peak. Correspondence between these two parameters is excellent, as expected. The equation of a straight line fit to these data is

$$I(R) = \left(\frac{20}{7}\right)(N_e - 2.50) \times 10^{-4} \quad .$$

When the calculated dissociative photoexcitation process contribution was subtracted from each observed intensity when the sunlight was making a contribution, a value of 183 R remained in each instance. From the previous equation the intensity should be 183 R when the electron density is 6.672×10^5 cm^{-3}. Perhaps this is an indication of how the conjugate point effects are controlled by the local ionosphere, but verification of that is beyond the scope of this analysis and, undoubtedly, would require much additional observational data.

Figure 45 compares the 6300 Å total emission intensity over Huntsville, Ala., on the night of January 6, 1972, with the mean winter twilight 6300 Å intensities over the Blue Hill Observatory, Mass., during the 1968-1970 time period. During the early portion of the twilight period, the Blue Hill Observatory intensities are about 50 percent greater than those over Huntsville. During the latter part of the twilight period, the difference between the two sets of intensity observations increases to a factor of 3.5 to 4. Figure 46 provides a partial explanation for this difference in observed intensities in that the mean winter time densities at the F_2 peak over Blue Hill for the 1968-1970 time period are between 1.5 and 2.5 times as large as those over Huntsville on January 6, 1972.

VIII. CONCLUSIONS

A. Atmospheric Model

The results of this analysis indicate that the Jacchia 1971 model atmosphere is more representative of the molecular oxygen and nitrogen concentrations over Huntsville, Ala., on the night of January 6, 1972, than other existing

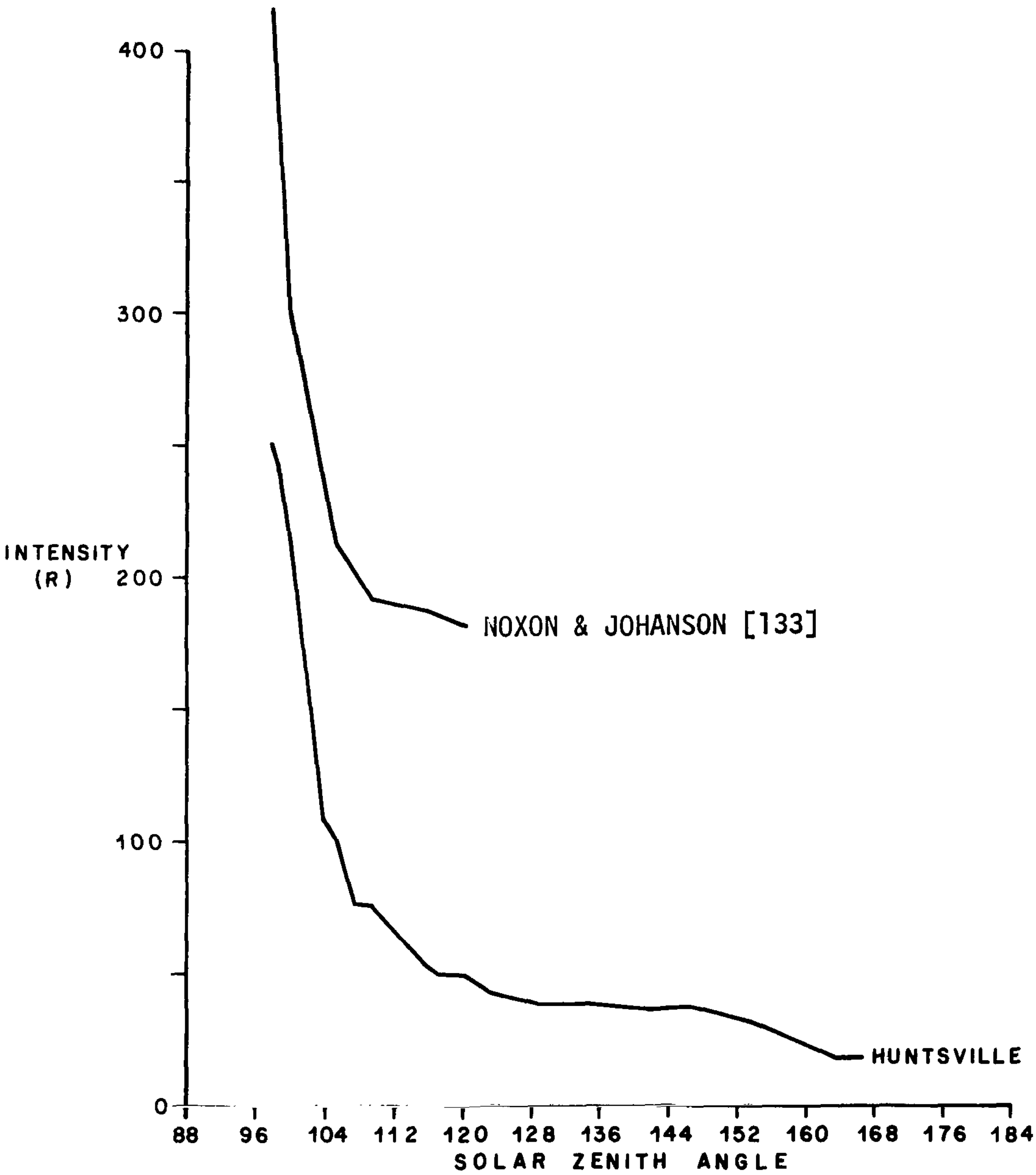

Figure 45. Comparison of 6300 Å emission intensities over Huntsville, Ala., and Blue Hill Observatory, Mass., as a function of solar zenith angle.

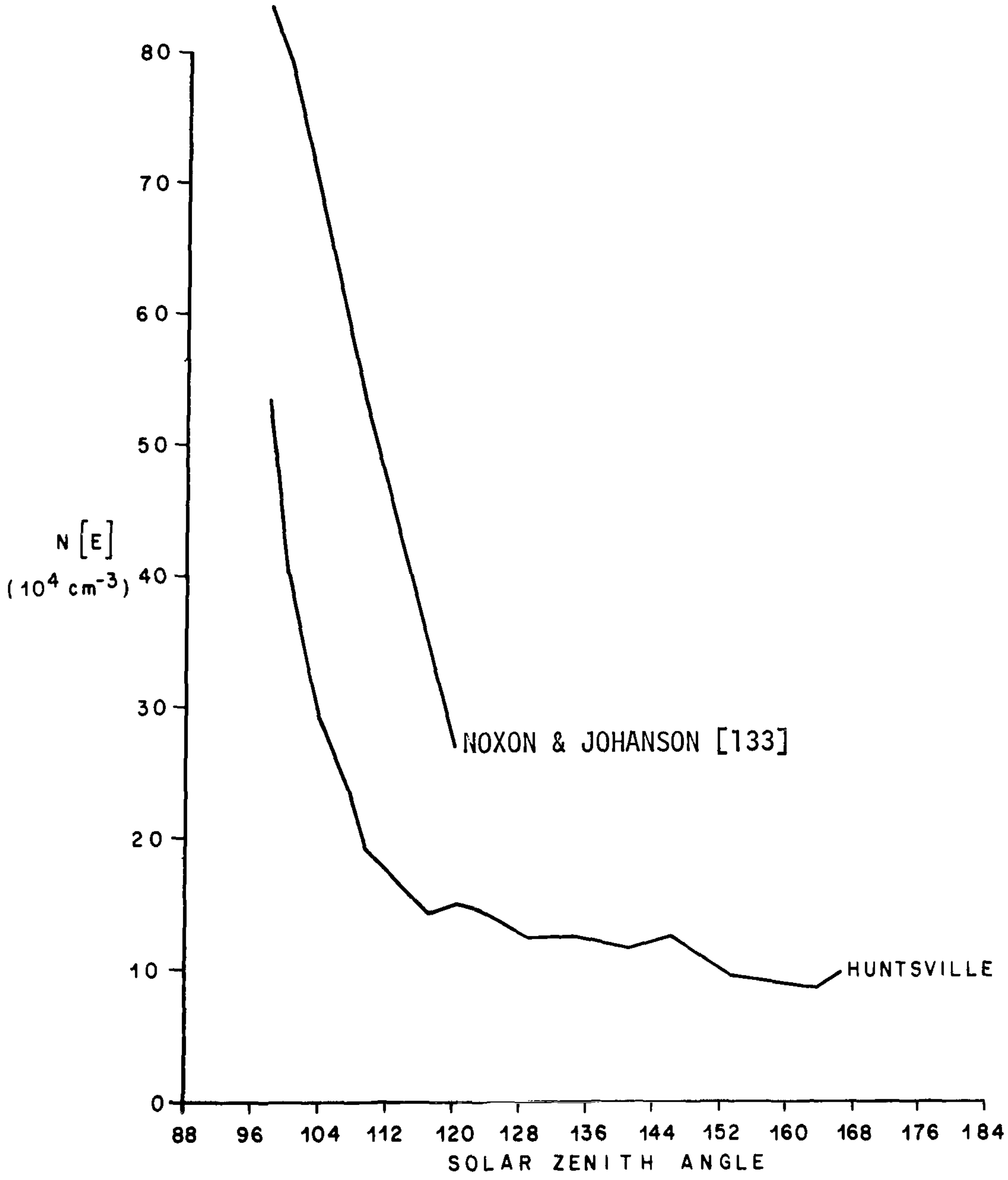

Figure 46. Comparison of F_2 peak electron number densities over Huntsville, Ala., and Blue Hill Observatory, Mass.

models. All other models require either dissociative recombination production mechanism efficiencies lower than the currently preferred value of 0.50 or rate coefficients for the quenching of $O(^1D)$ by molecular nitrogen higher than the highest value currently accepted by the scientific community, 1×10^{-10} cm^3 s^{-1}. The imposition of these limits on theoretical calculations of the 6300 Å emission shows that the Jacchia 1971 model consists of a lower limit on the molecular nitrogen number density and an upper limit on the molecular oxygen number density. Current planned revisions to the Jacchia 1971 model atmosphere include an increase in the molecular nitrogen number density and a decrease in the molecular oxygen density. These changes could readily be accommodated within the rate coefficient limits discussed above.

The 6300 Å emission can provide data concerning the N_2 and O_2 densities for use in the refinement and development of atmospheric models; however, additional emission lines must be monitored simultaneously to obtain the data required for the future refinement of the models at orbital altitudes where the principal constituent is atomic oxygen.

B. Photochemical Rate Coefficients

Results show that the following values constitute an internally consistent set that is capable of describing the post-sunset twilight behavior of the 6300 Å emission intensity:

$O^+ + O_2 \rightarrow O_2^+ + O$	2×10^{-11} cm^3 s^{-1}
$O_2^+ + e \rightarrow O^* + O$	1.95×10^{-7} $(300/T)^{0.7}$ cm^3 s^{-1} with an efficiency of producing $O(^1D)$ atoms of $0.50^{+0.32}_{-0.12}$
$O^+ + N_2 \rightarrow NO^+ + N$	1×10^{-12} cm^3 s^{-1}
$NO^+ + e \rightarrow N + O^*$	4.5×10^{-7} $(300/T)$ cm^3 s^{-1} with an efficiency of producing $O(^1D)$ atoms of 0.00
$O(^1D) + O_2 \rightarrow O + O_2$	5×10^{-11} cm^3 s^{-1}
$O(^1D) + N_2 \rightarrow O + N_2$	$\left(1^{+0.00}_{-0.11}\right) \times 10^{-10}$ cm^3 s^{-1}

The first three of these are upper limits since use of larger values would require that the upper limit on the N_2 quenching rate coefficient be exceeded or the dissociative recombination mechanism efficiency be less than 0.50, while the last two values are those currently most acceptable.

C. Solar Flux and Absorption Cross Sections

The conclusions reached above rule out the possibility of the Friedman and Tousey solar flux data as reported by Hinteregger et al. [6] as being representative of the solar conditions over Huntsville, Ala., on January 6, 1972, if the data are to be used in combination with the Metzger and Cook [7] absorption cross sections. The Ackerman [5] recommended solar fluxes and absorption cross sections are acceptable; however, additional observational data, such as fluxes and energy spectra of conjugate point photoelectrons, are required to positively establish the exact combination of solar flux and absorption cross section at any single point in time. For example, the Schumann-Runge contribution at 1726 CST could be increased from 67 R to 109 R and the agreement between the observed and calculated intensities would be perfect without the requirement for a large conjugate point photoelectron contribution. Therefore, although the Schumann-Runge fluxes and associated absorption cross sections listed in Table 14 are acceptable, an upper limit could be established as that combination of fluxes and absorption cross sections which would produce 109 R of 6300 Å OI intensity at 1726 CST. However, at 1726 CST the F_2 maximum electron density is decreasing rapidly with time and it is reasonable to assume that at least a comparable rate of decrease existed between sunset at 1703 CST and 1726 CST. Therefore, it is believed that this upper limit would not be realistic, since it appears that its use at smaller solar zenith angles would result in the calculated intensities becoming larger than the observed intensities.

Since no observational data are available prior to a local solar zenith angle of 97.5°, this analysis cannot provide any additional information about the conclusion of Noxon and Johanson [133] that the local photoelectron direct impact excitation process must be included for solar zenith angles between 90° and 95°, since the dissociative photoexcitation process alone cannot account for the difference between observed intensities and those calculated from the dissociative recombination process alone. In the winter the effects of CP photoelectrons further complicate the analysis.

D. Conjugate Point Photoelectrons

There is a sizeable contribution to the 6300 Å emission line intensity from conjugate point photoelectrons, at least during the period from a local solar zenith angle of approximately 97.5° to a conjugate point solar zenith angle of approximately 103°. These limits are set in this analysis by the earliest observation time and conjugate point sunset, assuming a screening height of 180 km. Based on the calculations in this analysis, the contribution of the combined dissociative recombination and conjugate point photoelectron direct impact excitation processes to the 6300 Å emission line intensity was approximately 183 R during the period from a local solar zenith angle of approximately 97.5° to a local solar zenith angle of approximately 103°. If these observations and calculations can be extrapolated to earlier times in the twilight period, perhaps the results imply that conjugate point photoelectrons do not contribute to the 6300 Å intensity as long as the local thermal electron densities are capable of producing 183 R through the dissociative recombination process.

E. Atmospheric Motions

Variations in the heights of the F_2 peak in the ionosphere were not associated with variations in the observed intensity; however, they were highly correlated with variations in the temperature derived from the Doppler broadening of the 6300 Å emission line. This implies that both the neutral and charged particle atmospheres were moving together and that observations of intensity enhancement by other investigators were more probably associated either with movements of the ionosphere that were not in phase with the neutral atmospheric movement or with travelling patches with increased electron densities.

Even though the variations in the temperature observations were highly correlated with the height of the F_2 peak, the magnitudes of the variations are such that the changes cannot be accounted for solely on the basis of observing another altitude region in a quiescent atmosphere. Changes of 20 to 40 km in the altitude of the F_2 peak are associated with temperature changes on the order of 100°K. At the heights at which these observations apply, temperature-height profiles in current models are nearly isothermal and changes of 10°to 50°K would be expected over these height intervals. Therefore, either the temperature-height profiles in the models are in error or the observations are being made at different altitudes in air masses with different exospheric temperatures. Wind measurements from the Doppler shift of the 6300 Å emission line could be used to determine whether these temperature variations should be attributed to vertical and/or horizontal motions or to differences between the true and the model temperature-height profiles. No detailed measurements of the variations in the outside pressure, the reference pressure for the etalon chamber, are available for the time period being analyzed; therefore, no data are available that can be used to derive vertical wind speeds which might provide some insight into this problem.

F. General

The total 6300 Å emission intensity over Huntsville, Ala., appears to be much lower than that reported by other investigators [133, 142, 17]; however, the conjugate point photoelectron contribution appears to be much larger during this declining portion of the 20th solar cycle. The lower integrated intensity over Huntsville can be attributed to the lower overall electron densities over Huntsville due to (1) its geographic location with respect to the geomagnetic equator which places it in an area of relatively low electron densities, (2) the fact that this analysis covered a twilight period in January when the annual variation would predict a minimum in the electron density, and (3) a time with respect to the solar cycle when the electron densities would be expected to be generally lower than those present for the time periods covered in the analyses referenced above. All of these factors would contribute to the increased CP photoelectron contribution observed over Huntsville if the local ionosphere controls the CP photoelectron input.

IX. RECOMMENDATIONS FOR FUTURE RESEARCH

The 6300 Å emission line intensity and line shape are excellent tools for studying the Earth's upper atmosphere, its composition, temperature, and dynamics; however, results are extremely sensitive to the electron density-height profiles used in the theoretical calculations required to substantiate and interpret the observational data. The phase path sounder at Huntsville, Ala., which is currently being modified, will soon be operational and capable of producing electron density-true height profiles with an accuracy of ±0.1 km.

The increased accuracy of these data will allow a better determination of molecular oxygen and nitrogen density-height profiles, if independent experiments such as the Ionospheric Modification Experiment can provide reliable results for the molecular nitrogen and/or oxygen quenching rate coefficients. Therefore, as soon as this sounder is available, the study should be reaccomplished to confirm these results.

The phase path sounder and a CW Doppler array currently being installed will be capable of providing additional data concerning the horizontal and vertical motions of the ionosphere. The etalon chamber pressure should be referenced to a baratron so that line of sight motions of the $O(^1D)$ atoms could be measured. The motions of both the charged particles and the $O(^1D)$ atoms could then be used in conjunction with changes in the 6300 Å emission intensity and the temperature of the neutral gas to study the effects of these motions on the emission intensity and the neutral gas temperature.

Observational data for other periods should be subjected to this same analysis to ascertain the magnitude of the CP contribution as well as any possible seasonal variations in onset time and/or magnitude. Seasonal variations due to changes in electron densities should also be studied in conjunction with the observed variations in the emission line intensity.

In view of the recent results of Hernandez[4] concerning the possible contamination of 6300 Å OI emission observations by the (9-3) hydroxyl band, extreme care should be taken to ensure that the data used in any analysis consist solely of 6300 Å photons from the atomic oxygen transition. Depending on its position with respect to the 6300 Å OI line shape profile, the (9-3) OH band emission can produce changes that imply:

1. Either lower or higher than actual temperatures for the ^1D oxygen atoms.

2. More or less than actual atomic oxygen red line emission intensity.

3. Mass motions of the ^1D oxygen atoms either toward or away from the observer.

The results of Sivjee [144] are quite significant with respect to the 6300 Å OI emission intensities and derived exospheric temperatures obtained with the Fabry-Perot interferometer in its present configuration. The low and rapidly fluctuating temperatures derived from the emission line profiles on other nights might be due to changes in the intensity and temperature of the 9-3 band OH emission (see Appendix D). The F-P configuration should be

---

[4] Hernandez, op. cit.

changed so that emission lines of this band system do not fall at the peak of the 6300 Å OI emission line profile. In addition, other measurements, perhaps with photometers containing filters that would provide data on the $P_1(3)$ line of the 9-3 OH band, should be made simultaneously so that the OH emission could be separated from the 6300 Å OI emission. This combination of observational data could then be used to study the dynamics of the D-region of the atmosphere. This might resolve questions concerning the origin of the low temperatures occasionally derived from 6300 Å OI emission line profiles.

APPENDIX A

HISTORICAL BACKGROUND

Newcomb [145] attributed the light of the night sky to the flux of radiation from stars that were too faint to be seen individually. Atmospheric light was studied intensively at the Lowell Observatory, Flagstaff, Arizona, from 1915 onward, and the two atomic oxygen redlines, 6300 and 6364 Å, were discovered there [146, 147]. Seasonal, day-to-day, and daily variations of the airglow were gradually discovered [148-152]. Chapman [139] first proposed the theory that the airglow was caused by emission of photons associated with the recombination of ionized and, more particularly, dissociated particles produced by the absorption of sunlight, in the ultraviolet portion of the spectrum, during the day. Dufay [153] showed that the luminance of the night sky must come from a combination of the zodiacal light and the self-luminescence of the atmosphere, not from faint stars.

Excitement of the 6300 and 6364 Å atomic oxygen lines during twilight was first discovered by Garrigue [154, 155]. His investigations showed that after twilight the 6300 Å emission diminished in intensity from 70 to 5 (arbitrary units) at sunset at approximately 10° above the horizon and from 20 to 5 in the north at the same elevation angle. He concluded that the radiation was emitted by excitation resulting from solar radiation because of the progressive decrease after twilight.

Cabannes and Garrigue [156] and Currie and Edwards [157] were the first to document and discuss the post-twilight decrease in the intensity of the 6300 Å emission. Their analysis of observations in December 1935 and January 1936 at Pic du Midi and the spring of 1936 at Montpelier showed that the 6300 Å emission intensity was affected by rapid perturbations, that it came from an altitude between 105 to 110 km, and that approximately 3 h after sunset it reached and thereafter remained fixed at a value approximately one-tenth the value at twilight with the intensity at the zenith two to three times weaker than at the horizon. These phenomena could not be explained by the action of sunlight even though they originated in the same atmospheric layers. The first explanations of the variation in intensity with the time based on the resonance scattering of sunlight were untenable; however, the photochemical dissociation of molecular oxygen by ultraviolet ($\lambda < 1750$ Å) could not be truly effective at very high altitudes in view of the rarity of molecular oxygen [158] and the slow decrease after sunset required the presence of a very large number of oxygen atoms at very great heights, a very large scale height.

The spectrographic studies of Elvey and Farnsworth [159] and Elvey [160] showed that the slow decrease of the intensity of the 6300 Å emission extended well into the night. The studies of Elvey and Farnsworth [159] also placed the height of the emitting layer at approximately 500 km with the twilight enhancement due to illumination of the atmosphere by the Sun, as postulated by Cabannes and Garrigue [156]. However, they also concluded that this effect could not account for all of the enhancement since it lasted for approximately 4 h after sundown. Resonance seemed unlikely because the emission was from a forbidden transition. Their study showed a difference between the morning and evening twilights; therefore, they concluded that the enhancement was due to some phenomenon of the upper atmosphere independent of the direct illumination of the Sun. From their pre-dawn enhancement analysis they concluded that there was a much slower decrease in the number of oxygen atoms with height than previous theoretical calculations had indicated. A gradual increase in intensity long before sunrise was also discovered at this time.

Bates [161] postulated that the 6300 Å emission originated in the F-region of the ionosphere and suggested that dissociative recombination of ions and electrons could be the source. Dufay and Tcheng Mao-Lin [162] confirmed both of these post- and pre-twilight enhancements that were investigated in more detail photoelectrically by Barbier [163] and photographically by Berthier [164] and Robley [165]. Berthier's [164] observations showed a very marked assymmetry between the morning and evening twilights. In the evening there was a very rapid decrease until the Sun was approximately 14° below the horizon and then a much slower decrease. According to his analysis the peak of the intensity occurred at an altitude between 90 and 100 km.

It had seemed quite likely [166] that a large part of the twilight 6300 Å emission arose from resonance scattering of sunlight; however, Chamberlain [15] showed that a comparison of observations with theory suggested that virtually none of the emission came from resonance scattering, a conclusion reached by Elvey and Farnsworth almost 15 years earlier. Chamberlain also showed that dissociation of molecular oxygen in the Schumann-Runge continuum contributed, but did not give by itself, either the observed intensity or its variations with time. He then advanced the hypothesis that the main excitation of the 6300 Å twilight emission arose from dissociative recombination of O_2^+ following suggestions of Bates and Massey [61], Bates [166], and Barbier [167]; however, he assumed that molecular oxygen was the principal deactivating particle. His study supported the results of Dufay and Tcheng Mao-Lin [168] and Barbier [14] that the emission height was approximately 250 to 300 km.

The rocket results of Heppner, Stolarik, and Meredith [169] and Heppner and Meredith [170] placed the emission height above 163 km, while the results of Zipf and Heath [171] raised the emission height to above 208 km. The rocket-borne measurements of Gulledge and Packer [172] and the satellite measurements of Reed and Blamont [173] gave further evidence that the maximum of the 6300 Å emission is at an altitude of approximately 250 to 300 km with the emitting layer on the order of 80 to 100 km thick.

The ionospheric analyses of Ratcliffe, Schmerling, Setty, and Thomas [174] and Bates [175, 176] presented further evidence of the importance of dissociative recombination. St. Amand [177] and Barbier [167] showed a connection between the F-layer and the redlines. Huruhata, Nakamura, Tanabe, and Tohmatsu [178] concluded from their analysis of rocket-borne measurements that the 6300 Å emission was approximately proportional to the maximum electron density in the F-region of the ionosphere. The dissociative recombination theory was further advanced and developed by Lagos, Bellew, and Silverman [179], Peterson, Van Zandt, and Norton [116], Holmes, Johnson, and Young [180], Zipf [28], Wallace and McElroy [12], Ferguson, Fehsenfeld, Goldan, Schmeltekopf [80], Swider [27], and Okuda [181, 182].

Brandt [9] predicted that the 6300 Å emission in the day glow would be approximately 50 kR, and Noxon and Goody [183] and Jarrett and Hoey [132] obtained similar values. However, Zipf and Fastie [46], Wallace and Nidey [184], and Nagata, Tohmatsu, and Ogawa [185] got values of approximately 5 kR. Noxon [10] reported observed values ranging from 5 to 50 kR with very large day-to-day variations.

The first reported redline altitude intensity distribution from rocket-borne measurements was by Gulledge and Packer [186] followed by Huruhata, Nakamura, and Tanabe [187] and Wallace and McElroy [12]. The zenith intensity during the 1964 rocket flight reported on by Gulledge and Packer was approximately 22 R with no emission above 300 km with an intensity greater than 5 R. This result was consistent with the dissociative recombination theory in which the emitting layer moved upward during the night. The results of Huruhata, Nakamura, and Tanabe [187] were similar with an integrated intensity of less than 25 R and an emission layer from 200 to 320 km, peaking at an altitude between 270 and 280 km. Gulledge, Packer, Tilford, and Vanderslice [50] reported on the results of another rocket-borne measurement which showed that approximately 5 h after sunset the peak emission occurred at 246 km. The zenith intensity on the upleg was approximately 70 R, while the downleg intensity was approximately 90 R. The difference was attributed to an observed downward motion of the ionosphere, thereby lending more credence to the correlation between the redline emission and the ionosphere.

Eather [188] reported that the average night glow 6300 Å emission was approximately 35 R north of 80° invariant latitude, then decreased to as low as 5 R between 40 and 55° invariant latitude, and then increased to 30 R in the 15 to 25° latitude region. These results were obtained from a tilting photometer flown on a Convair 990. The photometer system included a C^{14} radioactive light source that had been calibrated at Fritz Peak Observatory by M. Gadsden.

Schaeffer, Feldman, and Fastie [112], based on the results of an analysis of a rocket flight at a solar zenith angle of 60°, reported that the measured 6300 Å emission above 100 km was approximately 1.1 kR with 0.29 kR due to photodissociation, 0.56 kR due to direct electron impact excitation, and 0.26 kR due to dissociative recombination. They did not claim high accuracy for their electron impact results but believed the photodissociation production rate was approximately equal to one-third of that expected from the solar flux values of Detwiler, Garrett, Purcell, and Tousey [189]. However, their results were in good agreement with the solar flux values of Parkinson and Reeves [190].

Brasher and Hanson [191] have provided further evidence of the connection between the ionosphere and the redline emission. They showed theoretically that a lifting of the F_2 peak by only 20 km reduced the peak night glow intensity by a factor of approximately three and in so doing confirmed the suggestion by Van Zandt and Peterson [192] that there is a correlation between the midnight enhancement of the 6300 Å emission and the ionospheric drifts.

APPENDIX B

LISTING OF COMPUTER PROGRAM OF THEORETICAL MODEL

```
      DIMENSION FRF(3)
      DIMENSION ZFLUX(91),COLUMN(3,39),Z(39),E(39),XZ(7),CH(3)
      COMMON TAU(3),TEMPOZ(4),FLUX(45),SIGABS(3,45),ATMC1,ATMC2,ATMC3,AT
     1MA,ATMS,ATMGAM(3),CON120(3),E,EMISSS(500),INTEGS(500),DELZ,F,J,
     2TINF,CAAFO,ALATH,CAGNI,ALPTH,CAOA,CAOC,HZ(3),O1D,O2D,O3D,O2
C       PROGRAM FOR THE CALCULATION OF 6300A AIRGLOW AT SPECIFIED ALTITUDES.
      IN=5
      IO=6
      IP=7
  200 FORMAT(F5.0,F6.1,3E8.1,I4)
  201 FORMAT(3E16.8)
  202 FORMAT(E15.8,15X,3E15.8)
  203 FORMAT(13E5.2)
  204 FORMAT(6E10.2)
  205 FORMAT(12I5)
   90 FORMAT(11H INPUT DATA/49H        TINF,T120,CON120(1),CON120(2),CON1
     120(3), = /2(F10.3,1H,),3(E15.8,1H,))
  990 FORMAT(29H        YEAR,DD,HR,MN,THETA = /1X,4F7.1,F9.2)
  506 FORMAT(F6.1,3F5.1)
C      NUMBER DENSITIES                    TEMPOZ(1)-TEMPOZ(4)
C      **********  DEFINITION OF CONSTITUENTS  **********
C                          I     TEMPOZ(I)
C                          1       N2
C                          2       O2
C                          3       O
C                          4       O2
C               READ THE INPUT PARAMETERS
      DO 17 L=1,45
   17 READ(IN,202)ZFLUX(L),SIGABS(3,L),SIGABS(2,L),SIGABS(1,L)
      READ(IN,504)
      READ (IN,201) CON120(1), CON120(2), CON120(3)
      READ(IN,200)YEAR,T120,ZMAX,ZMIN,DELZ,LMAX
 1000 READ(IN,506)TINF,DD,HR,MN
      READ(IN,203)(E(J),J=1,39)
      WRITE(IO,90)TINF,T120,CON120(1),CON120(2),CON120(3)
      TPI=6.28318536
      XCON=57.29577951
      EPS=23.45/XCON
C      FLONG IS LONGITUDE OF HUNTSVILLE
      FLONG=-86.65
      PIT=1.57079634
      PI=3.14159268
      CALL ANGLE(HR,YEAR,DD,MN,XCON,EPS,TPI,FLONG,THETA)
      WRITE(IO,990)YEAR,DD,HR,MN,THETA
      DO 18 I=1,3
   18 COLUMN(I,1)=0.0
   85 CONTINUE
C THE INITIAL VALUES OF THE ARRAYS - FLUX[L],COLUMN[I,J], AND PREV[I]
C      ARE NOW ESTABLISHED
C        THESE PARAMETERS ARE CALCULATED ONLY ONCE AND THOSE WITH THE
C  PREFIX - ATM - ARE USED IN THE SUBROUTINE MODATM, AND ARE SPECIFIED
C  IN COMMON
      D=TINF-800.0
      ARG=D/(750.0+1.722E-4*D**2)
      ATMS=1.5E-4+0.0291*EXP(-.5*ARG**2)
      ATMA=(TINF-T120)/TINF
```

```
C  ATMC1 AND ATMC3 ARE IN CENTIMETERS. WHILE ATMC2 IS IN KILOMETERS
      ATMC1=120.0E5
      ATMC2=6476.77
      ATMC3=6356.77E5
      ATMGAM(1)=(1.1359*29.0)/(ATMS*TINF)
      ATMGAM(2)=ATMGAM(1)*(32.0/28.0)
      ATMGAM(3)=ATMGAM(2)*.5
      J=1
      Z(J)=ZMAX
      ZZ=Z(J)
      THETA=THETA/XCON
      CALL JAC(ZZ)
      CAOC=9.0E-11
      CAOA=5.0E-11
      CABNI=2.0E-12
      CAAFO=4.0E-11
      ALBTH=5.0E-07
      ALATH=1.9E-07
      DO 5445 I=1,3
      XZ(I)=(ATMC3+ZZ)/(HZ(I)*1.E5)
 5445 TAU(I)=SQRT(.5*XZ(I)*(COS(THETA)*COS(THETA)))
      CALL ERFS(ERF)
      IF(PIT-THETA)533,533,535
  533 DO 599 I=1,3
  599 CH(I)=(SQRT(PIT*XZ(I)*SIN(THETA)))*EXP(TAU(I)*TAU(I))*(1.+ERF(I))
      GO TO 566
  535 DO 606 I=1,3
  606 CH(I)=(SQRT(PIT*XZ(I)*SIN(THETA)))*EXP(TAU(I)*TAU(I))*(1.-ERF(I))
  566 DO 577 I=1,3
  577 COLUMN(I,J)=TEMPOZ(I)*HZ(I)*CH(I)*1.E5
      DO 66 L=1,45
      FLUX(L)=0.0
      DO 3333 I=1,3
 3333 FLUX(L)=FLUX(L)+SIGABS(I,L)*COLUMN(I,J)
      FLUX(L)=ZFLUX(L)*EXP(-FLUX(L))
   66 CONTINUE
      CALL CONSTI
      CALL EMISS
      INTEGS(J)=EMISSS(J)
      WRITE(IO,108)ZZ,(TEMPOZ(I),I=1,4),EMISSS(J),E(J),INTEGS(J),
     1010,020,030,0P
      DO7J=2,500
      Z(J) =  Z(J-1) - DELZ
      IF(Z(J).LT.ZMIN)GO TO 21
      ZZ=Z(J)
      CALL JAC(ZZ)
      DO 54 I=1,3
      XZ(I)=(ATMC3+ZZ)/(HZ(I)*1.E5)
   54 TAU(I)=SQRT(.5*XZ(I)*(COS(THETA))**2)
      CALL ERFS(ERF)
      IF(PIT-THETA)53,53,55
   53 DO 59 I=1,3
   59 CH(I)=(SQRT(PIT*XZ(I)*SIN(THETA)))*EXP(TAU(I)*TAU(I))*(1.+ERF(I))
      GO TO 56
   55 DO 60 I=1,3
   60 CH(I)=(SQRT(PIT*XZ(I)*SIN(THETA)))*EXP(TAU(I)*TAU(I))*(1.-ERF(I))
```

```
      56 DO 57 I=1,3
      57 COLUMN(I,J)=TEMPOZ(I)*H2(I)*CH(I)*1.E5
      58 DO 5 L=1,45
         FLUX(L)=0.
         DO 3033 I=1,3
    3033 FLUX(L)=FLUX(L)+SIGABS(I,L)*COLUMN(I,J)
         FLUX(L)=7FLUX(L)*EXP(-FLUX(L))
       5 CONTINUE
         CALL CONSTI
         CALL EMISS
         CALL INTEG
         WRITE(IO,108)ZZ,(TEMPOZ(I),I=1,4),EMISSS(J),E(J),INTEGS(J),
        1O1D,O2D,O3D,OP
       7 CONTINUE
         WRITE(IO,103)
         GO TO 22
      21 WRITE(IO,104)
      22 GOTO 1000
     100 FORMAT(1X1H16HHEIGHT2XF10.3,1X3HKM.)
     103 FORMAT(10X35HLOWER BOUNDARY HAS NOT BEEN REACHED)
     104 FORMAT(10X32HNORMAL COMPLETION OF COMPUTATION)
     106 FORMAT(/5X,2HL=,I3,5X2HI=,I2,5X2HS=,I2,5X10HDATA ERROR)
     108 FORMAT(1X,5HZZ = E20.8/1X16HNUMBER DENSITIES/1X,2HN2,1XE11.3,2X,2H
        1O2,1XE11.3,2X,1HO,1XE11.3,2X,2HO3,1XE11.3/1X,5HEMISS,1XE11.3,2X,
        21HE,1XE11.3,2X,6HINTEGS,1XE11.3/1X,3HO1D,1XE11.3,2X,3HO2D,1XE11.3,
        32X,3HO3D,1XE11.3,2X,2HOP,1XE11.3//)
     500 FORMAT(72H
        1                         )
         END

D OF COMPILATION:          NO  DIAGNOSTICS.


         SUBROUTINE JAC(ZZ)
         REAL INTEGS
         DIMENSION E(39)
         DIMENSION ALPHA(5),EI(6),DI(6),R(7),DII(6),XM(3)
         COMMON TAU(3),TEMPOZ(4),FLUX(45),SIGABS(3,45),ATMC1,ATMC2,ATMC3,AT
```

```
     1MA,ATMS,ATMGAM(3),CON120(3),E,EMISSS(500),INTEGS(500),DELZ,F,J,
     2TINF,CAAFO,ALATH,CABNI,ALBTH,CADA,CAOC,HZ(3),D1D,D2D,D7D,CP
      T90=193.
      Z=ZZ*1.0E-5
      GRAV=9.80665E-3*(1.+ZZ/ATMC3)**-2.
      ALPHA(4)=0.0
      ALPHA(3)=0.0
      ALPHA(2)=0.0
      ALPHA(1)=0.0
      XM(3)=16.
      XM(2)=32.0
      XM(1)=28.0
      BOLTZ=8.31432E-3/GRAV
      T=TINF
      RHO90=.346E-9
      ALPHA(5)=-.38
      ALPHA(6)=0.0
      AV=6.02257E23
      EI(1)=28.0134
      EI(2)=31.9988
      EI(3)=15.9994
      EI(4)=39.948
      EI(5)=4.0026
      EI(6)=1.00797
      B(1)=28.82579
      B(2)=-.0740066
      B(3)=-.011940 7
      B(4)=4.51103E-4
      B(5)=-8.21895E-6
      B(6)=1.07561E-5
      B(7)=-6.97444E-7
      QN=.78110
      QO2=.20955
      QA=.0093432
      QHE=6.1471E-6
      RK=8.31432
      TX=371.6678+.0518806   *T-294.3505 *EXP(-.00216222*T)
      A2=2.*(T-TX)/3.14159265
      DIT(6)=0.
      M=10
      EPS=.0001
      T1=1.9*(TX-T90     )/35.
      T4=3.*(TX-T90     -2.*T1*35./3.)/(35.**4)
      T3=-T1/(3.*35.**2)+4.*T4*35./3.
      TZ=TX+T1*(Z-125.)+T3*(Z-125.)**3+T4*(Z-125.)**4
      IF (Z-100.) 43,43,40
   43 ZZ=Z-90.
      EM=B(1)+B(2)*ZZ+B(3)*ZZ**2+B(4)*ZZ**3+B(5)*ZZ**4+B(6)*ZZ**5
     1+B(7)*ZZ**6
      D=Z
 70   CONTINUE
      A=90.
      FA=B(1)+B(2)*(A-90)+B(3)*(A-90)**2+B(4)*(A-90)**3+B(5)*(A-90)**4
     1+B(6)*(A-90)**5 +B(7)*(A-90)**6
      FA=FA*9.80665/((1.+A/6.356766E+3)**2)
      FA=FA/(TX+T1*(A-125.)+T3*(A-125.)**3 +T4*(A-125.)**4)
```

```
      FD=B(1)+B(2)*(D-90)+B(3)*(D-90)**2+B(4)*(D-90)**3+B(5)*(D-90)**4
     1+B(6)*(D-90)**5 +B(7)*(D-90)**6
      FD=FD*9.80665/((1.+D/6.356766E+3)**2)
      FD=FD/(TX+T1*(D-125.)+T3*(D-125.)**3 +T4*(D-125.)**4)
C     SR04, SIMPSONS RULE QUADRATURE  -  S.F.KUNCIR                   SR040
C     DEFINITIONS  -                                                  SR040
C        A = LOWER LIMIT OF INTEGRATION                               SR040
C        D = UPPER LIMIT OF INTEGRATION
C        FUNC = INTEGRAND FUNCTION SUBPROGRAM                         SR040
C        EPS = RELATIVE ERROR CONVERGENCE CRITERION                   SR040
C        R = RESULT OF INTEGRATION                                    SR040
C        N = NUMBER OF INTEGRATIONS REQUIRED TO FIND R.               SR040
C                                                                     SR040
      N=0                                                             SR040
      PREV=0.                                                         SR040
      SONE=(D-A)*(FA+FD)/2.
   71 N=N+1
      IF (N-M) 72,72,75
   72 NINT=2**N
      STWO=0.                                                         SR040
      DEL=(D-A)/FLOAT(NINT)
      DO 73 I=1,NINT,2
      X=A+DEL*FLOAT(I)                                                SR040
      FX=B(1)+B(2)*(X-90)+B(3)*(X-90)**2+B(4)*(X-90)**3+B(5)*(X-90)**4
     1+B(6)*(X-90)**5 +B(7)*(X-90)**6
      FX=FX*9.80665/((1.+X/6.356766E+3)**2)
      FX=FX/(TX+T1*(X-125.)+T3*(X-125.)**3 +T4*(X-125.)**4)
   73 STWO=STWO+FX
      CUR=SONE+4.*DEL*STWO                                            SR040
      IF (EPS*ABS(CUR)-ABS(CUR-PREV)) 74,75,75
   74 PREV=CUR
      SONE=(SONE+CUR)/4.                                              SR040
      GO TO 71
   75 R=CUR/3.
      IF (Z-100.) 44,75,44
   44 IF (D-100.) 76,55,76
   76 DENS=RHO90*T90*FM*EXP(-R/FK)/(TZ*28.82579)
      DL=XLOG(DENS)
      PAR=AV*DENS/FM
      AN=XLOG(QN*EM*PAR/28.96)
      AA=XLOG(QA*EM*PAR/28.96)
      AHE=XLOG(QHE*EM*PAR/28.96)
      AO=XLOG(2.*PAR*(1.-FM/28.96))
      AO2=XLOG(PAR*(FM*(1.+QO2)/28.96-1.))
      AH=-0.
      TEMPOZ(1)=AN
      TEMPOZ(2)=AO2
      TEMPOZ(3)=AO
      DO3331 I=1,3
 3331 HZ(I)=(BOLTZ*TZ)/XM(I)
      RETURN
   40 Z3=100.
      TZ3=TX+T1*(Z3-125.)+T3*(Z3-125)**3+T4*(Z3-125)**4
      ZM3=B(1)+B(2)*10.+B(3)*100.+B(4)*1000.+B(5)*10.**4.+B(6)*10.**5.
     1+B(7)*10.**6.
      D=100.
```

```
          GO TO 70
       55 DEN1=RHO90     *T90     *ZM3*EXP(-R/FK)/(T23*286.82E78 )
          PAR=AV*DEN1/ZM3
          DI(1)=QN*ZM3*PAR/28.96
          DI(2)=PAR*(ZM3*(1.+QO2)/28.96-1.)
          DI(3)=2.*PAR*(1.-ZM3/28.96)
          DI(4)=QA*ZM3*PAR/28.96
          DI(5)=QHE*ZM3*PAR/28.96
          IF(Z-125.) 56,56,90
    56    CONTINUE
          A1=100.
          FA1=9.80665/((1.+A1/6.356766E+3)**2)
          FA1=FA1/(TX+T1*(A1-125.)+T3*(A1-125.)**3+T4*(A1-125.)**4)
          D1=Z
          FD1=9.80665/((1.+D1/6.356766E+3)**2)
          IF(D1-125.) 45,45,50
       45 FD1=FD1/(TX+T1*(D1-125.)+T3*(D1-125.)**3+T4*(D1-125.)**4)
          GO TO 51
    50    FD1=FD1/(TX+A2*ATAN(T1*(D1-125.)*(1.+4.5E-6*(D1-125.)**2.5)/A2))
          TZ=TX+A2*ATAN(T1*(Z-125.)*(1.+4.5E-6*(Z-125.)**2.5)/A2)
    51    N=0
          PREV=0
          SONE=(D1-A1)*(FA1+FD1)/2.
    91    N=N+1
          IF (N-M) 92,92,85
    92    NINT=2**N
          STWO=0.
          DEL=(D1-A1)/FLOAT(NINT)
          DO 83 I=1,NINT,2
          X1=A1+DEL*FLOAT(I)
          FX1=9.80665/((1.+X1/6.356766E+3)**2)
          IF(X1-125.) 46,46,52
       46 FX1=FX1/(TX+T1*(X1-125.)+T3*(X1-125.)**3+T4*(X1-125.)**4)
          GO TO 83
    52    FX1=FX1/(TX+A2*ATAN(T1*(X1-125.)*(1.+4.5E-6*(X1-125.)**2.5)/A2))
    83    STWO=STWO+FX1
          CUR=SONE+4.*DEL*STWO
          IF (EPS*ABS(CUR)-ABS(CUR-PREV)) 84,85,85
    84    PREV=CUR
          SONE=(SONE+CUR)/4.
          GO TO 91
    85    R=CUR/3.
          DO 41  I=1,5
          DIT(I)=DI(I)*(T23/TZ)**(1.+ALPHA(I))*EXP(-FI(I)*R/FK)
       41 CONTINUE
          TEMPOZ(1)=DIT(1)
          TEMPOZ(2)=DIT(2)
          TEMPOZ(3)=DIT(3)
          DENS=0
          DO 42 I=1,6
          DENS=DENS+EI(I)*DIT(I)/AV
    42    CONTINUE
          EM=DENS*AV/(DIT(1)+DIT(2)+DIT(3)+DIT(4)+DIT(5)+DIT(5))
          DL=XLOG(DENS)
          AN =XLOG(DIT(1))
          AO2=XLOG(DIT(2))
```

```
            AO  =XLOG(DIT(3))
            AA  =XLOG(DIT(4))
            AHE=XLOG(DIT(5))
            IF(Z-500.) 47,48,48
         47 DIT(6)=10.**(-6)
         48 AH=XLOG(DIT(6))
            AN  =AMAX1(-0.,  AN)
            AO2=AMAX1(-0.,AO2)
            AO  =AMAX1(-0.,  AO)
            AA  =AMAX1(-0., AA)
            AHE=AMAX1(-0.,AHE)
            AH  =AMAX1(-0., AH)
            DO 3332 I=1,3
       3332 HZ(I)=(BOLTZ*TZ)/XM(I)
            RETURN
     90     S=TX+A2*ATAN(T1*375.*(1.+4.5E-5*375.**2.5)/A2)
            DI(6)=10.**(73.13-39.4*XLOG(S)+5.5*XLOG(S)*XLOG(S))
            A1=500.
            IF(Z-500.) 49,50,50
         49 A1=Z
         50 FA1=9.80665/((1.+A1/6.356766E+3)**2)
            FA1=FA1/(TX+A2*ATAN(T1*(A1-125.)*(1.+4.5E-6*(A1-125.)**2.5)/A2))
            D1=Z
            IF(Z-500.) 61,62,62
         61 D1=500.
         62 FD1=9.80665/((1.+D1/6.356766E+3)**2)
            FD1=FD1/(TX+A2*ATAN(T1*(D1-125.)*(1.+4.5E-6*(D1-125.)**2.5)/A2))
            N=0
            PREV=0
            SONE=(D1-A1)*(FA1+FD1)/2.
     91     N=N+1
            IF (N-M) 92,92,95
     92     NINT=2**N
            STWO=0.
            DEL=(D1-A1)/FLOAT(NINT)
            DO 93 I=1,NINT,2
            X1=A1+DEL*FLOAT(I)
            FX1=9.80665/((1.+X1/6.356766E+3)**2)
            FX1=FX1/(TX+A2*ATAN(T1*(X1-125.)*(1.+4.5E-6*(X1-125.)**2.5)/A2))
     93     STWO=STWO+FX1
            CUR=SONE+4.*DEL*STWO
            IF (EPS*ABS(CUR)-ABS(CUR-PREV)) 94,95,95
     94     PREV=CUR
            SONE=(SONE+CUR)/4.
            GO TO 91
     95     R=CUR/3.
            TZ=TX+A2*ATAN(T1*(Z-125.)*(1.+4.5E-6*(Z-125.)**2.5)/A2)
            IF(Z-500.) 63,64,64
         63 R=-R
         64 DIT(6)=DI(6)*(S/TZ)*EXP(-EI(6)*R/FK)
            GO TO 56
            END

D OF COMPILATION:          NO   DIAGNOSTICS.
```

```
      SUBROUTINE INTEG
      REAL INTEGS
      DIMENSION E(39)
      COMMON TAU(3),TEMPOT(4),FLUX(45),SIGABS(3,45),ATMC1,ATMC2,ATMC3,AT
     1MA,ATMS,ATMGAM(3),CON120(3),E,EMISSS(500),INTEGS(500),DELZ,F,J,
     2TINF,CAAFO,ALATH,CABNI,ALBTH,CADA,CAOC,HZ(3),D1D,D2D,D3D,DP
      JJ=J-1
      AEMISS=(EMISSS(JJ)+EMISSS(J))*.5
      COLEMI=AEMISS*DELZ
      INTEGS(J)=INTEGS(JJ)+COLEMI
      RETURN
      END

      SUBROUTINE  ANGLE(HR,YR,DAYNO,MIN,XCON,EPS,TPI,FLONG,THETA)
      REAL JD,MIN
      JD=2439856.+(YR-1969.)*365.+DAYNO
  170 TEMP=(JD-2415020.)/36525.
      TGO=99.6909833+TEMP*(36000.76854+3.8708E-04*TEMP)
  171 IF(TGO-360.)173,173,172
  172 TGO=TGO-360.
      GO TO 171
  173 GMT=HR*60.+MIN
  175 THG=TGO+GMT*.25068447
  176 IF(THG-360.)178,178,177
  177 THG=THG-360.
      GO TO 176
  178 ANG=THG+FLONG
  180 IF(ANG-360.)190,190,185
  185 ANG=ANG-360.
      GO TO 180
  190 ANG=ANG/XCON
      FLAMS=.017203*(JD-2435839.)+.0335*SIN(.017203*
     1(JD-2435839.))-1.41
      IF(FLAMS)195,191,191
  191 IF(FLAMS-TPI)198,198,192
  192 FLAMS=FLAMS-TPI
      GO TO 191
  195 IF(FLAMS+TPI)196,198,198
  196 FLAMS=FLAMS+TPI
      GO TO 195
  198 CONTINUE
      DLSUN=ASIN(SIN(EPS)*SIN(FLAMS))
      ALSUN=ASIN(TAN(DLSUN)/TAN(EPS))
C      PUT ALSUN AND FLAMS IN SAME QUAD.
      ALSUN=ABS(ALSUN)*XCON
      TEMP=ABS(FLAMS)*XCON
      IF(TEMP-90.)230,230,200
  200 IF(TEMP-180.)205,205,210
  205 ALSUN=180.-ALSUN
      GO TO 230
  210 IF(TEMP-270.)215,215,220
  215 ALSUN=ALSUN+180.
      GO TO 230
  220 ALSUN=360.-ALSUN
  230 IF(FLAMS)235,240,240
  235 ALSUN=-ALSUN
  240 ALSUN=ALSUN/XCON
      HSUN=ANG-ALSUN
      HRA=HSUN
      DS=DLSUN
      CTHETA=COS(34.6/XCON)*COS(DS)*COS(HRA)+SIN(34.6/XCON)*SIN(DS)
      THETA=ACOS(CTHETA)
      THETA=THETA*XCON
      RETURN
      END
```

```
      FUNCTION XLOG(X)
      XLOG=ALOG10(X)
      RETURN
      END

D OF  COMPILATION:          NO  DIAGNOSTICS.
```

```
      SUBROUTINE CONSTI
      REAL INTEGS
      DIMENSION E(39)
      COMMON TAU(3),TEMPOZ(4),FLUX(45),SIGABS(3,45),ATMC1,ATMC2,ATMC3,AT
     1MA,ATMS,ATMGAM(3),CON120(3),E,EMISSS(500),INTEGS(500),DELZ,F,J,
     2TINF,CAAFO,ALATH,CABNI,ALBTH,CAOA,CAOC,H7(3),O1D,O2D,O3D,OP
      Q=E(J)
      RR=0.30
      PR=0.15
      RRR=0.15
      R=1.0
      SUM1=0.0
      DO 51 L=1,45
      DISSOC=SIGABS(2,L)*FLUX(L)*TEMPOZ(2)
   51 SUM1=SUM1+DISSOC
      O1D=R*SUM1
      OP=( .95*Q**2.)/(Q*TEMPOZ(1)*CABNI/ALBTH+TEMPOZ(2)*CAAFO/ALATH)
      O2D=RR*CAAFO*TEMPOZ(2)*OP
      O3D=RRR*CABNI*TEMPOZ(1)*OP
      TEMPOZ(4)=O1D+O2D
      RETURN
      END

D OF  COMPILATION:          NO  DIAGNOSTICS.
```

```
      SUBROUTINE EMISS
      REAL INTEGS
      DIMENSION E(39)
      COMMON TAU(3),TEMPOZ(4),FLUX(45),SIGABS(3,45),ATMC1,ATMC2,ATMC3,AT
     1MA,ATMS,ATMGAM(3),CON120(3),E,EMISSS(500),INTEGS(500),DELZ,F,J,
     2TINF,CAAFO,ALATH,CABNI,ALBTH,CAOA,CAOC,H7(3),O1D,O2D,O3D,OP
      A=5.9E-9*TEMPOZ(4)
      EMISSS(J)=A/(9.1E-3+CAOC*TEMPOZ(1)+CAOA*TEMPOZ(2))
      RETURN
      END

D OF  COMPILATION:          NO  DIAGNOSTICS.
```

```
          SUBROUTINE ERFS(ERF)
          DIMENSION ERF(3)
          COMMON TAU(3)
          A1=.25482959
          A2=.28449674
          A3=1.4214137
          A4=-1.453152
          A5=1.0614054
          B=.3275911
          DO 1 I=1,3
          QS=1./(1.+B*TAU(I))
        1 ERF(I)=1.-((((A5*QS+A4)*QS+A3)*QS+A2)*QS+A1)*QS/EXP(TAU(I)*TAU(I))
          RETURN
          END

D OF COMPILATION:          NO  DIAGNOSTICS.
```

APPENDIX C

OBSERVATIONAL DATA

The airglow equipment was operated on approximately 15 nights during the period November 10, 1971, through September 1, 1972; however, equipment status, weather conditions, and the requirement for a moonless condition limited to 5 the number of nights on which observations were made simultaneously by the C-4 ionosonde, Fabry-Perot interferometer, and the turret photometer. The temperature histories of the nights of January 7, 1972, and February 7, 1972, both contain very low temperatures that may be due to contamination of the Fabry-Perot 6300 Å OI emission observations by OH emissions. This is discussed in more detail in Appendix D. Electron density-height profiles, required for a detailed analysis, were not available on the nights of November 17, 1971, and February 4, 1972, due to equipment malfunctions. The night of January 6, 1972, was selected for analysis because the records were somewhat more complete on that night; however, the data from the remaining four nights are provided here for comparison. The intensity time histories of all five are quite similar; however, the temperature histories of all five show large variations in short time periods with extremely low temperatures being observed near midnight on January 7, 1972. These temperatures are comparable to temperatures derived on other nights when observations were begun long after the sunset period; however, to date no explanation has been found.

Although the peak electron number density-time histories are similar, the actual number densities on January 6, 1972, are smaller than those observed on the other four nights.

It is believed that these data will support the contention that the data of January 6, 1972, are not atypical of the airglow measurements over Huntsville, Alabama, and, therefore, the conclusions reached on the basis of the analysis of this single night are truly representative of the majority of atmospheric conditions and not merely fortuitous.

Figures C-1 through C-7 present the observational data.

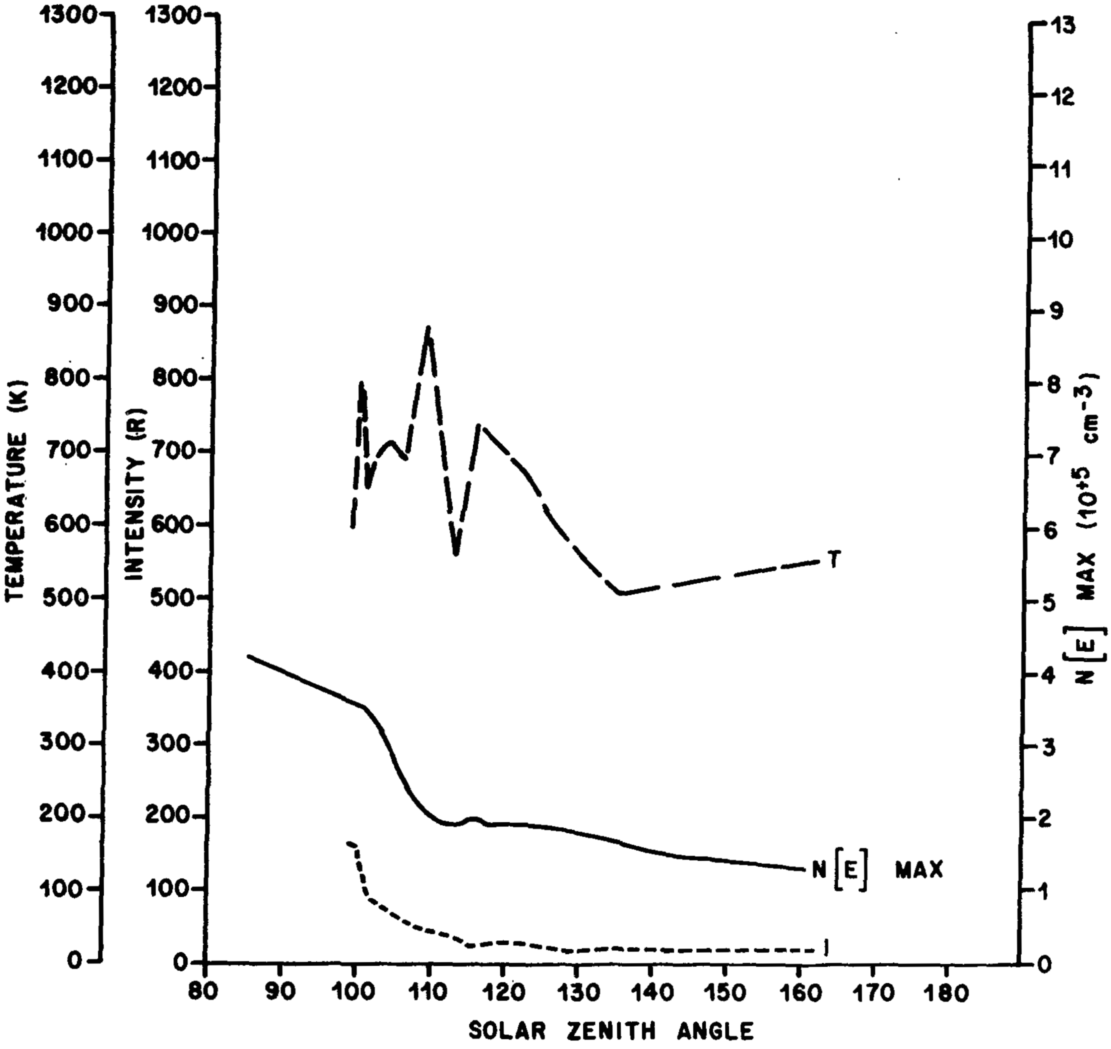

Figure C-1. Observational data for November 17, 1971.

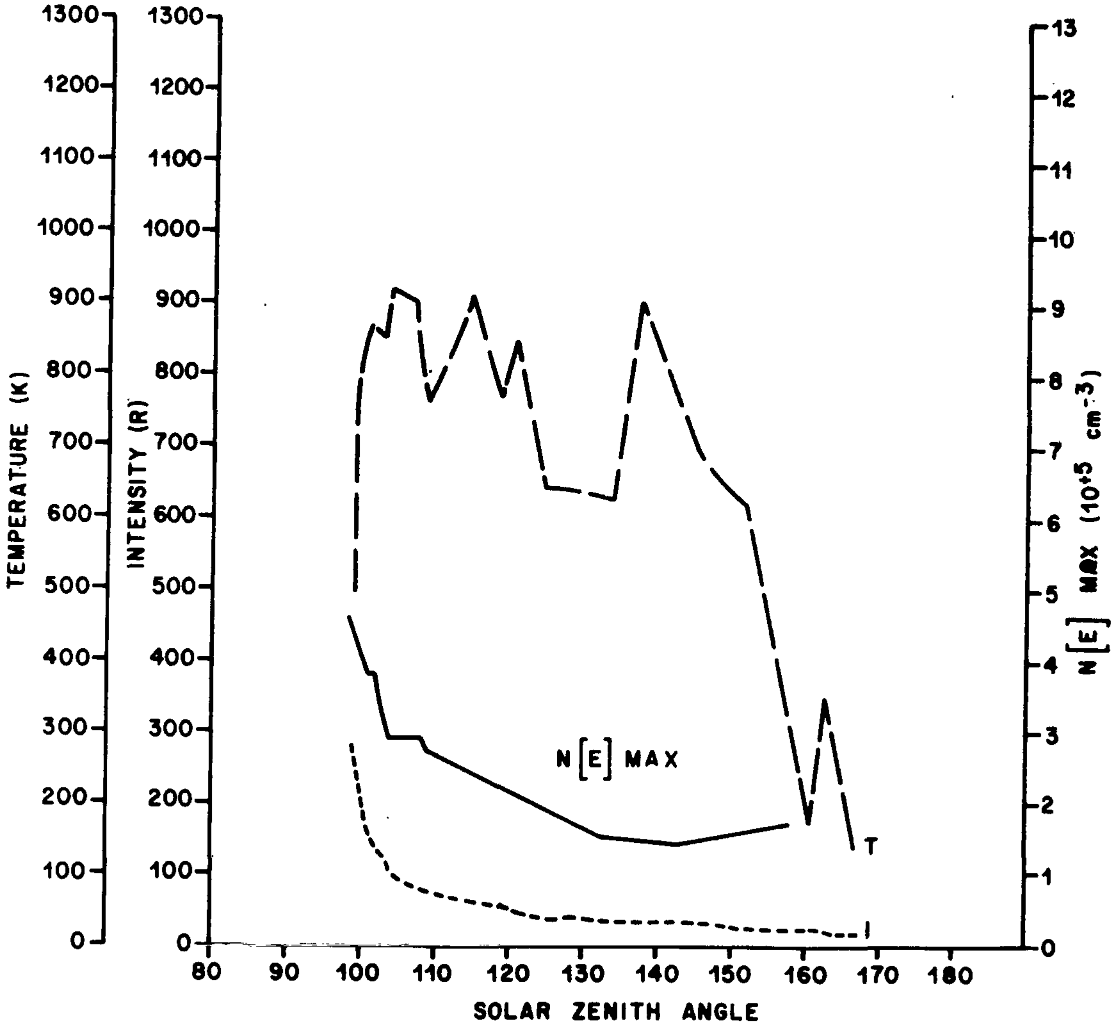

Figure C-2. Observational data for January 7, 1972.

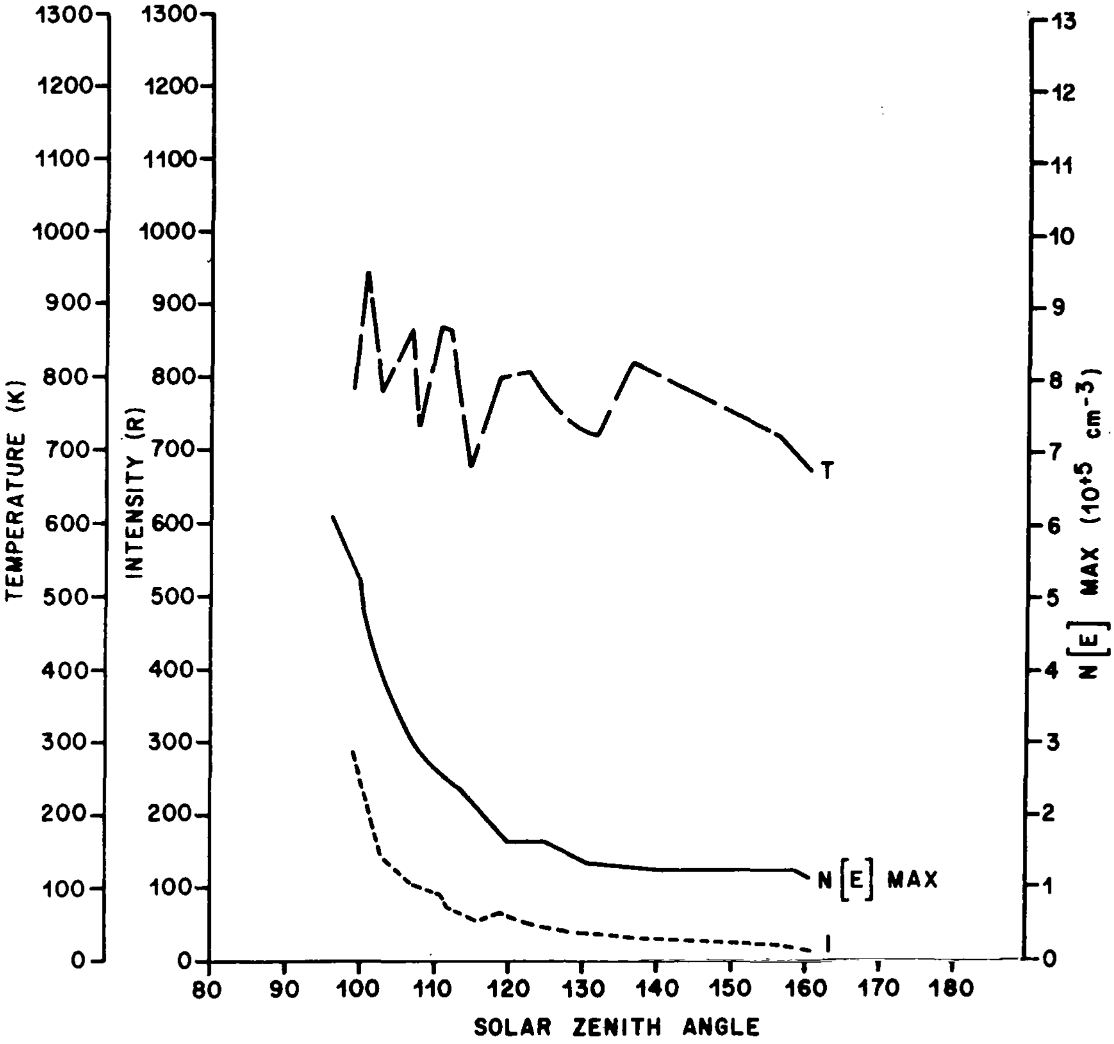

Figure C-3. Observational data for February 4, 1972.

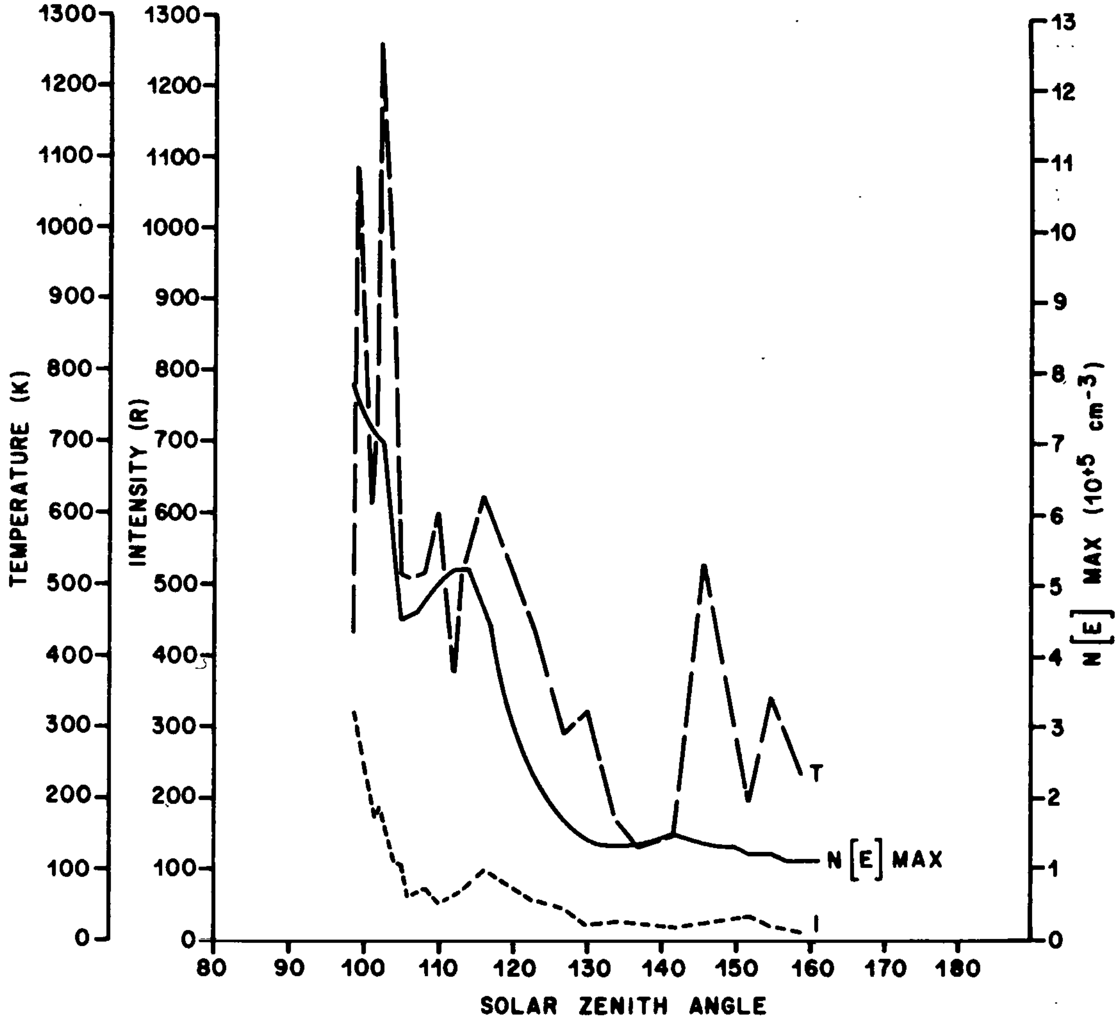

Figure C-4. Observational data for February 7, 1972.

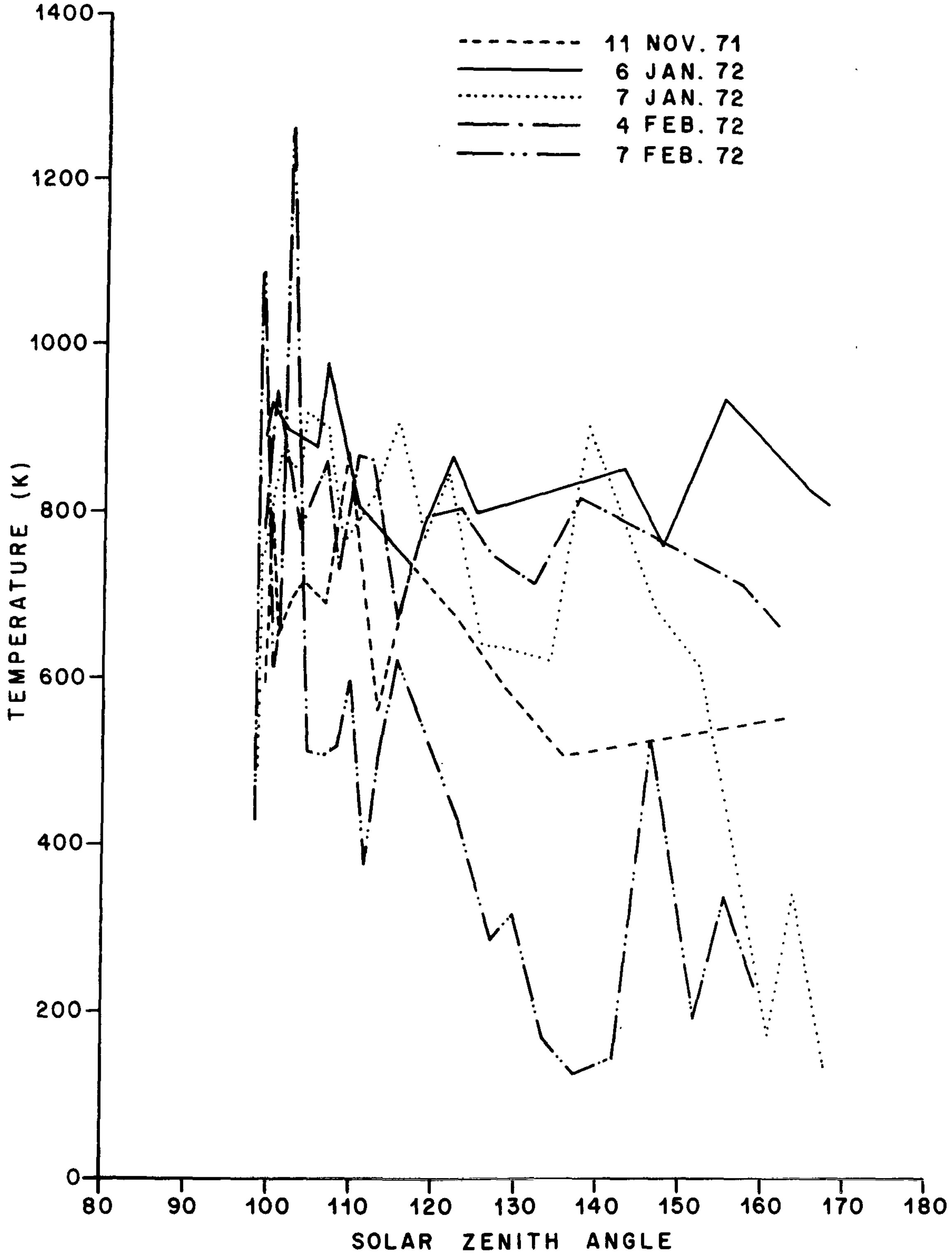

Figure C-5. Composite of sunset exospheric temperature data.

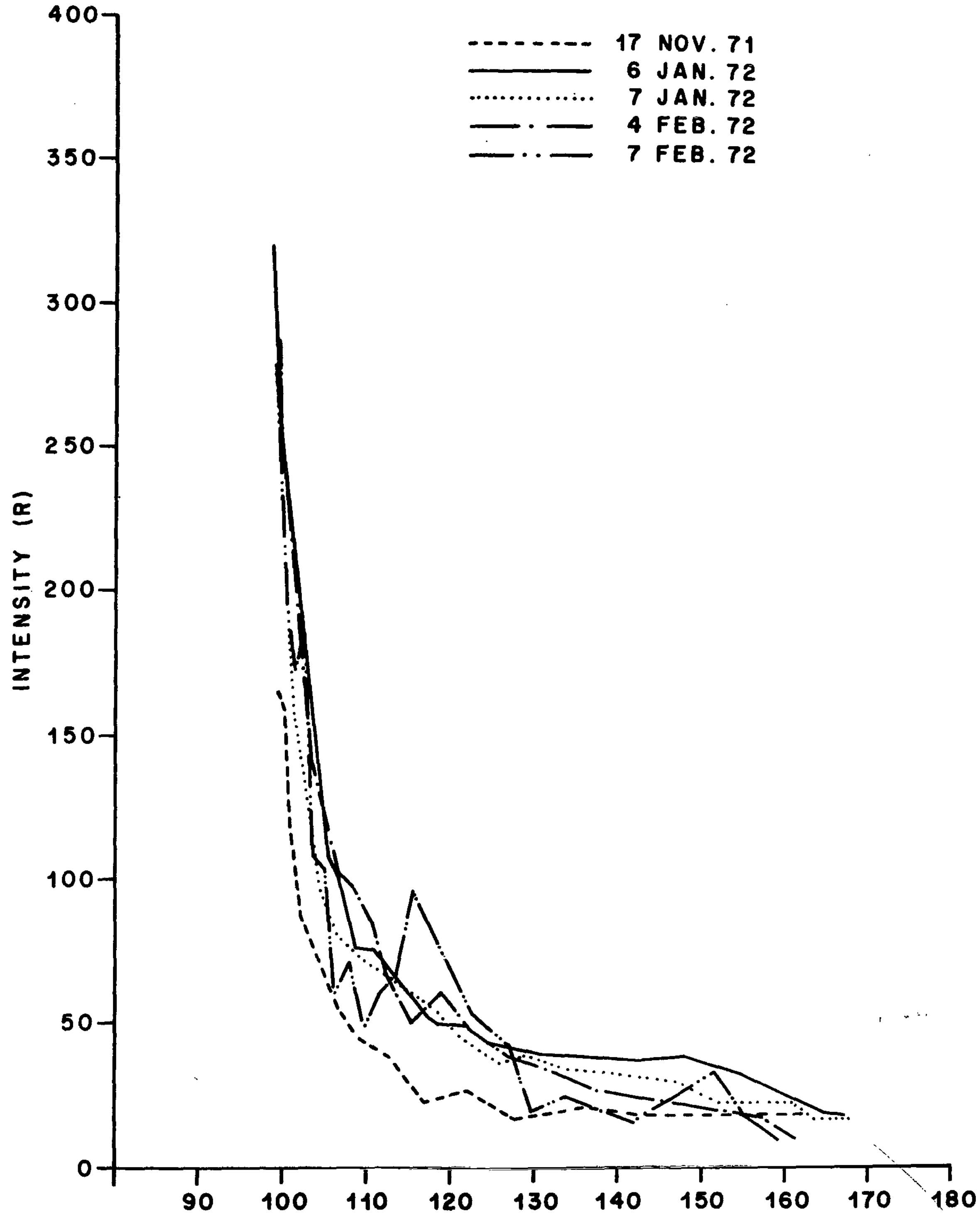

Figure C-6. Composite of sunset intensity data.

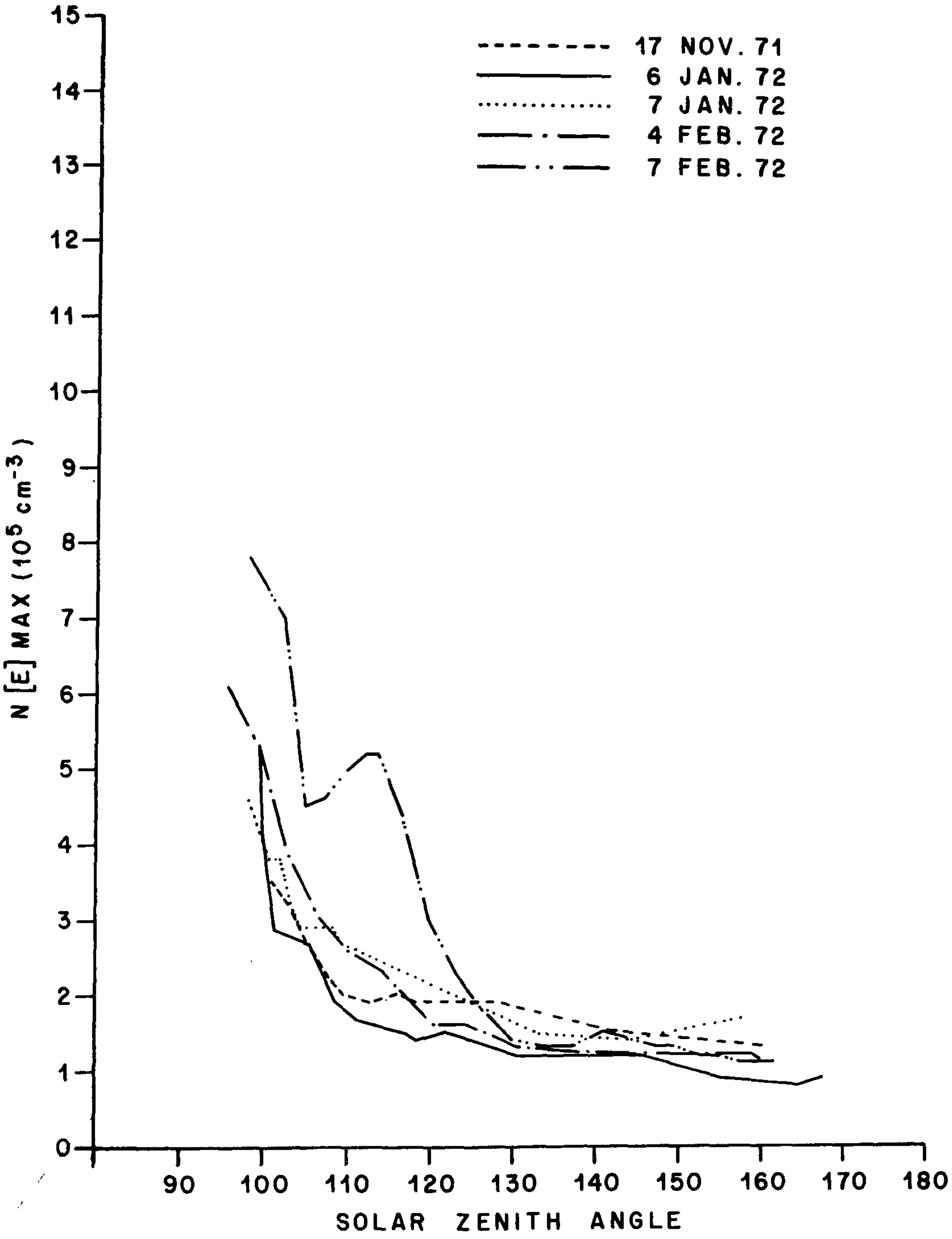

Figure C-7. Composite of sunset F_2 maximum electron density data.

APPENDIX D

CONTAMINATION OF THE 6300 Å OI EMISSION BY HYDROXYL EMISSIONS

The dominant emissions in the night sky come from radiative transitions of the OH radical. The intensity and temperature of the OH(9-3) band, which has its origin at 6356 Å [16], is important to an analysis of the 6300 Å OI emission because the OI line is embedded in this band system. Therefore, since both the turret photometer and Fabry-Perot interferometer filters used to obtain observational data in this analysis are of finite thickness, they transmit some of the OH (9-3) band emission along with the 6300 Å OI emission. The problem is to determine the magnitude of this contaminating emission.

A. Photochemistry

The detailed analysis of the OH band system by Meinel [193] showed that there was an absence of OH band emissions originating from vibrational levels with $v \geq 10$. Bates and Nicolet [194] and Herzberg [195] suggested that the source of the observed radiation might be hydroxyl radicals formed by the following mechanism, since the excitation energy of the $v = 9$ level in the electronic ground state of OH is 3.32 eV:

$$O_3 + H \rightarrow OH + O_2 + 3.32\ \text{eV} \quad . \tag{D-1}$$

Hydrogen was proposed to be regenerated by

$$OH + O \rightarrow H + O_2 \quad . \tag{D-2}$$

The spectral characteristics of the OH night glow have been reproduced in the laboratory by the ozone mechanism, equation (D-1) [196]. A photochemical model by Bates and Nicolet [194] indicated that this reaction, equation (D-1), was capable of producing the observed emission rate.

Krassovsky and Lukashenia [197] suggested the following alternative mechanism involving vibrationally excited oxygen molecules:

$$O_2^* \ (v \geq 27) + H \rightarrow OH^*(v = 9) + O \quad , \qquad \text{(D-3)}$$

with the hydrogen being regenerated by equation (D-2). Excitation of OH to the $v \geq 10$ vibrational levels, which required $O_2^*(v > 26)$, was precluded by the following:

$$O_2^* \ (v > 26) + O_2 \rightarrow O + O_3 \quad . \qquad \text{(D-4)}$$

This mechanism was disputed by Bates and Moiseiwitsch [198, 199].

Although no conclusive evidence supporting either of these mechanisms, equations (D-1) or (D-3), is in the literature, the general consensus seems to support the ozone mechanism, equation (D-1).

Table D-1 contains a more detailed list of the reactions, with their rate coefficients, that might be involved in the OH chemistry. The principal reactions involved in the OH chemistry are shown in Figure D-1 with reactions of equations (D-1) and (D-2) currently believed to be the most important.

Table D-2 lists the reactions, with their rate coefficients, currently believed to be involved in the atomic hydrogen chemistry, while Figure D-2 shows the principal reactions. Table D-3 and Figure D-3 contain the same data on the ozone chemistry. These tables and figures are from Reference 34.

1. THEORETICAL PHOTOCHEMICAL MODELS

Temporal variations of the OH intensity are of great interest since they are closely related to the chemistry of the D-region of the ionosphere. Bates and Nicolet [194] were the first to attempt theoretical calculations of the nighttime kinetics in an oxygen hydrogen atmosphere. Hunt [104, 122], Gattinger [200], and Hesstvedt [201] have also theoretically investigated diurnal variations in the OH radical production and loss rates and their height profiles. Hunt's [122] results show that the OH production rate maximum occurs at approximately 40 km altitude at noon and at approximately 80 km at midnight and while the total columnar production rate decreases by approximately

TABLE D-1. CHEMICAL KINETICS OF OH

Reactions Forming	Reactions Removing
$O^- + H \rightarrow OH + e \ 1 \times 10^{-10\pm2}$	$OH + H + M \rightarrow H_2O + M \ 1 \times 10^{-31\pm1}$
$H_2O + h\nu \rightarrow OH + H \ \lambda < 2390Å$	
$H_2O_2 + h\nu \rightarrow HO + HO \ \lambda < 5650Å$	$OH + O \rightarrow H + O_2 \ (5\pm2) \times 10^{-11}$
$O(^1D) + H_2O \rightarrow OH + OH \ 1 \times 10^{-11}$	$OH + H \rightarrow O + H_2 \ 9 \times 10^{-12\pm0.3} \ e^{-3800/T}$
$H + O_2 \rightarrow OH + O \ 4 \times 10^{-10\pm0.3} \ e^{-8400/T}$	$OH + H_2 \rightarrow H_2O + H \ 6.3 \times 10^{-11\pm0.3} \ e^{-2750/T}$
$H + O_3 \rightarrow OH + O_2 \ 1 \times 10^{-11\pm2} \ e^{-500/T}$	$OH + OH \rightarrow H_2O + O \ 1.4 \times 10^{-11\pm0.3} \ e^{-500/T}$
$O + HO_2 \rightarrow OH + O_2 \ 1 \times 10^{-11}$	$OH + O_3 \rightarrow O_2 + HO_2 \ 1.5 \times 10^{-11} T^{0.5} \ e^{-4/RT}$
$H + HO_2 \rightarrow OH + OH \ 2 \times 10^{-10\pm1} \ e^{-500/T}$	$OH + HO_2 \rightarrow H_2O + O_2 \ 2 \times 10^{-11\pm1}$
$O + H_2O_2 \rightarrow OH + HO_2 \ 1 \times 10^{-12\pm2} \ e^{-2000/T}$	$OH + H_2O_2 \rightarrow H_2O + HO_2 \ 3 \times 10^{-11\pm1} \ e^{-500/T}$
$HO_2 + O_3 \rightarrow OH + O_2 + O_2 \ 1 \times 10^{-14\pm2}$	$OH + OH + M \rightarrow H_2O_2 + M \ 3.3 \times 10^{-30\pm0.5} \ (T/300)^{-1}$
$O + H + M \rightarrow OH + M \ 1 \times 10^{-33\pm1}$	

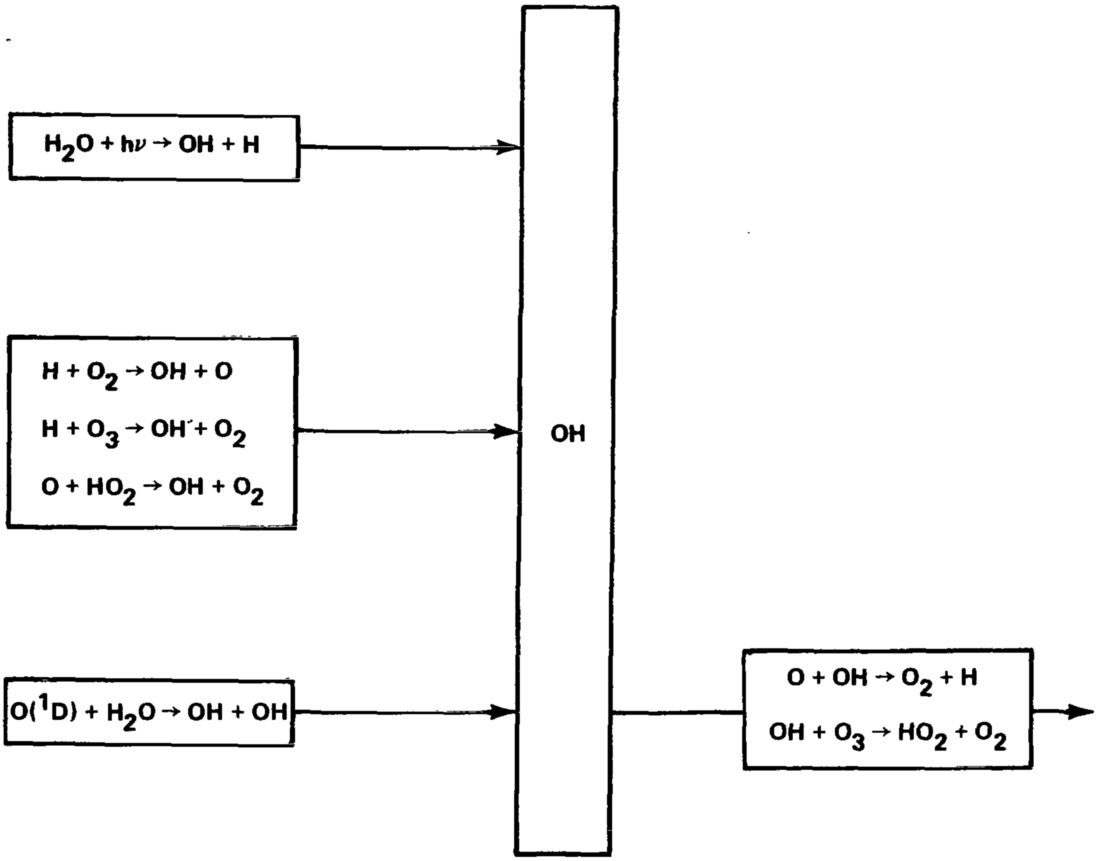

Figure D-1. Chemical kinetics of OH principal reactions.

60 percent between noon and midnight, the integrated intensity remains approximately the same. This is because the higher production rate in the daytime occurs at a lower altitude where the excited state is collisionally deactivated before it can radiate. Intensity-height profile results from Hunt's [122] theoretical calculations also agree very well with the rocket observations of Packer [202].

OH intensity temporal variations in the night glow can only be due to changes in the concentration of hydrogen or ozone. These changes may be due either to changes in the altitude of the emitting layer or to changes in the reaction rate coefficients due to changes in the ambient temperature. According to Sivjee [144], theoretical calculations of ozone and hydrogen concentrations at a fixed altitude based on chemical equilibrium concepts show long rise and fall times, on the order of 6 to 12 h. These results are in serious conflict with

TABLE D-2. CHEMICAL KINETICS OF H

Reactions Forming	Reactions Removing
$H_2O + h\nu \rightarrow H + OH$ $\lambda < 2390$Å	$H + O^- \rightarrow OH + e$ $1 \times 10^{-10\pm2}$
$O + OH \rightarrow H + O_2$ $5\pm2 \times 10^{-11}$	$H + O_2 + M \rightarrow HO_2 + M$ $5\pm2 \times 10^{-32}$ $(T/300)^{-2.0\pm0.5}$
$OH + H_2 \rightarrow H + H_2O$ $6.3 \times 10^{-11\pm0.3}$ $e^{-2750/T}$	$H + O + M \rightarrow OH + M$ $1 \times 10^{-33\pm1}$
	$H + H + M \rightarrow H_2 + M$ $1 \times 10^{-32\pm0.5}$ $(T/300)^{-1}$
	$H + OH + M \rightarrow H_2O + M$ $1 \times 10^{-31\pm1}$ $(T/300)^{-2}$
	$H + OH \rightarrow H_2 + O$ $9 \times 10^{-12\pm0.3}$ $e^{-3800/T}$
	$H + O_3 \rightarrow OH + O_2$ $1 \times 10^{-11\pm2}$ $e^{-500/T}$
	$H + O_3 \rightarrow O + HO_2$ $1 \times 10^{-12\pm2}$ $e^{-120/T}$
	$H + HO_2 \rightarrow H_2O + O$ $1 \times 10^{-12\pm2}$ $e^{-500/T}$
	$H + HO_2 \rightarrow OH + OH$ $2 \times 10^{-10\pm1}$ $e^{-500/T}$
	$H + HO_2 \rightarrow H_2 + O_2$ $6 \times 10^{-11\pm1}$ $e^{-500/T}$
	$H + H_2O_2 \rightarrow H_2 + HO_2$ $1 \times 10^{-12\pm2}$ $e^{-1800/T}$
	$H + O_2 \rightarrow O + OH$ $4 \times 10^{-10\pm0.3}$ $e^{-4800/T}$

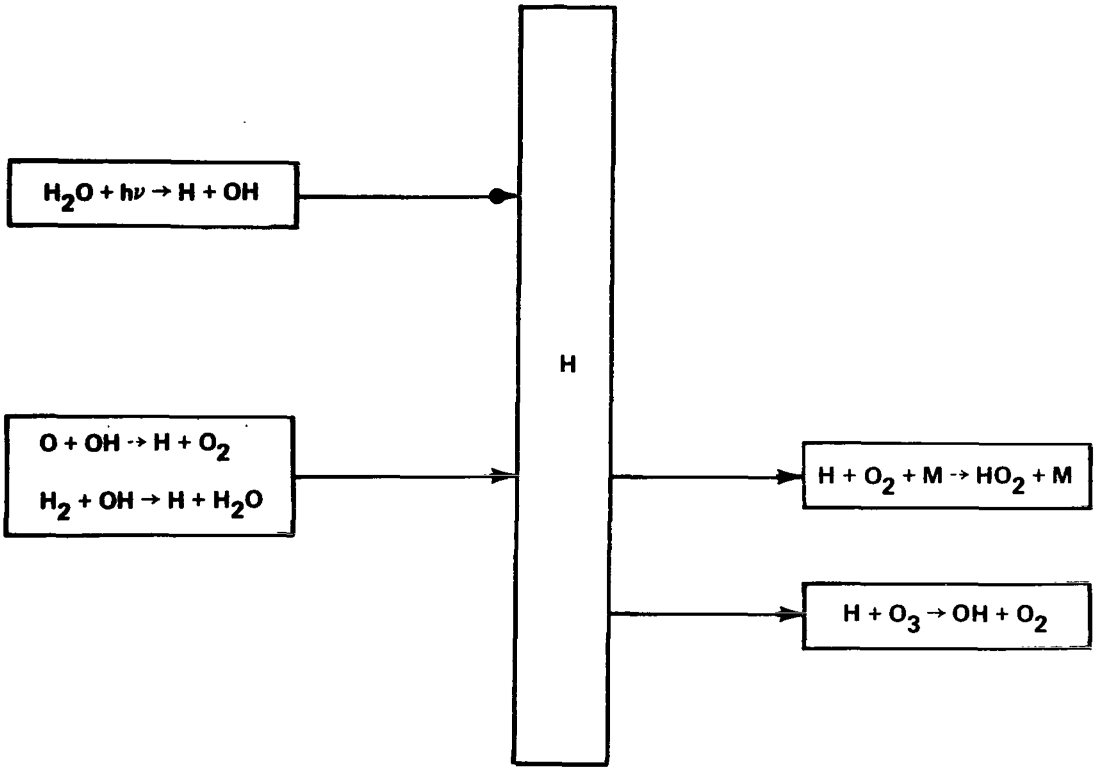

Figure D-2. Chemical kinetics of H principal reactions.

observational data that show short-lived variations [144], on the order of minutes to hours; therefore, constituent number density variations at a fixed altitude do not appear to be the cause of the temporal variations.

Sivjee [144] concludes that the short-lived variations in OH intensity are due to changes in the altitude of the emitting layer with the higher intensities occurring when the layer moves up to the altitude of the atomic oxygen number density peak near 95 to 97 km. These higher intensities are primarily a combined result of an increase in the atomic oxygen number density that controls the amount of O_3 available to react with atomic hydrogen through

$$O + O_2 + M \rightarrow O_3 + M \tag{D-5}$$

TABLE D-3. CHEMICAL KINETICS OF O_3

Reactions Forming	Reactions Removing
$O_3^- + N_2^+ \rightarrow O_3 + N_2$ $2 \pm 1.5 \times 10^{-7}\ (T/300)^{-1 \pm 0.5}$	$O_3 + e \rightarrow O_3^- + h\nu$ $1 \times 10^{-17 \pm 2}$
$O_3^- + O^+ \rightarrow O_3 + O$ $2 \pm 1.5 \times 10^{-7}\ (T/300)^{-1 \pm 0.5}$	
	$O_3 + e \rightarrow O^- + O_2$ $3 \times 10^{-12 \pm 1.5}$
$O_3^- + NO^+ \rightarrow O_3 + NO$ $2 \pm 1.5 \times 10^{-7}\ (T/300)^{-1 \pm 0.5}$	$O_3 + O_2^- \rightarrow O_3^- + O_2$ $4.0 \pm 1.3 \times 10^{-10}$
	$O_3 + O^- \rightarrow O_3^- + O$ $5.3 \pm 2 \times 10^{-10}$
	$O_3 + h\nu \rightarrow O + O_2$ wavelength and flux dependent
$O_3^- + h\nu \rightarrow O_3 + e$ $6 \pm 2 \times 10^{-2}$	$O_3 + O_2\,(^1\Delta) \rightarrow O + O_2 + O_2$ $1.7 \times 10^{-12 \pm 0.3}\, e^{-1430/T}$
$O_2^- + O \rightarrow O_3 + e$ $2.5 \pm 1.5 \times 10^{-10}$	$O_3 + O_2\,(^1\Sigma) \rightarrow O_2 + O_2$ $6 \times 10^{-13 \pm 1}$
$O^- + O_2\,(^1\Delta) \rightarrow O_3 + e$ 5×10^{-15}	$O_3 + O \rightarrow O_2 + O_2$ $1.4 \pm 0.3 \times 10^{-12}\, e^{(-1500 \pm 200)/T}$
$O^- + O_2\,(^1\Sigma) \rightarrow O_3 + e$ 5×10^{-15}	$O_3 + N \rightarrow NO + O_2$ $5.7 \times 10^{-13 \pm 0.3}$
$O_3^- + NO_2 \rightarrow O_3 + NO_2$ $7 \times 10^{-10 \pm 2}$	$O_3 + NO \rightarrow O_2 + NO_2$ $9.5 \pm 1 \times 10^{-13}\, e^{(-1300 \pm 100)/T}$
	$O_3 + NO_2 \rightarrow O_2 + NO_3$ $2.6 \times 10^{-13 \pm 5}\, e^{(-7000 \pm 600)/T}$
	$O_3 + H \rightarrow OH + O_2$ $1 \times 10^{-11 \pm 2}\, e^{-500/T}$
$O_2^+ + NO_2 \rightarrow O_3 + NO^+$ $1 \times 10^{-11 \pm 2}$	$O_3 + H \rightarrow O + HO_2$ $1 \times 10^{-12 \pm 2}\, e^{-120/T}$
$O + O_2 + M \rightarrow O_3 + M$ $5.5 \pm 2 \times 10^{-34}\ (T/300)^{-2.5 \pm 0.3}$	$O_3 + OH \rightarrow HO_2 + O_2$ $1.5 \times 10^{-11} T^{0.5} e^{-4/RT}$
	$O_3 + HO_2 \rightarrow OH + O_2 + O_2$ $1 \times 10^{-14 \pm 2}$
	$O_3 + O(^1D) \rightarrow O_2 + O_2$ $7 \times 10^{-12 \pm 1}$
$O_2^+ + O_2^- \rightarrow O + O_3$ $1 \times 10^{-11 \pm 2}$	$O_3 + NO^+ \rightarrow NO_2^+ + O_2$ $1 \times 10^{-13 \pm 2}$

and an increase in the reaction rate coefficient for equation (D-1) due to an increase in the ambient temperature, although the atomic hydrogen number density does increase somewhat with height at these altitudes. His calculations are in excellent agreement with the rocket observations of Packer [202] and

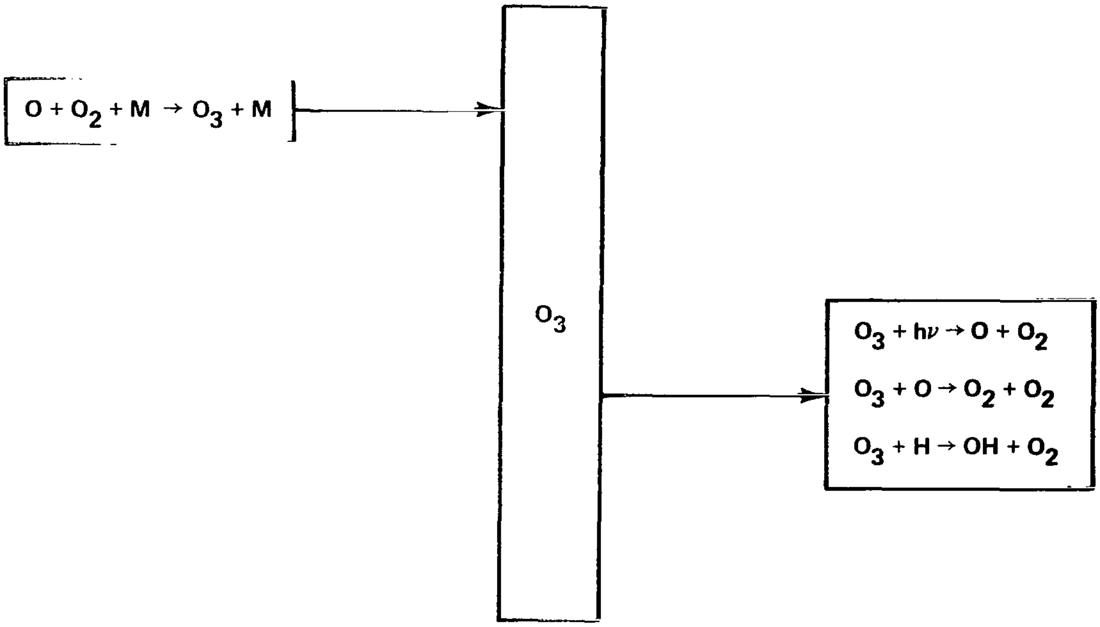

Figure D-3. Chemical kinetics of O_3 principal reactions.

Baker and Waddoups [203]. When the emitting layer moves upward, it moves where the ambient temperature is higher; thus, his calculations support the observational data of Krassovsky et al. [204] and Huruhata [205] that there is a dependence of OH intensity on rotational temperature.

If Sivjee's [144] conclusions are correct, a dynamical atmosphere at D-region altitudes, approximately 80 to 100 km, might provide a possible explanation for the extremely low and rapidly changing temperatures derived from Fabry-Perot interferometer measurements (Fig. C-1 through C-5) of the 6300 Å OI emission. The configuration of the F-P interferometer used in this study is such that any OH (9-3) band contamination is added to the 6300 Å OI emission line profile at the peak. The addition of any OH emission that is at a lower temperature (approximately 150 to 250 K) causes a reduction in the derived temperature with the reduction being almost linearly related to the amount of OH intensity present as well as the rotational temperature of the emitting OH radicals. For example, if the observed emission consists of 80 percent 6300 Å photons from ^1D atoms at a temperature of 1000 K and 20 percent 6306.837 Å photons from OH radicals at a temperature of 200 K, the data reduction technique used herein would derive a temperature of approximately 800 K for the emission. Additional observational data are required to separate the possible two components that may have resulted in the low temperature data shown in Figures C-1 through C-5; however, it appears from Sivjee's [144] work that vertical motions on the order of 10 to 15 km due to vertical circulations or acoustic or internal gravity wave propagation could very well explain the observed abrupt, short-lived changes in intensity and/or temperature.

B. Observations of Intensity and Rotational Temperature

The original work on the OH emissions was done by Meinel [193] who found that for the time period from about 1.5 h after sunset to approximately 1.5 h before sunrise, approximately 50 percent of the 6300 Å OI emission measured with a broad bandpass filter was really due to the OH(9-3) band system. Chamberlain and Smith [205a], on the basis of theoretical calculations, predicted that the intensity of the OH(9-3) band should be approximately 110 R. Blackwell et al. [206] reported an observed value of 81 R at a rotational temperature of 294 K. The following year Krassovsky et al. [204], from observations at Yakutsk, USSR, reported a value of 140 R with a dependence on the rotational temperature. They also observed a seasonal variation with a winter maximum at Yakutsk. In the same paper they reported that observations at Zvenigorod, USSR, showed neither a temperature dependence nor a seasonal variation but a definite enhancement on cloudy nights. G. Kvifte [207] reported an intensity of 160 R for the OH(9-3) band. Huruhata [205] found that large variations in the intensity of hydroxyl emissions in one night were due to ascending and descending motions of the emitting layer. He also found that the intensity increased when the 10 mb pressure surface (approximately 30 km) decreased. However, a review paper by Krasovsky and Shefov [208] attributed the variations in intensity and rotational temperature to spatial patchiness and not vertical displacements. Greenspan [209] in an analysis of the spatial variability of the OH emissions reported that the latitudinal distribution showed a minimum near 30°N. G. J. Kvifte [210] reported a value of 90 to 110 R for the OH(9-3) band over an observatory in Norway, while Chiplonkar and Tillu [211] reported an intensity value of 113 R over Poona, India. L. L. Smith [212] reported that observations over Hawaii indicated that OH(9-3) band intensity did not covary with the 6300 Å OI emission intensity, while Shefov [213] showed that there was a correlation between the OH intensity and the solar cycle. He also found that seasonal variations in wind speed and direction did affect the seasonal variations in OH intensity. Sivjee [144] found no enhancement of OH intensity during either electron or proton auroras. Thus, it appears that there are many inconsistencies and unknowns in the strength and variability of the OH emissions. From the sparse data available, Huntsville, Alabama, is apparently located where there is a minimum in the latitudinal distribution of the intensity; however, this could be offset by the fact that there is a winter maximum in intensity of the upper vibrational levels [213] and also by the fact that the level of solar activity was relatively high on January 6, 1972. Observational data [144, 213] indicate a minimum in OH intensity between approximately 2200 and 2345 CST.

Rao and Kulkarni [214] reported that contamination of the 6300 Å OI emission intensity observations by nearby hydroxyl lines is very small where filters with half-widths $\leq$ 10 Å are used; however, the contamination could not be neglected for filters with half-widths > 40 Å. They reported the following relative intensities for the lines:

Line	Band	Relative Intensity
6300 Å		3
6264 Å		1
6287.6 Å	$P_1(2)$ (9-3)	0.0763
6298.7 Å	$P_2(3)$ (9-3)	0.0390
6306.8 Å	$P_1(3)$ (9-3)	0.0922

This table shows that for every three photons of 6300 Å OI emission there is one 6364 Å photon, 0.0763 $P_1(2)$ photons, 0.0390 $P_2(3)$ photons, and 0.0922 $P_1(3)$ photons.

The photometer used to obtain the observational data used in this analysis had a 6300 Å filter with a 15 Å half-width and an 80 percent transmission at the peak. Portions of the emissions in all three lines listed were transmitted through the filter and recorded as 6300 Å OI intensity.

The filter transmission function is combined with the above information on the position and relative intensities of these lines to compute the percentage of the observed intensity that should be attributed to the OH (9-3) band using the following:

$$\text{Total Relative Int.} = T_{6287.6}R(I)_{6287.6} + T_{6306.8}R(I)_{6306.8} + T_{6298.7}R(I)_{6298.7}$$

$$= (0.13)(0.0763) + (0.44)(0.0922) + (0.73)(0.0390)$$

$$= (0.0099) + (0.0406) + (0.0285) = 0.0790 \quad .$$

The percent of the observed intensity due to the OH(9-3) band emission is, therefore, equal to the total relative intensity of the three OH lines divided by the relative intensity of the 6300 Å OI emission, or

$$\frac{0.0790}{3.0} \times 100 = 2.63\% \quad .$$

The Fabry-Perot interferometer used in this analysis had a filter with a 5.2 Å half-width and a 55 percent transmission at the peak. A recent report by Hernandez[5] contains the new determinations of the positions of the $P_1(3)$ and $P_2(3)$ lines as $6306.83_7 \pm 0.009$ Å and $6297.99_2 \pm 0.004$ Å, respectively. Figure D-4 shows the 6300 Å filter transmission function. The positions of the three nearby OH lines are indicated on the figure, which shows that only approximately 3 percent of the $P_1(3)$ line is transmitted through the filter, approximately 36 percent of the $P_2(3)$ line, and less than 3 percent of the $P_1(2)$ line.

With these new wavelengths and an etalon spacing of 1 cm, which results in a free spectral range of 0.198 Å for this Fabry-Perot interferometer, it is possible to calculate where the above OH emission lines lie with respect to the OI line. These calculations show that:

1. The $P_2(3)$ line lies between 0.054 and 0.062 Å from the OI line with the most probable position being 0.060 Å from the OI line.

2. The $P_1(3)$ line lies between 0.003 and 0.021 Å from the OI line with the most probable position being 0.007 Å from the OI line.

3. The $P_1(3)$ line lies 0.036 Å from the OI line.

---

[5] Hernandez, op. cit.

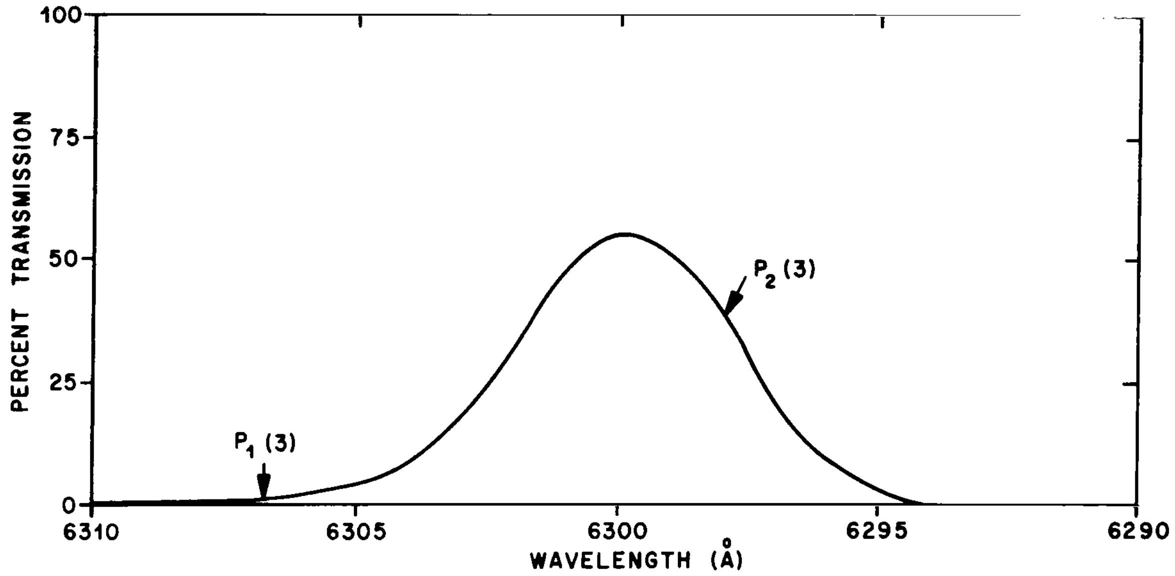

Figure D-4. 6300 Å filter transmission function.

Figure D-5 shows the position of these OH lines on a plot of an OI line shape which is a convolution of 18 emission line profile measurements on the night of January 6, 1972, between 1800 and 2330 CST. The average temperature derived from this convolution is 841 K. From the plot it is impossible to ascertain if there is any emission from the $P_1(3)$ line mixed with the OI line; however, neither the $P_2(3)$ nor the $P_1(2)$ lines appear to be present. During this time period the OI line intensity decreased from approximately 100 R to approximately 18 R; therefore, it is believed that a $P_2(3)$ line intensity of a constant 2 R would be discernible on this plot. If this value can be used as an upper limit on the intensity of the $P_2(3)$ line, the results of Rao and Kulkarni [214] and those of Hernandez indicate that the intensity of the $P_1(3)$ line should have been approximately 4.6 R. The transmission function of the filter is such that only 3 percent of the intensity of this line is transmitted; therefore, only approximately 0.138 R could be attributed to the OH emission.

The individual emission line shape measurements for this night are shown in Figures 6 through 17. There is no indication in any of these measurements that the $P_2(3)$ emission line is present; therefore, it is believed that the contamination of the OI emission line by the $P_1(3)$ OH emission line is negligible on this night.

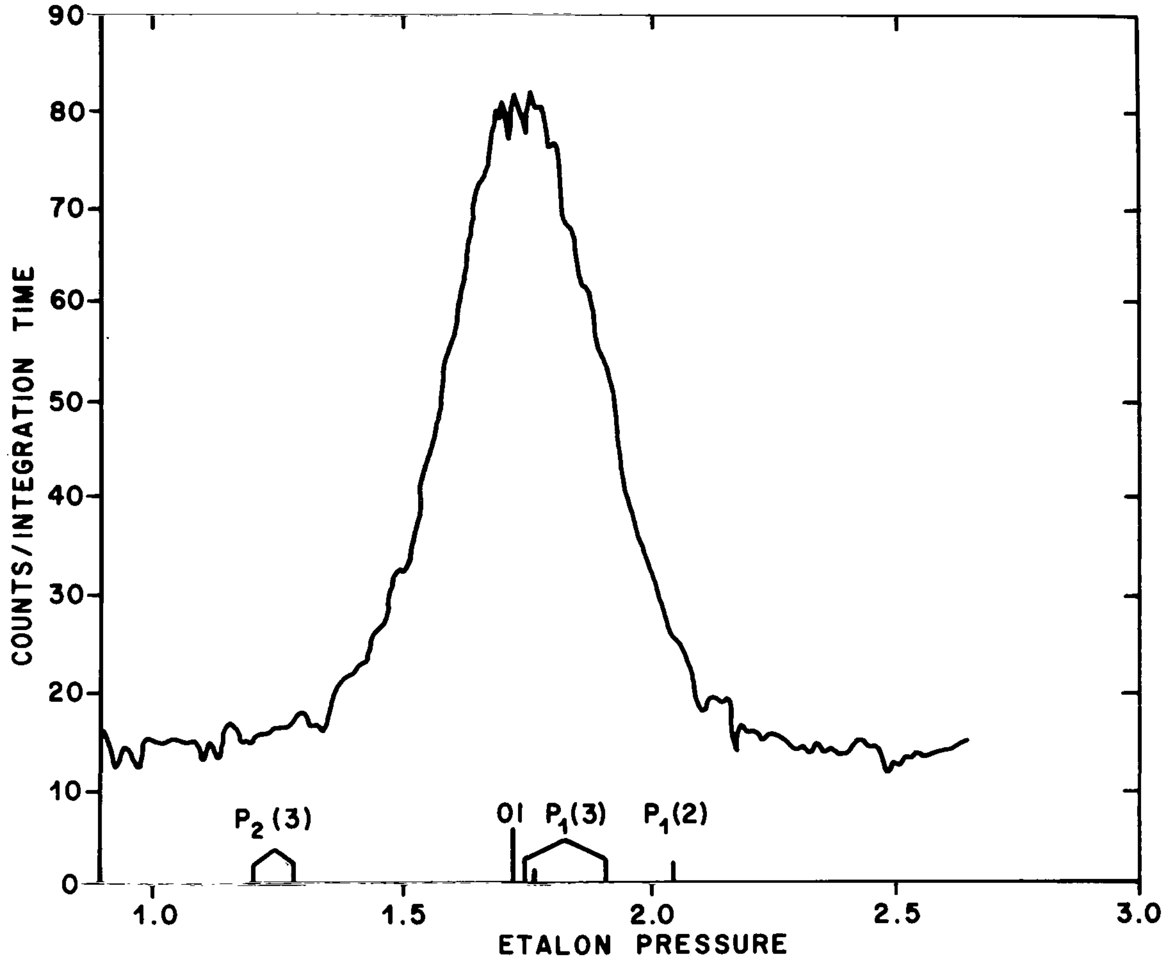

Figure D-5. Convolution of 18 emission line profiles from January 6, 1972, with expected positions of OH lines.

To support this contention, the data were subjected to two additional analyses. First, the data were input to a computerized version of a statistical analysis technique capable of separating a mixture of distribution into its components. This analysis showed that the data were not a mixture of signals but a single distribution.

In the second analysis, several theoretical emission line profiles were generated and reduced with the results shown on Figure D-6. The values of the coefficients of the transforms for the theoretical 200 K profile and the 1000 K profile are shown as squares and circles, respectively. For comparison, the

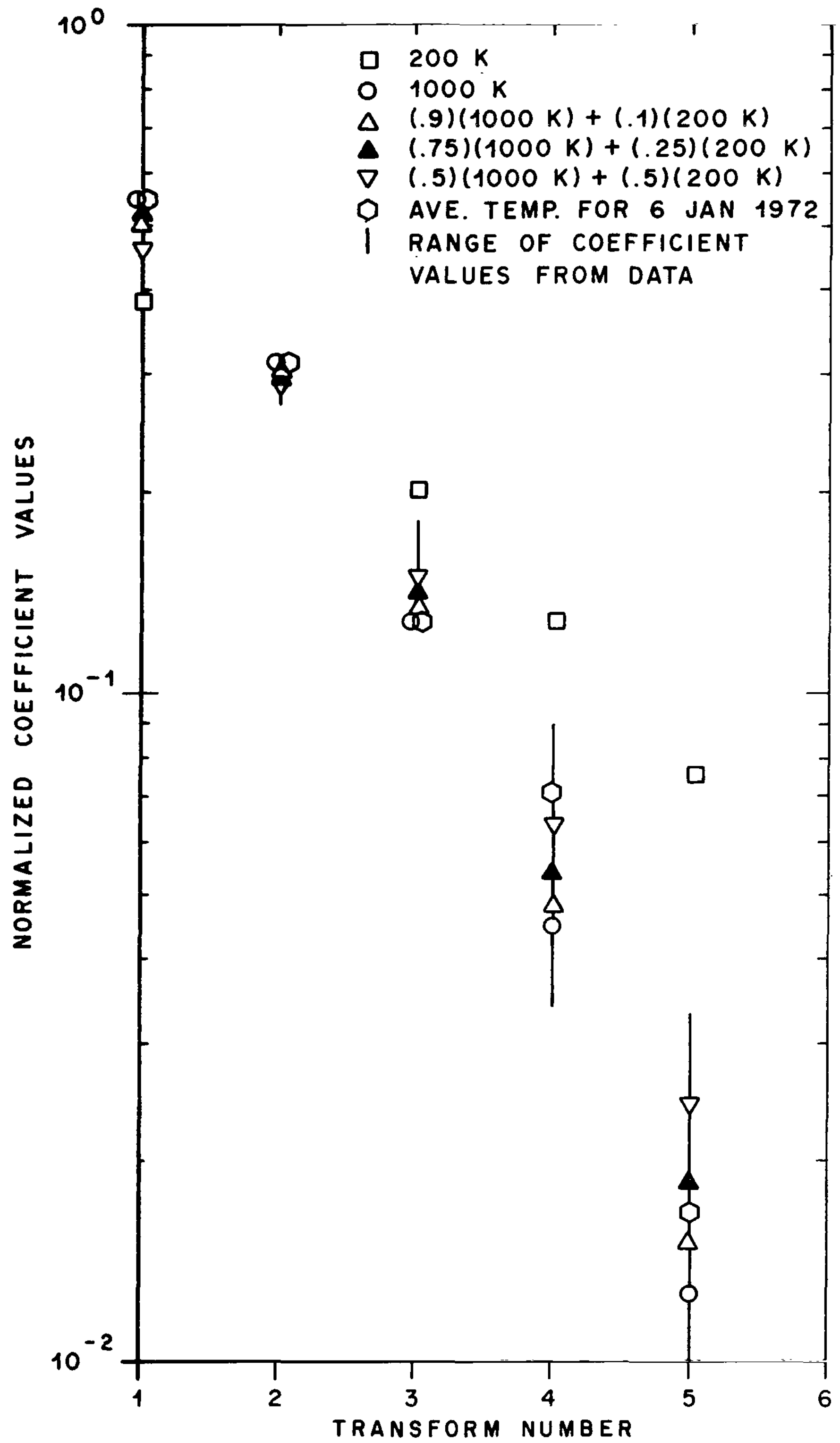

Figure D-6. Comparison of values of Fourier transform coefficients from theoretical line profiles with those from observational data.

triangles show values of the coefficients obtained from theoretically calculated emission line profiles containing varying ratios of the intensities from a 1000 K and a 200 K source. The transforms from the observational data are also plotted on this figure with all values normalized to the value of the coefficient of the first transform of the 1000 K profile. Neither the values of the coefficients obtained from the analysis of the theoretical mixtures of sources at two different temperatures nor their trends with transform number have characteristics that are significantly different from those of a single temperature source. Therefore, this technique cannot be used to distinguish emission lines due to a mixture at two different temperatures from emission lines due to a single temperature source.

The decrease in the observed intensity at conjugate point sundown provides additional evidence that the major portion of the observed emission is due to the atomic oxygen transition, since the OH emission cannot be affected in any way by conjugate point conditions.

For these reasons it is believed that the observational data used in this analysis are from the 6300 Å OI line uncontaminated by any 9-3 OH band emission.

REFERENCES

1. Jacchia, L. G.: Smithsonian Contrib Astrophys, vol. 8(9), 1965.

2. Reber 1973

3. Bates, D. R.: Proc Roy Soc, London, vol. A253, p. 451, 1959.

4. Jacchia, L. G.: Smithsonian Astrophys Obser Spec Report, No. 332, 1971.

5. Ackerman, M.: Aeronomic Acta, p. A77, 1970.

6. Hinteregger, H. E.; Hall, L. A.; and Schmidtke, G.: Space Res, vol. 5, pp. 1175-1190, 1965.

7. Metzger, P. H. and Cook, G. R.: J Quant Spectros Radiat Transf, vol. 4, p. 107, 1964.

8. Peterson, V. L. and Steiger, W. R.: J Geophys Res, vol. 71, pp. 2267-2277, 1966.

9. Brandt, J. C.: Astrophys J, vol. 128, pp. 718-723, 1958.

10. Noxon, J. F.: J Geophys Res, vol. 69, pp. 3245-3255, 1964.

11. Dalgarno, A. and Walker, J. C. G.: J Atmos Sci, pp. 473-474, 1964.

12. Wallace, L. and McElroy, M. B.: Planet Space Sci, vol. 14, pp. 677-708, 1966.

13. Bates, D. R.: Mon Not Roy Astron Soc, vol. 106, p. 509, 1946.

14. Barbier, D.: Comptes Rendux, vol. 244, pp. 1809-1811, 1957.

15. Chamberlain, J. W.: Astrophys J, vol. 127, pp. 54-98, 1958.

16. Chamberlain, J. W.: Physics of Aurora and Airglow. Academic Press, New York, 1961.

17. Biondi, M. A. and Feibelman, W. A.: Planet Space Sci, vol. 16, pp. 431-443, 1968.

REFERENCES (Continued)

18. Biondi, M. A. and Brown, S. C.: Phys Rev, vol. 76, p. 1697, 1949.

19. Sayer, J.: Solar Eclipses and the Ionosphere. Ed. by W. J. G. Beynon and G. M. Brown, Pergamon Press, London, p. 212, 1956.

20. Nicolet, M. and Aikin, A. C.: J Geophys Res, vol. 65, p. 1469, 1960.

21. Kasner, W. H.; Rogers, W. A.; and Biondi, M. A.: Phys Rev Letters, vol. 7, p. 321, 1961.

22. Danilov, A. D.: Dokl Akad Nauk, SSSR, vol. 137, p. 1098, 1961.

23. Whitten, R. C. and Poppoff, I. G.: J Geophys Res, vol. 66, p. 2779, 1961 and corrected ibidem, vol. 67, p. 3000, 1962.

24. Ivanov-Kholodony, G. S.: Geomagnetizm i Aeronomiva, vol. 2, p. 377, 1962.

25. Norton, R. B.; Van Zandt, T. E.; and Denison, J. S.: Proceedings of the International Conference on the Ionosphere. Inst Phys and Phys Soc, London, p. 26; 1963.

26. Bortner, M. G.: AFCRL-65-392, April 1965.

27. Swider, W., Jr.: J Geophys Res, vol. 70, p. 4859, 1965.

28. Zipf, E. C.: Bull Am Phys Soc, vol. 11, p. 494, 1966.

29. Warke, C. S.: Phys Rev, vol. 144, p. 120, 1966.

30. DSA Reaction Rate Handbook, July, 1967.

31. Kasner, W. H. and Biondi, M. A.: Bull Am Phys Soc, vol. 12, p. 218, 1967.

32. Kasner, W. H. and Biondi, M. A.: Phys Rev, vol. 174, p. 139, 1968.

33. Chan, F. T.: J Chem Phys, vol. 49, pp. 2533-2540, 1968.

REFERENCES (Continued)

34. Bortner, M. and Kummler, R.: The Chemical Kinetics and the Composition of the Earth's Atmosphere, GE-9500-ECS-SR-1, 1968.

35. Biondi (1972)

36. Wickwar, V. B.: Ann Geophys, vol. 27, pp. 187-192, 1972.

37. Gunton, R. C. and Inn, E. C. Y.: J Chem Phys, vol. 35, p. 1869, 1961.

38. Lin, S. C.: Ann Geophys, vol. 17, p. 16, 1961.

39. Syverson, M. W.; Stein, R. P.; Shaw, T. M.; Scheibe, M.; and Gunton, R. C.: Bull Am Phys Soc, vol. 7, p. 378, 1962.

40. Doering, J. P. and Mahan, B. H.: J Chem Phys, vol. 36, p. 669, 1962.

41. Saxena, P. P.: Ann Geophys, vol. 24, pp. 1023-1030, 1968.

42. Weller, C. S. and Biondi, M. A.: Bull Am Phys Soc, vol. 13, p. 199, 1968.

43. Weller, C. S. and Biondi, M. A.: Phys Rev, vol. 172, p. 198, 1968.

44. Bardsley, J. N.: J Phys, vol. B1, p. 365, 1968.

45. Meira, L. G., Jr.: Rocket Measurements of Upper Atmospheric Nitric Oxide and Their Consequences to the Lower Ionosphere. NASA CR-1690, February 1971.

46. Zipf, E. C. and Fastie, W. G.: J. Geophys Res, vol. 68, pp. 6208-6209, 1963.

47. Tohmatsu, T.; Ogawa, T.; and Tsuruta, H.: Rept of Ionosphere Space Res Japan, vol. 19, pp. 482-508, 1965.

48. Brown, W. E. and Steiger, W. R.: Nature, vol. 216, p. 47, 1967.

49. Donahue, T. M.; Parkinson, T.; Zipf, E. C.; Doering, J. P.; Fastie, W. G.; and Miller, R. E.: Planet Space Sci, vol. 16, pp. 737-747, 1968.

REFERENCES (Continued)

50. Gulledge, I. S.; Packer, D. M.; Tilford, S. G.; and Vanderslice, J. T.: J Geophys Res, vol. 73, pp. 5535-5547, 1968.

51. Zipf, E. C.: Bull Am Phys Soc, vol. 15, p. 418, 1970.

52. Forbes, J. M.: J Atmos Terr Phys, vol. 32, pp. 1901-1908, 1970.

53. Hanson, W. B.: Space Res 3, p. 173, North Holland Printing Co, Amsterdam, 1963.

54. Cole, K. D.: Annls Astrophys, vol. 21, p. 156, 1965.

55. Carlson, H. C., Jr.: Ph.D. Thesis, Cornell University, Ithaca, New York, 1965.

56. Carlson, H. C., Jr.: J Geophys Res, vol. 71, pp. 195-199, 1966.

57. Bates, D. R. and Nicolet, M.: J. Atmos Terr Phys, vol. 18, p. 65, 1960.

58. Bates, D. R. and Nicolet, M.: J Atmos Terr Phys, vol. 21, p. 286, 1961.

59. Dickinson, P. H. G. and Sayers, J.: Proc Phys Soc, vol. 76, p. 137, 1960.

60. Hertzberg, M.: J Atmos Terr Phys, vol. 20, p. 177, 1961.

61. Langstroth, G. F. O. and Hasted, J. B.: A general discussion of the Faraday Soc, vol. 33, p. 298, 1962.

62. Fite, W. L.; Rutherford, J. A.; Snow, W. R., and Van Lint, V. A. J.: A general discussion of the Faraday Soc, vol. 33, p. 298, 1962.

63. Whitten, R. C. and Poppoff, I. G.: Discuss Faraday Soc, vol. 37, p. p. 185, 1964.

64. Fehsenfeld, F. C.; Schmeltekopf, A. L.; and Ferguson, E. E.: Planet Space Sci, vol. 13, pp. 291-223, 1965.

REFERENCES (Continued)

65. Donahue, T. M.: Planet Space Sci, vol. 14, p. 33, 1966.

66. Copsey, M. J.; Smith, D.; and Sayers, J.: Planet Space Sci, vol. 14, pp. 1047-1055, 1966.

67. Warneck, P.: J Geophys Res, vol. 72, pp. 1651-1653, 1967.

68. Bohme (1967)

69. Strobel, D. F.: Ph.D. Thesis, Harvard University, Cambridge, Massachusetts, 1968.

70. Smith, D. and Fouracre, R. A.: Planet Space Sci, vol. 16, pp. 243-252, 1968.

71. Stubbe, P.: Planet Space Sci, vol. 17, pp. 1221-1231, 1969.

72. Bates, D. R.: Contemp Phys, vol. 11, pp. 105-124, 1970.

73. Strobel, D. F. and McElroy, M. B.: Planet Space Sci, vol. 18, p. 8, 1970.

74. Potter, R. L.: J Chem Phys, vol. 23, p. 2462, 1955.

75. Krassovsky, V. I.: Izv Akad Nauk, SSR, SerGeofix, vol. 4, p. 504, 1957.

76. Aquilanti, V. and Volpi, G. G.: Ric Sci, vol. 36, pp. 359-364, 1966.

77. Paulson, J. F.; Dale, F.; and Murad, E.: DASA Symposium, University of Pittsburgh, June 19-20, 1967.

78. Norten (1967)

79. Schmeltekopf, A. L.; Fehsenfeld, F. C.; Gilman, G. I.; and Ferguson, E. E.: Planet Space Sci, vol. 15, pp. 401-406, 1967.

80. Ferguson, E. E.; Fehsenfeld, F. C.; Goldan, P. D.; and Schmeltekopf, A. L.: J Geophys Res, vol. 70, p. 4323, 1965.

REFERENCES (Continued)

81. Nicolet, M. and Swider, W., Jr.: Planet Space Sci, vol. 11, pp. 1459-1482, 1963.

82. Goldan, P. D.; Schmeltekopf, A. L.; Fehsenfeld, F. C.; Schiff, H. I.; and Ferguson, E. E.: J Chem Phys, vol. 44, p. 4095, 1966.

83. McGowan, J. W.: Can J of Chem, vol. 47, p. 1779, 1969.

84. Fehsenfeld, F. C.; Dunkin, D. B.; and Ferguson, E. E.: Planet Space Sci, vol. 18, pp. 1267-1269, 1970.

85. Ferguson, E. E.; Fehsenfeld, F. C.; Goldan, P. D.; Schmeltekopf, A. L.; and Schiff, H. I.: Planet Space Sci, vol. 13, pp. 823-827, 1965.

86. Fontheim, E. G.; Beutler, A. E.; and Nagy, A. F.: Ann Geophys, vol. 24, p. 489, 1968.

87. Duboin, M. L.; Lejeune, G.; Petit, M.; and Weill, G.: J Atmos Terr Phys, vol. 30, pp. 299-304, 1968.

88. Cogger, L. L. and Shepherd, G. G.: Planet Space Sci, vol. 17, pp. 1857-1865, 1969.

89. Fournier, J. P. and Nagy, A. F.: J Atmos Sci, vol. 22, pp. 732-734, 1965.

90. Noxon, J. F. and Johanson, A. E.: Planet Space Sci, vol. 18, pp. 1367-1379, 1970.

91. Nichol. D. G.: Planet Space Sci, vol. 18, pp. 1335-1347, 1970.

92. Pal, S. R.: Planet Space Sci, vol. 18, pp. 1829-1831, 1970.

93. Evans, J. V.: J Geophys Res, vol. 70, pp. 4331-4364, 1965.

94. Sudworth, J. P.: Planet Space Sci, vol. 18, pp. 1011-1020, 1970.

95. Nagy, A. F. and Banks, P. M.: J Geophys Res, vol. 75, pp. 6260-6270, 1970.

REFERENCES (Continued)

96. Carlson, H. C.: Radio Sci, vol. 3, pp. 668-673, 1968.

97. Okuda, M. and Misawa, K.: Rept of Ionosphere Space Res Japan, vol. 23, pp. 1-8, 1969.

98. Bennett, R. I.: J Geophys Res, vol. 74, pp. 381-383, 1969.

99. Carpenter (1963)

100. Torr, M. R. and Torr, D. G.: J Geophys Res, vol. 74, p. 5187, 1969.

101. Campbell, W. H. and Matsushita, S.: J Geophys Res, vol. 72, pp. 3518-3521, 1967.

102. DeMore, W. and Raper, O. F.: J Chem Phys, vol. 44, p. 1780, 1964.

103. DeMore, W. and Raper, O. F.: Astrophys J, vol. 139, p. 1381, 1964.

104. Hunt, B. G.: J Atmos Sci, vol. 23, pp. 88-95, 1966.

105. Hunten, D. M. and McElroy, M. B.: Rev of Geophys, vol. 4, p. 303, 1966.

106. Snelling, D. R. and Bair, E. J.: J Chem Phys, vol. 47, pp. 228-234, 1967.

107. McGrath, W. D. and McGarvey, J. J.: Planet Space Sci, vol. 15, pp. 427-455, 1967.

108. Young, R. A., Black, G.; and Slanger, T. G.: J Chem Phys, vol. 49, pp. 4758-4768, 1968.

109. Noxon, J. F.: Space Sci Rev, vol. 8, pp. 92-134, 1968.

110. Peterson, V. L. and Van Zandt, T. E.: Planet Space Sci, vol. 17, pp. 1725-1736, 1969.

111. Dalgarno, A.: Ann Geophys, vol. 26, pp. 601-607, 1970.

112. Schaeffer, R. C.; Feldman, P. D.; and Fastie, W. G.: J Geophys Res, vol. 76, pp. 3168-3173, 1971.

REFERENCES (Continued)

113. Hernandez, G.: J Geophys Res, vol. 77, pp. 3625-3629, 1972.

114. Wallace, L. and Chamberlain, J. W.: Planet Space Sci, vol. 2, pp. 60-70, 1959.

115. Zipf, E. C., Jr.: J Geomagnet Geoelec, Kyoto, vol. 18, p. 301, 1965.

116. Peterson, V. L.; Van Zandt, T. E.; and Norton, R. B.: J Geophys Res, vol. 71, pp. 2255-2266, 1966.

117. Warneck, P. and Sullivan, J. O.: Planet Space Sci, vol. 14, pp. 1225-1226, 1966.

118. Snelling, D. R. and Bair, E. J.: J Chem Phys, vol. 48, pp. 5737-5738, 1968.

119. Gilmore, F. R.; Bauer, E.; and McGowan, J. W.: J Quant Spectros Radiat Trans, vol. 9, pp. 157-183, 1969.

120. Zipf, E. C.: Can J of Chem, vol. 47, pp. 1863-1877, 1969.

121. Noxon, J. F.: J Chem Phys, vol. 52, pp. 1852-1873, 1970.

122. Hunt, B. G.: J Geophys Res, vol. 71, pp. 1385-1398, 1966.

123. Roble, R. G.: Ph.D. Thesis, University of Michigan, Ann Arbor, Michigan, 1969.

124. Roble, R. G.; Hays, P. B.; and Nagy, A. F.: Planet Space Sci, vol. 16, p. 1109, 1968.

125. Purdy, C. M.; Megill, L. R.; and Roach, F. E.: J Res NBS, vol. 65C, pp. 213-216, 1961.

126. Born, M. and Wolf, E.: Principles of Optics. Third Edition, Pergamon Press, New York, 1965.

127. Tolansky, S.: An Introduction to Interferometry. Longmans, London, 1955.

REFERENCES (Continued)

128. Jenkins, F. A. and White, H. E.: Fundamentals of Optics. Second Edition, McGraw-Hill Book Company, Inc., New York, 1950.

129. Turgeon, E. C. and Shepherd, G. G.: Planet Space Sci, vol. 9, p. 925, 1962.

130. Wark, D. W.: Astrophys J, vol. 131, p. 491, 1960.

131. Jarrett, A. H.; Hoey, M. J.; and Paffrath, L.: Planet Space Sci, vol. 12, p. 591, 1964.

132. Jarrett, A. H. and Hoey, M. J.: Planet Space Sci, vol. 11, pp. 1251-1252, 1963.

133. Hays, P. B. and Roble, R. G.: Appl Opt, vol. 10, pp. 193-200, 1971.

133a. Noxon, J. F. and Johanson, A. E.: Planet Space Sci, vol. 20, pp. 2125-2151, 1972.

134. Kulkarni, P. V. and Sanders, L. L.: Planet Space Sci, vol. 12, pp. 189-194, 1964.

135. Blacker, H. V. and Gadsden, M.: Planet Space Sci, vol. 14, pp. 921-928, 1966.

136. Kulkarni, P. V.: Ann Geophys, vol. 25, pp. 747-751, 1969.

137. Doupnik, J. R. and Schmerling, E. R.: J ATP, vol. 27, pp. 917-941, 1965.

138. Walker, J. C. G.: J Atmos Sci, vol. 22, p. 462, 1965.

139. Chapman, S.: Proc Phys Soc, vol. 43, pp. 26 and 482, 1931.

140. Chapman, S.: Proc Roy Soc A, vol. 132, p. 353, 1931.

141. Rishbeth, H. and Garriot, O, K.: Introduction to Ionospheric Physics. International Geophysics Series, Academic Press, New York and London, 1969.

REFERENCES (Continued)

142. Wickwar, V. B.: Ph.D. Thesis, Rice University, Houston, Texas, April 1971.

143. Deehr, C. S.: Ann Geophys, vol. 25, pp. 867-879, 1969.

144. Sivjee, G. G.: Ph.D. Thesis, The John Hopkins University, Baltimore, Maryland, 1970.

145. Newcomb, S.: Astrophys J, vol. 14, p. 297, 1901.

146. Slipher, V. M.: Astrophys J, vol. 49, p. 266, 1919.

147. Slipher, V. M.: Mon Not Roy Astron Soc, vol. 93, p. 657, 1933.

148. Rayleigh, Lord: Proc Roy Soc A, vol. 106, p. 117, 1924.

149. Rayleigh, Lord: Proc Roy Soc A, vol. 109, p. 428, 1925.

150. Rayleigh, Lord: Proc Roy Soc A, vol. 119, p. 11, 1928.

151. Rayleigh, Lord: Proc Roy Soc A, vol. 124, p. 395, 1929.

152. McLennan, J. C.; McLeod, J. H., and Ireton, H. J. C.: Trans Roy Soc Canada, vol. 22, p. 397, 1928.

153. Dufay, J.: Re'unions de l'institut d'optique, Paris, June 13, 1933.

154. Garrigue, H.: Comptes Rendus, vol. 202, pp. 1807-1809, 1936.

155. Garrigue, H.: Comptes Rendus, vol. 203, pp. 484-487, 1936.

156. Cabannes, J. and Garrigue, H.: Comptes Rendus, vol. 203, pp. 484-487, 1936.

157. Currie, B. W. and Edwards, H. W.: Terr Mag, vol. 41, p. 265, 1936.

158. Dufay, J. and Dufay, M.: Comptes Rendus, vol. 226, pp. 1208-1210, 1948.

REFERENCES (Continued)

159. Elvey, C. T. and Farnsworth, A. H.: Astrophys J, vol. 96, pp. 451-467, 1942.

160. Elvey, C. T.: Emission Spectra of the Night Sky and Aurorae. Report of the Gassiot Committee, London Phys Soc, p. 16, 1948.

161. Bates, D. R. and Massey, H. S. W.: Proc Roy Soc A, vol. 87, p. 261, 1946.

162. Dufay, J. and Mao-Lin, Tcheng: Ann Geophys, vol. 2, p. 189, 1946.

163. Barbier, D.: The Airglow and Aurorae. Ed. by E. B. Armstrong and A. Dalgarno, Pergamon Press, London, p. 38, 1956.

164. Berthier, P.: Comptes Rendus, vol. 236, pp. 1593-1595, 1953.

165. Robley, R.: Comptes Rendus, vol. 243, p. 2120, 1956.

166. Bates, D. R.: Emission Spectra of the Night Sky and Aurorae. Report of the Gassiot Committee, London Phys Soc, p. 21, 1948.

167. Barbier, D.: Comptes Rendus, vol. 244, pp. 2077-2080, 1957.

168. Dufay, J. and Mao-Lin, Tcheng: Ann Geophys, vol. 11, pp. 387-389, 1955.

169. Heppner, J. P.; Stolarik, J. D.; and Meredith, L. H.: Trans Am Geophys Union, vol. 38, p. 394, 1957.

170. Heppner, J. P. and Meredith, L. H.: J Geophys Res, vol. 66, p. 51, 1968.

171. Zipf, E. C. and Heath, D. F.: Trans Am Geophys Union, vol. 43, p. 436, 1962.

172. Gulledge, I. S. and Packer, D. M.: Astron J, vol. 71, p. 163, 1966.

173. Reed, E. I. and Blamont, J. E.: Space Res 7, Ed. by R. L. Smith-Rose, North Holland Press, Amsterdam, p. 337, 1967.

REFERENCES (Continued)

174. Ratcliffe, J. A.; Schmerling, E. R.; Setty, C. S. G. K.; and Thomas, J. O.: Phil Trans, vol. 248, p. 621, 1955.

175. Bates, D. R.: Rocket Exploration of the Upper Atmosphere. Ed. by R. L. F. Boyd and M. J. Seaton, Pergamon Press, London, p. 347, 1954.

176. Bates, D. R.: Solar Eclipses and the Ionosphere. Ed. by W. J. G. Beynon and G. M. Brown, Pergamon Press, London, p. 91, 1956.

177. St. Amand, P.: Ann de Geophys, vol. 11, p. 450, 1955.

178. Huruhata, M.; Nakamura, T.; Tanabe, H.; and Tohmatsu, T.: Rept of Ionosphere Space Res Japan, vol. 13, pp. 283-289, 1959.

179. Lagos, P.; Bellew, W.; and Silverman, S. M.: J Atmos Terr Phys, vol. 25, p. 581, 1963.

180. Holmes, J. C.; Johnson, C. Y.; and Young, J. M.: Space Res, vol. 5, p. 756, 1965.

181. Okuda, M.: Rept of Ionosphere Space Res Japan, vol. 19, pp. 470-481, 1965.

182. Okuda, M.: Rept of Ionosphere Space Res Japan, vol. 20, pp. 304-311, 1966.

183. Noxon, J. F. and Goody, R. M.: J Atmos Sci, vol. 19, pp. 342-343, 1962.

184. Wallace, L. and Nidey, R. A.: J Geophys Res, vol. 69, pp. 471-479, 1964.

185. Nagata, T.; Tohmatsu, T.; and Oagwa, T.: Planet Space Sci, vol. 13, pp. 1273-1282, 1965.

186. Gulledge, I. S. and Packer, D. M.: Trans Am Geophys Union, vol. 46, p. 61, 1965.

REFERENCES (Continued)

187. Huruhata, M.; Nakamura, T.; and Tanabe, H.: Rept of Ionosphere Space Res Japan, vol. 20, p. 223, 1966.

188. Eather, R. H.: J Geophys Res, vol. 74, pp. 153-158, 1969.

189. Detwiler, C. R.; Garrett, D. L.; Purcell, J. D.; and Tousey, R.: Ann Geophys, vol. 17, p. 263, 1961.

190. Parkinson, W. H. and Reeves, E. M.: Solar Phys, vol. 10, p. 342, 1969.

191. Brasher, W. E. and Hanson, W. B.: Radio Sci, vol. 5, pp. 1325-1340, 1970.

192. Van Zandt, T. E. and Peterson, V. L.: Ann Geophys, vol. 24, pp. 747-759, 1968.

193. Meinel, A. B.: Astrophys J, vol. 112, pp. 120-130, 1950.

194. Bates, D. R. and Nicolet, M.: J Geophys Res, vol. 55, pp. 301-327, 1950.

195. Herzberg, G.: J Roy Ast Canada, vol. 45, p. 100, 1951.

196. McKinley, J. D., Jr.; Garvin, D.; and Boudart, M. J.: J Chem Phys, vol. 23, p. 784, 1955.

197. Krassovsky, V. I. and Lukashenia, V. T.: Doklady Akad Nauk, SSR, vol. 80, p. 735, 1951.

198. Bates, D. R. and Moiseiwitch, B. L.: J Atm Terr Phys, vol. 8, p. 305, 1956.

199. Bates, D. R. and Moiseiwitch, B. L.: J Atm Terr Phys, vol. 11, p. 68, 1957.

200. Gattinger, R. L.: Ann Geophys, vol. 25, p. 825, 1969.

201. Hesstvedt, E.: J Geophys Res, vol. 75, p. 2337, 1970.

REFERENCES (Concluded)

202. Packer, D. M.: Ann Geophys, vol. 17, pp. 67-75, 1961.

203. Baker, D. J. and Waddoups, R. O.: J Geophys Res, vol. 72, p. 4881, 1967.

204. Krassovsky, V. I.; Shefov, N. N.; and Yarin, V. I.: J Atmos Terr Phys, vol. 21, pp. 46-53, 1961.

205. Huruhata, M.: J Geophys Res, vol. 70, pp. 4927-4929, 1965.

205a. Chamberlain, J. W. and Smith, C. A.: J Geophys Res, vol. 64, pp. 611-614, 1959.

206. Blackwell, D. E.; Ingram, M. F.; and Rundle, H. N.: Astrophys J, vol. 131, pp. 15-24, 1960.

207. Kvifte, G.: Planet Space Sci, vol. 5, pp. 153-162, 1961.

208. Krassovsky, V. I. and Shefov, N. N.: Space Sci Rev, vol. 4, pp. 176-198, 1965.

209. Greenspan (1966)

210. Kvifte, G. J.: Planet Space Sci, vol. 15, pp. 1515-1523, 1967.

211. Chiplonkar, M. W. and Tillu, A. D.: Indian J Pure Appl Phys, vol. 5, pp. 87-92, 1967.

212. Smith, L. L.: J Geophys Res, vol. 74, pp. 3042-3045, 1969.

213. Shefov (1969)

214. Rao, V. R. and Kulkarni, P. V.: Planet Space Sci, vol. 20, pp. 2198-2201, 1972.

BIBLIOGRAPHY

Barbier, D.: Ann Geophys, vol. 15, pp. 179-190, 1959.

Barbier, D.: Ann Geophys, vol. 21, pp. 228-249, 1965.

Bellew, W. and Silverman, S. M.: Planet Space Sci, vol. 14, pp. 407-429, 1966.

Biondi, M. A.: J Geophys Res, vol. 77, p. 1869, 1972.

Bohme, D. K.; Ong, P. P.; Hasted, J. B.; and Megill, L. R.: Planet Space Sci, vol. 15, p. 1777, 1967.

Brieg, E. L.: Planet Space Sci, vol. 18, pp. 1271-1274, 1970.

Carpenter, D. L.: J Geophys Res, vol. 68, p. 1675, 1963.

Chapman, S.: Proc Phys Soc, vol. B66, p. 710, 1953.

Dandikar, B. S.: Appl Optics, vol. 5, p. 835, 1966.

Davis, T. N. and Smith, L. L.: J Geophys Res, vol. 72, pp. 3518-3521, 1967.

DeMore, W. and Raper, O. F.: J Chem Phys, vol. 27, pp. 2048-2052, 1962.

DeVries, L. L.: Experimental Evidence in Support of the Joule Heating Associated with Geomagnetic Activity. NASA TMX-64568, Feb. 10, 1971.

DuCastel, F.; Carru, H.; Petit, M.; and Waldteufel, P.: L'onde electrique, vol. 468, p. 281, 1966.

Feldman, P. D.; Doering, J. P.; and Zipf, E. C.: J Geophys Res, vol. 76, pp. 3087-3094, 1971.

Ferguson, E. E.: Rev of Geophys, vol. 5, pp. 305-327, 1967.

Geller, M. A. and Sechrist, C. F., Jr.: J Atmos Terr Phys, vol. 33, pp. 1027-1040, 1971.

BIBLIOGRAPHY (Continued)

Ghosh, S. N. and Gupta, S. K.: J of Geomagne Geoelec, vol. 22, pp, 329-339, 1970.

Gordon, M. A.: Planet Space Sci, vol. 16, pp. 297-308, 1968.

Green, A. E. S.; Lindenmeyer, C. S.; and Griggs, M. J.: J Geophys Res, vol. 69, p. 493, 1964.

Greenspan, J. A.: J Atmos Terr Phys, vol. 28, p. 79, 1966.

Henry, R. J. W.: Phys Rev, vol. 162, p. 56, 1967.

Henry, R. J. W.; Burke, P. G.; and Sinfailam, A. L.: Phys Rev, vol. 178, pp. 218-225, 1969.

Hesstvedt, E.: Geophys Publikosjoner, Norske Videnskaps-Akad, Oslo, vol. 25(3), 1964.

McElroy, M. B.: Planet Space Sci, vol. 13, pp. 404-433, 1965.

Norton, R. B.: J Geophys Res, vol. 72, p. 5552, 1967.

O'Brien, B. J.: Aurora and Airglow. Ed. by B. McCormac, Rheinhold Publishing Corp., New York, 1967.

Pal, S. R.: Ann Geophys, vol. 26, pp. 791-793, 1970.

Reber, C. A.: J Geophys Res, vol. 77, p. 2871, 1972.

Schulz, G. J. and McDowell, J. T.: Phys Rev, vol. 128, p. 174, 1962.

Seaton, M. J.: Astrophys J, vol. 127, pp. 67-74, 1958.

Shefov, N. N.: Planet Space Sci, vol. 16, p. 1629, 1969.

Smith, K.; Henry, R. J. W.; and Burke, P. G.: Phys Rev, vol. 157, pp. 51-68, 1967.

Sunshine, G.; Aubrey, B. B.; and Bederson, B.: Phys Rev, vol. 154, p. 1, 1967.

BIBLIOGRAPHY (Concluded)

Taeusch, D. R.; Carignan, G. R.; and Reber, C. A.: J Geophys Res, vol. 74, p. 5187, 1969.

Tolpadi, S. K. and Singh, R. N.: Indian J of Pure and Appl Phys, vol. 9, pp. 342-345, 1971.

Von Zahn, U.: J Geophys Res, vol. 75, pp. 5517-5527, 1970.

Weill, G.: Atmospheric Emissions. Ed. by B. M. McCormac and A. Ombolt, Van Nostrand Rheinhold, Co., New York, 1969.

*U.S. GOVERNMENT PRINTING OFFICE: 1976 - 635-275/117

NATIONAL AERONAUTICS AND SPACE ADMINISTRATION
WASHINGTON, D.C. 20546

OFFICIAL BUSINESS
PENALTY FOR PRIVATE USE $300

SPECIAL FOURTH-CLASS RATE
BOOK

POSTAGE AND FEES PAID
NATIONAL AERONAUTICS AND
SPACE ADMINISTRATION
451

U.S.MAIL

749 001 C1 U E 760903 S00903DS
DEPT OF THE AIR FORCE
AF WEAPONS LABORATORY
ATTN: TECHNICAL LIBRARY (SUL)
KIRTLAND AFB NM 87117

POSTMASTER: If Undeliverable (Section 158 Postal Manual) Do Not Return

"The aeronautical and space activities of the United States shall be conducted so as to contribute . . . to the expansion of human knowledge of phenomena in the atmosphere and space. The Administration shall provide for the widest practicable and appropriate dissemination of information concerning its activities and the results thereof."

—NATIONAL AERONAUTICS AND SPACE ACT OF 1958

NASA SCIENTIFIC AND TECHNICAL PUBLICATIONS

TECHNICAL REPORTS: Scientific and technical information considered important, complete, and a lasting contribution to existing knowledge.

TECHNICAL NOTES: Information less broad in scope but nevertheless of importance as a contribution to existing knowledge.

TECHNICAL MEMORANDUMS: Information receiving limited distribution because of preliminary data, security classification, or other reasons. Also includes conference proceedings with either limited or unlimited distribution.

CONTRACTOR REPORTS: Scientific and technical information generated under a NASA contract or grant and considered an important contribution to existing knowledge.

TECHNICAL TRANSLATIONS: Information published in a foreign language considered to merit NASA distribution in English.

SPECIAL PUBLICATIONS: Information derived from or of value to NASA activities. Publications include final reports of major projects, monographs, data compilations, handbooks, sourcebooks, and special bibliographies.

TECHNOLOGY UTILIZATION PUBLICATIONS: Information on technology used by NASA that may be of particular interest in commercial and other non-aerospace applications. Publications include Tech Briefs, Technology Utilization Reports and Technology Surveys.

Details on the availability of these publications may be obtained from:

SCIENTIFIC AND TECHNICAL INFORMATION OFFICE

NATIONAL AERONAUTICS AND SPACE ADMINISTRATION

Washington, D.C. 20546